Periodic Subwavelength Photonic Structures

by

Erika Ye

B.S. Massachusetts Institute of Technology, Cambridge (2014)

Submitted to the Department of Electrical Engineering

in Partial Fulfillment of the Requirements for the Degree of

Masters of Engineering in Electrical Engineering and Computer Science

at the

Massachusetts Institute of Technology

June 2015

Signature redacted

Author:.. .....

Department of Electrical Engineering and Computer Science

Mays 29, 2015

Signature redacted

Certified by:..... .....

Prof. Rajeev Ram, Thesis Supervisor

May 29, 2015

Signature redacted

Accepted by:..... .....

Prof. Albert R. Meyer, Chairman, Masters of Engineering Thesis Committee

Periodic Subwavelength Photonic Structures

by Erika Ye

Submitted to the Department of Electrical Engineering and Computer Science

May 29, 2015

in in Partial Fulfillment of the Requirements for the Degree of Masters of Engineering in Electrical Engineering and Computer Science

Three applications of the interaction of light with periodic dielectric structures are investigated. The first application is large-area spectroscopy, for which we use the mid-field diffraction pattern generated by the light source passing through a transmission grating to determine its spectral composition. By utilizing a large grating size, we are able to achieve resolutions of < 4 nm experimental while having an etendue of roughly 0.033 mm^2. Furthermore, since we are sampling the mid-field light pattern as opposed to the far-field, the entire spectrometer can fit within a 10 mm by 10 mm by 5 mm volume. The second application are barcodes based on the wavelength-dependent back-scattering off of a photonic crystal resonant cavity. The challenge is that we want to observe high quality factor resonant peaks while reducing the size of the crystal to less than 10 microns. So far the highest quality factor observed was about 800. The third application is a Fano silicon photonic crystal modulator waveguide device. The resonant cavity of the modulator is a 1D photonic crystal cavity. If we excite the fundamental and first excited mode of the waveguide, we obtain a Fano resonance that can potentially increase modulation depth and efficiency. We investigated how to improve the modulator architecture to reliably design resonators with sharp Fano resonance peaks. Those these applications are still in their early stages, the are promising for furthering each technology.

Contents

List of Figures

List of Tables

Chapter 1

Introduction

1.1 Thesis Overview

In this thesis, we will discuss three applications for sub-wavelength photonic structures: spectroscopy of a large area beam using a diffraction grating, a small-scale photonic crystal (PhC) resonant cavity barcode or tag, and a photonic crystal electro-optical (EO) modulator. Though these applications are quite different, we intend to investigate them from the perspective of understanding how they can be realized by using periodic structures, on the order of the wavelength, in their design. Furthermore, the final version of these devices ideally will be CMOS compatible, allowing for efficient and reliable fabrication. The scope of the thesis includes only the first design iterations of these devices.

Our motivation for investigating large-area spectroscopy is to design a miniature, wearable spectrometer. By designing the spectrometer to accept a large area of the signal, but likely at the cost of having a small numerical aperture (NA), we can reduce the size of the spectrometer by using information in the mid-field diffraction pattern instead of the far-field pattern. We also hope that the large area spectrometer will detect spectral information from the entire sampling area, which would help us spectrally resolve a diffuse and potentially non-uniform light source. In order to accurately detect and differentiate optical transitions from biological compounds like glucose, the spectrometer will need a resolution of 0.3 nm, and have a bandwidth of at least 100 nm [13]. In order to be integrated into a wearable device, the spectrometer will need to be less than 5 mm thick, and ideally about 1 cm by 1 cm in horizontal area. In comparison, the company Ibsen Photonics sells a compact spectrometer with a foot print of 25 mm by 48 mm by 16 mm, a wavelength range from 475 nm to 1100 nm, and a minimum resolution of 1.7 nm [59]. A higher resolution spectrometer has a

resolution of 0.6nm, but has a larger footprint of 61 mm by 65 mm by 19 mm [60].

The main motivation behind designing microscopic PhC tags is to label individual cells in a biological system. PhC resonant cavities are defects in the periodic dielectric structure that support resonant modes otherwise not allowed in the surrounding dielectric structure. The resonant frequency of the cavity can be adjusted by slightly changing the size of the defect and other parameters of the PhC. Because the PhC resonant modes are in-plane resonances, the angle of incidence would only affect the observed intensity of the modes but not the observed resonant frequency. Being able to resolve the labels according to frequency rather than intensity allows for accurate identification of the cells. The goal for this application is to design at least 10000 different barcodes within a 100 nm spectral range. This would require a small resonant cavity with a full-width half max of 0.01 nm. Having 10000 different barcodes would ensure that even if 1% of barcodes were successfully associated with a cell, 1000 cells would be uniquely labelled. This constraint could be relaxed if there were multiple resonance peaks that could be independently defined in frequency, or a single cell could associate with multiple barcodes. If the resonant peaks could be independently defined, in order to have at least 10000 codes, we would need 14 different resonant peaks. To be within a 100 nm spectral range, the FWHM would have to be at most 7 nm.

The third device, the electrically driven optical modulator, is a the device that imparts information from an electrical signal onto a constant laser source. A modulator is essentially a resonant cavity, whose resonant frequency can change depending on changes in its refractive index. Though modulators can be made of any electro-optically active material, we focus on silicon modulators for the ease of integrating them with electrical computing systems. One application of EO modulators is to use them as optical interconnects in a microprocessor environment. Integrating optics with electronics in a microprocessor has the potential for increasing processor speeds. As modulators are just one component of the entire system, minimizing its operating energy and its size, while maintaining a usable extinction ratio (at least 3 dB), is ideal. In contrast to the usual EO modulators that rely on resonant cavities with Lorentzian transmission curves, we hope to utilize a Fano resonance to increase modulation extinction while requiring a smaller change in the index of refraction and a smaller peak-to-peak voltage. We hope that these Fano EO modulators will have at least 3 dB extinction at 10 Gbps operation while using less than 1V peak-to-peak.

The following sections provide some background for these three applications, and more detail on our motivations for pursuing them. We'll first talk about the large-area miniature spectrometer in Section 1.2, then discuss the photonic crystal barcodes in Section 1.3, and end with the photonic crystal modulators 1.4. At the end of the introduction, there will be a brief introduction on photonic crystals.

1.2 Introduction to Diffraction Grating Spectroscopy

Researchers use a variety of spectroscopic techniques to characterize a sample of interest. By exposing the sample to some form of energy, we probe the sample of interest to gain information about the sample. One type of spectroscopy that is gaining interest is Raman spectroscopy. Raman spectroscopy relies on the inelastic scattering of monochromatic light to characterize the system's molecular vibrations, phonons, and other vibrational excitations of the system. Inelastic scattering changes the energy of the laser source, so the information in Raman spectroscopy is contained in the energy shifts of the laser source. Since the inelastically scattered light (Raman scattering) is typically much weaker than the elastically scattered light (Rayleigh scattering), one filters out the source wavelength and then must resolve the remaining frequencies of light.

Spectrometers are used to determine the spectral composition of a light source. Most spectrometers today are large in size, expensive, and use cooled CCD detectors. Especially in the case of Raman spectroscopy, where the signal tends to be relatively weak, larger systems are needed to detect the signal with less noise. The work presented in this thesis is the first step in an attempt to build a miniature, chip-scale spectrometer that can be used to detect Raman signal.

Current spectrometers rely on using a narrow slit to localize the input beam. The input beam is then incident on a diffraction grating, and diffracts at an angle that is determined by the wavelength. The slit drastically reduces the intensity of light that the spectrometer is able to collect, so lenses that collect the desired signal and focus it onto the entrance slit can significantly increase the signal [28]. The amount of light that can be collected by the optical system is called the "etendue," and is a function of the area of the light and the range in angles of propagation.

1.2.1 The Proposed Technology

In order to determine spectral composition of a large area, diffuse light source, while making a compact (1 cm x 1 cm x 5 mm) spectrometer, we hope to use a large area grating and uses information from the mid-field interference pattern, the Talbot effect. The large area grating will allow us to obtain information from a wide area, though it comes at the cost of needing little variation in the input angle.

Again, the desired specifications of the spectrometer is a spectral resolution of about 0.3 nm, and a bandwidth from about 800 nm to 900 nm. Glucose exhibits strong Raman peaks in the range from 350 cm^{-1} to 1350 cm^{-1} from the excitation laser [13]. If we use an excitation source at 785 nm, we expect the most

important Raman signal to be found from 807 nm to 893 nm. The two closest, identifiable peaks in the range have shifts of about 913 cm^{-1} and 898 cm^{-1} [83]. This corresponds to wavelengths of 845.6 nm and 844.5 nm. Therefore, the spectrometer should have a resolution between 0.1 nm and 0.6 nm for the peaks to be clearly distinguished.

Previous Work on "Small" Spectrometers

In 2003, Xu et al. published work on using a disordered photonic crystal with spatio-spectral transmission patterns to resolve multimodal diffuse sources [92]. They argued that by mapping the spectral transmission through the photonic crystal at each point of the crystal, the spectrum of the source could be determined. They proposed that multimode spectrometers with 1-10 nm resolution could be made using this technique, though they themselves were limited to a 5 nm resolution. The advantage of this technique was that they could resolve highly diffuse sources without any other lenses. However, most of the incident light would be reflected by 3D PhC, they had little advantage in intensity despite the apparent higher etendue. In fact, only certain regions of the photonic crystal behaved like a spectrometer, so even though the aperture area was large, only small area was usable. Furthermore, the manufacturing process is less than ideal for large scale reproduction.

A few years ago, Redding et al. published work regarding a compact spectrometer based on a disordered SOI photonic chip [67]. The light source is delivered from a ridge waveguide into a 2D space with randomly placed air-holes in the silicon body. They argue that the multiple scattering in a disordered medium increases the effective optical path, as the effective optical path in the diffusive regime is given by L^2/l_t [67] [61], where l_t is the transport mean free path and L is the length of the region with random scatterers. Light of different frequencies bounce through random scatterers differently, and hit a different set of photodetectors that line the rim of the cavity with the random scatterers. By identifying which combination of photodetectors are lit up, the spectral composition of the input laser source can be determined. Redding further developed that by carefully engineering "disorder", out-of-chip scattering could be reduced, improving overall throughput [67]. This confirms that this multi-scattering technique works even if the scatterers are not completely randomly placed. The main issue with this technique is that the light source is delivered from a ridge waveguide, which limits the application of this technique as a spectrometer.

The above spectrometers would require training the device to first observe the detector response at a range of wavelengths, and then using deconvolution methods to determine the spectrum. There has also been work on spectrometers that require less computation. In 2008, Park et al. presented a spectrometer that

used the wavelength sensitivity of Fresnel diffraction from a circular gradient grating [58] [57]. Operation of such a spectrometer is similar to that of a spectrometer that operates in far-field. They determined that by using a circular gradient grating, the spectral resolution does not depend on the size of the spectrometer. The reported spectral resolution is about 10 nm to 23 nm.

In 2001, Kung et al. presented a transform spectrometer based on the Talbot effect [38]. The spectrometer used a typical diffraction grating, but the detector was placed in the mid-field, as opposed to the far-field. In the mid-field of a diffraction grating, the light field is a series of periodically spaced replicas of the grating image. The periodicity of these self-images is a function of wavelength. This effect is called the Talbot Effect. However, Kung et al. were unable to achieve particularly high resolution because they use a diffraction grating with a large periodicity and use a lens to magnify each self-image onto a pixel of the CCD detector. The advantage of Kung's technique over the previous two is the simplicity of the data analysis, requiring only Fourier transforms.

There has been limited work on using the Talbot effect for spectrometry. Other work includes a paper by Lokshin et al. who was able to achieve 2 nm resolution for mercury vapor radiation [40]. They used a moving detector within the first self-image to observe different frequencies of light. The resolution was determined by depth of the self-image. They claimed that by increasing the number of grating lines, the resolution was increased. They also suggested using a second grating identical to the first to increase the spectral resolution in a Talbot spectrometer [40]. However, their analysis appears to be theoretical and rely on the paraxial approximation. In a large-scale system, this approximation cannot be kept with high confidence. With Lokshin's idea of using two gratings, Guerineau et al. also designed a Talbot spectrometer, with a moving slit detector. It used a moving color CCD to reconstruct the mid-field light pattern of polychromatic light. They suggested that their method of obtaining the spectral information of a sample using RGB detectors would be more suitable for large bandwidth, low resolution samples [26]. Because their diffraction grating had a long period, their experiments behaved within the paraxial limit.

However, the results from these two works need to be taken with a grain of salt. Their work relies on the depth-of-focus of the Talbot image, which is reported differently in the two papers, without any derivation. Their claims also cannot be described by the Rayleigh derivation of the Talbot self-images at a single frequency (shown in Section 1.2.2). Another source reports a depth-of-focus of $z_T/4$, which is more consistent with our own simulations and the Rayleigh derivation [70]. A more in depth discussion will be in the Appendix.

Recently, Wang et al. presented work on using a broadband diffractive optic to perform high throughput

Table 1.1: Miniature Spectrometers

This table lists recent miniature spectrometers that have appeared in the literature. Estimates of spectrometer size include the space in between the grating and the detector. Etendue is calculated from $\pi(\mathrm{NA})^2 A_{slit}$.

Author	**Spectrometer Type**	**Resolution**	**Etendue (mm^2)**	**Size (mm x mm x mm)**
Kung 2001 [38]	Talbot	42 nm	0.003	40+ x 4.9 x 6.5
Xu 2003 [92]	Disordered 3D PhC	2-20 nm estimate	0.024	30+ x 5 x 5
Redding 2013 [67]	Disordered 2D PhC	0.75 nm	1e-7	0.100 x 0.050 on chip
Park 2008 [58]	Fresnel	10-23 nm	8.2e-4	1-7 x 0.750 x 0.750
Momeni 2009 [48]	Waveguide	0.010 nm	1e-7	0.080 x 0.200 on chip
Wang 2014 [87]	Broadband Diffractive Optic	1 nm	0.077	500 x 9 x 9
This work (goals)	Talbot	1 nm	> 0.003	10 x 10 x 5

spectroscopy. They build a library of pixel response versus wavelength for the given diffractive optic, and use it to predict the incident photon flux. They assume almost 100% transmission of photons through their diffractive optics, and use the quantum efficiency to help limit the possible wavelengths. They use computational errors to predict the spectrum from the detected signal. They were able to experimentally obtain 1 nm resolution, but simulated that they could achieve resolutions of 0.011 nm. However, similar to the Talbot spectrometer, they can only use a collimated light source.

A summary of the previous work is in Table 2.1.

1.2.2 Diffraction Grating Theory

In order to motivate using alternate methods for miniaturized spectroscopy, we need to prove that we will be unable to achieve the desired specifications for our project. Here, we will first review the physics of far-field diffraction from a grating, and then discuss why we can't use a far-field spectrometer for our project.

General Form of Diffraction and Its Approximations

Consider a spherical wave at a point of area dS, with an field amplitude A and an wavelength λ. The electric field dE at some distance r away from the origin of the wave is [28]

$$dE = \frac{A}{\lambda r} e^{i(\omega t - kr)} dS. \tag{1.1}$$

Now imagine that light passes through the aperture $S(\varepsilon, \eta, 0)$ and illuminates a point $P(x, y, z)$, which is a distance $r = \sqrt{x^2 + y^2 + z^2}$ away from the aperture. If the aperture were only open at a single point, the electric field at point P, ignoring the time dependence, can be found easily from equation 1.1 to be

$$E_p = \frac{iA}{\lambda} \frac{e^{-ikr}}{r}. \tag{1.2}$$

According to Huygen's principle, for a point P with a lateral position (x, y) a distance z away from the input field, the electric field can be obtained by adding together spherical waves being emitted from each point of the input plane (input aperture). The amplitude of the field can vary along of the plane of the input aperture. The x and y of the input aperture are represented as ε and η, and z is set to zero.

The x and y are the lateral positions of point P on a screen a distance z away from the aperture, and

$$U(P) = \frac{i}{\lambda} \iint A(\varepsilon, \eta) \frac{e^{-ikr'(\varepsilon,\eta))}}{r'(\varepsilon, \eta)} d\varepsilon d\eta \tag{1.3}$$

, where

$$r' = \sqrt{(x - \varepsilon)^2 + (y - \eta)^2 + z^2}. \tag{1.4}$$

Equation 1.3 is the general equation for diffraction, as no approximations are made to simplify the spherical wave. Though this equation can be solved numerically, approximations of r are often made in terms of ε and η.

For Fresnel (near-field) diffraction, the approximation is

$$r' \approx r - \frac{x\varepsilon + y\eta}{r} + \frac{\varepsilon^2 + \eta^2}{2r} \tag{1.5}$$

, and for Fraunhofer (far-field) diffraction, the approximation is

$$r' \approx r - \frac{x\varepsilon + y\eta}{r}. \tag{1.6}$$

These approximations are made by taking the dominant Taylor series expansion terms of $r(\varepsilon, \eta)$. In order to for the higher order terms of the Taylor expansion to be negligible in $exp(-jkr')$, they must satisfy

$kr'_{higherorder} << 2\pi$. For Fresnel diffraction, in order for the third and higher order terms to be negligible, we require that $\lambda << z$ and $\lambda << \sqrt{(x-\varepsilon)^2+(y-\eta)^2}$. Under these assumptions, we're looking at the region right behind the input aperture. In the case that $\sqrt{(x-\varepsilon)^2+(y-\eta)^2} << z$, we can also ignore the second order term, as is done for Fraunhofer diffraction. In this limit, we also notice that $r' \approx z$. Since this approximation requires us to stay close to the z-axis, this approximation is also referred to as the paraxial approximation.

The electric field in the Fraunhofer approximation is

$$U(P) = \frac{iAe^{-ikr'}}{\lambda r'} \iint_{-\infty}^{\infty} S(\varepsilon,\eta,0)e^{ik\frac{x\varepsilon+y\eta}{r'}} d\varepsilon d\eta. \tag{1.7}$$

Farfield Diffraction Grating Spectroscopy

Suppose the input aperture is a 1D diffraction grating, with N infinitely long slits of width w, periodically spaced a distance d away from each other, in a perfectly absorbing material. Mathematically, the diffraction grating can be expressed as

$$A(\varepsilon,\eta) = \sum_{k=1}^{N} \begin{cases} A_0 & (-w/2 < \varepsilon < w/2) + k - N/2 \\ 0 & (w/2 < abs(\varepsilon) < d/2) + k - N/2 \end{cases}$$

Solving Equation 1.7, we see the electric field is

$$E = \frac{wA}{z}(\frac{\sin\beta}{\beta})(\frac{\sin N\alpha}{\sin\alpha})\sin(\omega t - kR + (N-1)\alpha) \tag{1.8}$$

, where $\alpha = (\frac{kd}{2})\sin\theta$ and $\beta = (\frac{kw}{2})\sin\theta$.

From this equation we can obtain simplified equations about the maxima and minima of the diffraction pattern. The maxima for slits spaced a distance d apart, occur at

$$d\sin\theta_m = m\lambda \tag{1.9}$$

and the minima around each maximum occur at

$$d\sin\theta_n = \frac{(n+1)}{\pi N}\lambda \tag{1.10}$$

where $m = 0, \pm1, \pm2, ...$ is the order of the maxima, $n = \pm1, \pm2, ..., \pm(N-1)$ is the order of the minima,

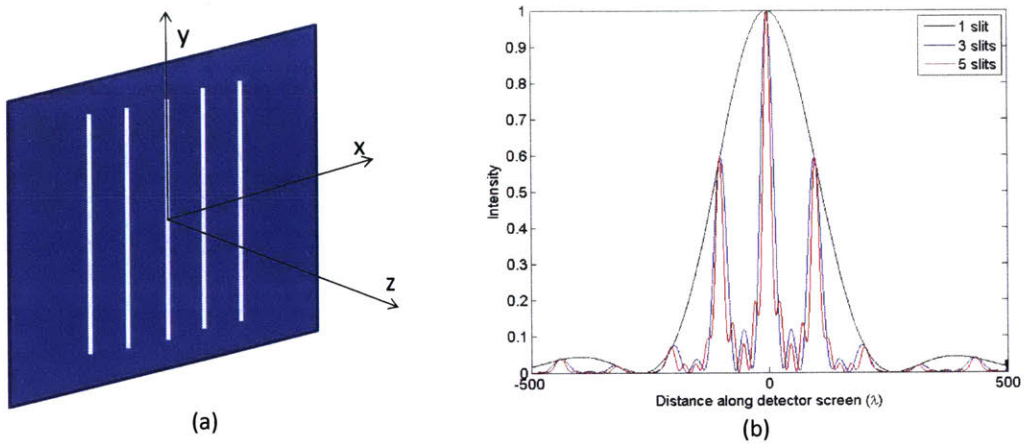

Figure 1.1: Depiction of Diffraction through a Grating in Far-Field
(a) This is a cartoon of the diffraction grating used. (b) This graph shows simulated diffraction patterns from a diffraction grating with only 1 slit, 3 slits, and 5 slits. Note that with an increasing number of slits, the peaks get narrower. The 1 slit spectrum is an envelope function for the narrower peaks.

and θ_m and θ_n is the angle from the center axis that maximum m or minimum n is found. These maxima and minima are shaped by an envelope diffraction pattern that results from the slit width w, which can be found from a single-slit transmission grating. If the slit width is much smaller than the slit spacing, there will be many maxima within the zeroth-order peak of the envelope diffraction pattern. θ_n also decreases when the number of slits is increased. Equation 1.9 can be made more general by considering oblique angles of incidence θ_i, in which the equation becomes $a(\sin\theta_m - \sin\theta_i) = m\lambda$.

The spectral resolution of a spectrometer is one measure of how well it performs. First, let us define the angular width, which is the effective width of a spectral line. Assuming Fraunhofer diffraction, and assuming a constant angle of incidence, the angular width of the peak is the spacing between two adjacent minima around the principle maximum, $\Delta\alpha = \frac{2\pi}{N}$. Plugging in $\alpha = \frac{ka}{2}\sin\theta$ from before, we find

$$\Delta\theta = \frac{2\lambda}{Nd\cos\theta_m}. \tag{1.11}$$

The angular dispersion tracks the difference in angular position corresponding to a difference in wavelength. Still assuming Fraunhofer diffraction, angular dispersion is

$$\mathscr{D} \equiv \frac{d\theta}{d\lambda} = \frac{m}{d\cos\theta_m}. \tag{1.12}$$

The chromatic resolving power is defined as the ratio of the wavelength to the least resolvable difference in wavelength possible, or $\mathscr{R} \equiv \frac{\lambda}{(\Delta\lambda)_{min}}$. Lord Rayleigh's criterion for the limit of resolution is when the principle maximum at one wavelength coincides with the principle minimum at another. This is equivalent to half of the angular width, so

$$(\Delta\theta)_{min} = \frac{\lambda}{Nd\cos\theta_m}. \tag{1.13}$$

We can find another expression for $(\Delta\theta)_{min}$ using Equation 1.9. After some work we find that

$$(\Delta\theta)_{min} = \frac{(\Delta\lambda)_{min}}{d\cos\theta_m}. \tag{1.14}$$

Setting Equations 1.13 and 1.14 equal to each other and rearranging the variables, we can determine that

$$\mathscr{R} = \frac{\lambda}{(\Delta\lambda)_{min}} = mN = \frac{Nd(\sin\theta_m - \sin\theta_i)}{\lambda}. \tag{1.15}$$

We conclude that for a binary diffraction grating, resolution is increased with an increased number of slits N, increased slit spacing d, decreased wavelength λ, and completely perpendicular incident light.

Our specifications require that at about $\lambda = 0.830$, we have at least 0.5 nm resolution. If we operate in the first diffraction order, we would need N = 1660 lines. Note that depending on d, different diffraction orders m may be achievable. However, using higher diffraction orders usually comes at a cost of lower intensity and lower bandwidth (since the θ_m's are less separated).

If we use a grating with 1660 lines, with a grating periodicity of $1.2d$, the size of the grating will be roughly 1.653 mm. In order to be in the far-field for a grating of this size, we'd need $z >> 1.653mm$. Let's say a z of about 165 mm is sufficient. Even if the beam could be folded on itself several times, we note that it'd be difficult to miniaturize the system into a 10 mm x 10 mm x 5 mm volume.

In practice, a small slit is used to spatially filter the incoming light such that only a certain range of angles are used in the spectrometer. The slit size is typically on the order of a few hundred microns in width.

The Talbot Effect

In 1836, H.F. Talbot observed that for a periodic diffraction grating as described above, the mid-field diffraction pattern is an image of the original diffraction grating every z_T from the input aperture [78]. This effect is now referred to as the self-imaging effect or the Talbot effect, and occurs because of the interference between the +1, 0, and -1 diffracted beams. The periodicity of the self-images, z_T, which we will refer to as

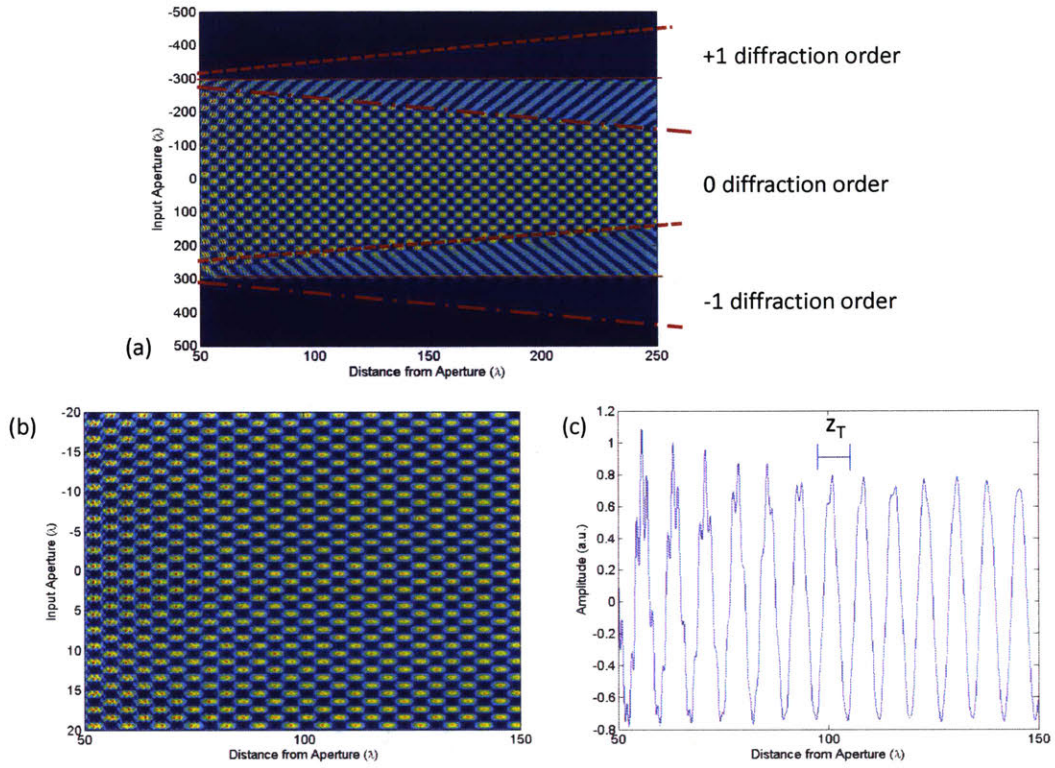

Figure 1.2: Talbot Effect
Picture showing the Talbot Effect. a) Simulated diffraction pattern with a periodic grating with a period of 2λ. b) Zoomed in image of diffraction pattern marked by the box in (a). c) Intensity of diffraction pattern along z for a given x. The period of the simple cosine is the Talbot distance. Together, this figure shows that the simplest self-imaging effect we observe is a result of the interference between the 0, +1, and -1 order diffraction beams.

Talbot depth, turns out to be a function of wavelength, so the Talbot can be used for spectroscopic purposes. One caveat is that the light source needs to be a plane wave, which is a condition we would like to avoid. However, to better understand mid-field diffraction as a means of lens-less spectroscopy, we will make this assumption for our initial analysis.

Lord Rayleigh explained the Talbot effect by calculating the intensities of interfering plane waves propagating at angles dictated by diffraction [41]. The fields of the propagating waves can be expressed as

$$A_0 \exp(j(\omega t - kz)) +$$
$$A_1 \cos(k_{\parallel,1} x) \exp(j(\omega t - k_{\perp,1} z)) +$$
$$A_2 \cos(k_{\parallel,2} x) \exp(j(\omega t - k_{\perp,2} z)) + ... \tag{1.16}$$

, where $k_{\parallel,n} = \frac{2n\pi}{d}$, $k_{\perp,n}^2 = k^2 - k_{\parallel,n}^2$, and d is the periodicity of the grating.

The intensity of this field would be

$$A_0^2 + A_1^2 \cos^2(k_{\parallel,1} x) + A_2^2 \cos^2(k_{\parallel,2} x) +$$
$$A_0 A_1 \cos(k_{\parallel,1} x)(\exp(j(kz - k_{\perp,1} z)) + \exp(-j(kz - k_{\perp,1} z))) +$$
$$A_0 A_2 \cos(k_{\parallel,2} x)(\exp(j(kz - k_{\perp,2} z)) + \exp(-j(kz - k_{\perp,2} z))) + ... \tag{1.17}$$

The field is periodic in z, but has multiple periods if there are multiple diffraction orders. If the grating is engineered such that only the 0, +1, and -1 diffraction orders exist, then $A_2 = 0$, and $kz - k_{\perp,1} z = 2\pi n$ determines the periodicity of the field in z. The period of the mid-field diffraction pattern, which is referred to as the Talbot depth, is therefore

$$z_T = \frac{\lambda}{1 - \sqrt{1 - \frac{\lambda^2}{d^2}}}, \tag{1.18}$$

where d is the period of the grating. For large d, $z_T \approx \frac{2d^2}{\lambda}$. Because the Talbot depth is a function of wavelength, if one could measure the Talbot depth from the midfield diffraction pattern, one could potentially use this information to determine the spectral composition of the light source.

Limitations and Considerations

This section introduced diffraction from a classical perspective that is generally well understood. However, if we were to foray further into nanoscale features on the diffraction grating, full numerical solvers of Maxwell's equations would need to be used. For example, if we were to consider a grating with features on the order of the incident wavelength, as is the case for all of the photonic crystal work, the approximate boundary conditions used previously are no longer valid, and the vector behavior of the field has to be considered. This

would lead to varied transmission depending on the polarization of light, and could also exhibit plasmonic effects that could greatly increase the transmission of light through subwavelength holes [22].

However, in this thesis, we will focus on optimizing the Talbot spectrometer using a basic grating. For future work on this project, we will need to find a way to use the Talbot spectrometer when in close proximity to a diffuse light source. This might require investigating light transmission through additional gratings or more complex photonic crystal-like structures to understand how they could be used to collimate or focus incoming light.

1.3 Introduction to Photonic Crystal Barcodes

The spectrometer relies on the scattering from an out-of-plane light source on a 1-dimensional periodic dielectric structure. The next two applications are based on effects that result from in-plane light scattering off a periodic dielectric structure. The devices are based on waveguide structures, so the light is now confined and propagates only in the plane of the waveguide. The periodicity of the patterned structures in the waveguide are typically shorter than the wavelength, so the scattered light no longer has multiple diffraction orders. So, while the device still uses a periodic dielectric structure, the boundary conditions lead to very different results. These types of dielectric structures are photonic crystals (PhCs), which are described in more detail in section 1.5.1.

1.3.1 The Proposed Technology

We aim to create high quality factor (high Q) resonant cavities that would effectively couple to light from free space at the resonant frequency, such that it would be possible to determine the resonant frequencies of a photonic crystal cavity by looking at the reflection spectrum. Far from the resonant frequency, we expect the light to simply reflect off of the photonic crystal. However, near the resonant frequency, the light transfers energy to the PhC resonant cavity. As a result, the specular reflection off the barcode is reduced. However, the resonant mode also radiates light, so we'll need to filter out the radiated light from the reflected light. A more mathematical description explaining the interaction of the incident field with a resonant cavity is in Section 1.5.1.

In order to use PhCs as biological barcodes, the barcode must be inert and non-toxic, identifiable regardless of orientation, and easy to modify and manufacture. Additionally, if we want to have a library of 10000 barcodes, the bandwidth of the resonant cavities must be very small. As mentioned in the overview, we are

targeting a half-power bandwidth of less than 0.01 nm, which corresponds roughly to a quality factor of 10^5 if we operate at a wavelength of 1000 $\pm$ 50 nm. To tag individual cells, the cavities should be at most a few microns in diameter. These specifications are quite aggressive, compared to other biological barcodes, but could allow for more advanced biological research.

1.3.2 Potential Applications

Biological research has made significant advances that allow researchers to experiment on individual cells. However, unless the cell is isolated, it is difficult to repeatedly observe the same cell with high confidence. Therefore, we hope that our tagging device could be used to track individual cells over time and as they are transferred from one analysis platform to another. For use in biological systems, these devices and the reading method should interfere minimally with cell behavior.

Our devices could also be used for tagging other microscopic things. For example, there has been work to include barcoding in high-density and multiplex assays, due to the sheer number of samples that need to be processed. Each reaction well could be marked with this optical tag for fast and reliable relocation. The company Illumina offers an automated microarray processing product, which is able to track samples using a "PosID reagent barcode scanning" system [32]. Though the details of their tracking technology is not disclosed, it seems like the chemical reagents used in their microarrays are encoded with some extra information that can be probed optically. The photonic crystal devices proposed here could be used in a similar fashion, but with a wider range of applications because its presence is independent of the reaction inside the well. Since the barcodes can be on the scale of a few microns, they can also be transferred with the fluids from a single well to another platform if necessary.

Alternatively, these photonic crystal devices can be used more "actively". Because the proposed devices are sensitive to the index of the surrounding material, these types of devices could also be used as a sensor that detects changes in index of refraction. In this case, the devices would ideally be in a known location, so that we could track changes in the index by observing the shift in the resonant wavelength of the device.

1.3.3 Argument for PhC Labels in Biological Systems

Researchers already use many types of visualization markers to understand biological systems. For example, green fluorescent protein is used to identify cells that have expressed a certain gene. Quantum dots and some fluorescent dyes are able to bind to the surfaces of cells and other biological elements. Because the chemistry of the attachment depends on the target and the ligands on the quantum dots or dyes, the binding can be

very specific. This allows researchers to identify types of cells, like cancer cells.

Some researchers have used cellular barcoding to keep track of the behavior of certain cells. For example, barcoding has been mostly been used to track cell lineage, and has also provided insight on the migration of various cells throughout the body [71] [23]. In both papers, retroviral DNA vectors were used as cellular barcodes. In order to analyze the results, a sample of the cells of interest is taken, and the barcode DNA must be amplified via PCR. Gerrits et al. sequenced the DNA to determine which barcode the cell obtained [23]. Schepers et al. labeled the DNA with Cy3 and Cy5 fluorescent particles and measured the fluorescence signal, which was corrected against an artificial background distribution [71].

These labels generally are minimally invasive, and are widely used for their specific applications. However, none are used to track individual cells. We hope to create devices that will be able to track individual cells as they go through a single-cell analysis platform. Optical devices would be preferred over other types of barcodes, because as long as the laser is below a threshold power, reading the barcodes would be non-invasive.

Existing Biological Tags

There are many ideas for biological barcodes. For example, Nicewarner-Pena et al., fabricated long, metal-coated cylindrical barcodes. Since different metals have different reflectivities at a certain wavelength, when observed under the microscope, the stripe will have lighter and darker regions [51]. A large number of barcodes can be made if many types of metals are used, or if the number of segments is increased. However, differentiating multiple metals is more difficult to recognize by eye, since some reflected light off one metal might appear similar to other metals. These barcodes would need an intensity-dependent decoding, so the system is more prone to error. Furthermore, the particles are metal-based, and may interfere with cell functions.

Many have functionalized polystyrene beads with multiple small fluorescent particles, in order to create unique barcodes [5] [91]. Depending on the number of different photoluminescent particles N, the spheres can be labeled in 2^N ways. If we also use m different intensity levels to distinguish between different barcodes, there could be m^N different barcodes. The advantage of these barcodes is all of the required are well understood. However, if fluorescent dyes are used, there are issues with chemical stability, as well as photobleaching, photoquenching, and photoinstabiity. Furthermore, the spectral line widths are usually quite broad, so not as many types of fluorophores can be used without overlap. If quantum dots are used on the microspheres, the issues with chemical stability are ameliorated. The spectral linewidths are also narrower compared to those of fluorescent dyes, with a FWHM of about 20 nm. However, they still undergo

photobleaching, so intensity-dependent readings might be inaccurate. One other major concern is the toxicity of quantum dots.

Resin beads have also been encoded with polymers that have various functional groups [20] [73]. The various functional groups had unique Raman spectra, such that by using deconvolution techniques, the functional groups present on each bead could be determined. However, Raman signal tends to weak and prone to interference, since most molecules produce a Raman signal. Certain transitions can be enhanced by SERS (surface-enhanced Raman spectroscopy), but it likely would not be sufficient on a large scale.

Nanoporous particles made from alumina and silicon also can be used as barcodes. Both materials reportedly are non-toxic to living cells [66] [69]. Both also have broad photoluminescence (PL) curves, which show distinct peaks that result from structural resonances. In the case of the alumina thin films, the oscillations in the PL spectrum are a result of Fabry-Perot resonances between the air-alumina-aluminum interfaces of the films [69]. In the case of the silicon microspheres, the resonances are whispering gallery mode resonances [66]. Unfortunately for the 2D film, since the resonances are Fabry-Perot based, the location of the resonant peaks will change depending on the orientation of the film with respect to the excitation source [30]. For the nanoporous silicon particles, because they are spherical and excited resonances are whispering gallery modes, the peaks are independent of the angle of incidence. Unfortunately, the synthesis of these materials is not well understood, and also quite expensive [66].

One barcode uses rugate patterning to create a frequency specific reflection [11]. The line width of the peak is about 11 nm, which is narrower than typical line widths for quantum dots and other fluorophores. Each barcode also can be engineered to have multiple resonant frequencies. Therefore, the total number of codes is 2^N, where N is the differentiable rugate patterns. Unfortunately, the spectral response is affected by the orientation of the film with respect to the incident light source, so if the label changes orientation, the barcode will be misread.

Some have made more complex barcodes, such as an RF chip that emits a binary code when pulsed with electromagnetic radiation [49] [52]. Since the code is given in time, it is not limited to constraints on the length of the code. However, this chip is an active device, and it requires electronics to work properly. Therefore, the chip itself will be difficult to integrate into a biological system due to size. RF electromagnetic radiation also might interfere with cell function.

In summary, there are two main types of optical encoding: image-based encoding and spectrometric encoding. Image encoding allows for easy visual identification of each barcode. However, it is generally more difficult to perform computations on these types of barcodes. Spectrometric encoding uses wavelength

Table 1.2: Example Biological Barcode Technologies

Barcode Description	**Barcode Type**	**Size**	**Spectral Line Width**	**Number of Codes**
Metal-coated cylindrical particles [51]	Visual	0.2μm x 0.2μm x 6.5μm	–	N^m [a]
Microscopic beads encoded with fluorophores beads [5]	Spectroscopic (Visible)	100μm diameter sphere	35 nm to 100 nm (asymmetric) [68]	2^N
Microscopic beads encoded with quantum dots [91]	Spectroscopic (Visible)	10μm diameter sphere	20 nm to 90 nm [7] [68]	m^N [b]
Microscopic beads encoded with inorganic pigments [93]	Visual	0.3 μm - 6 mm	–	N
Resin beads with varied functional groups [20] [73]	Spectroscopic (Raman)	likely 1 μm	–	2^N
Nanoporous anodic alumina [69]	Spectroscopic (Visible)	2D thin-film	about 5 nm	$< 2^N$
Porous-silicon photonic crystals [11]	Spectroscopic (Vis-NIR)	94 mm x 94 mm x 5 mm	11 nm	2^N
Silicon colloid Microcavities [66]	Spectroscopic (NIR)	4.1 μm diameter sphere	1 nm	$< 2^N$
Radio-frequency (RF) tags in polymer capsule [49] [52]	RF	8 mm x 1 mm x 1 mm	–	2^N [c]
Goals for this work	Spectroscopic	10 μm x 10 μm x 220 nm	< 0.5 nm	2^N

Unless otherwise marked, N corresponds to the number of distinct units (e.g. fluorophores) possible.
[a] m = number of segments along the barcode.
[b] m = number of intensity levels.
[c] Here, N is the number of bits in the sequence, in time.

specific features. Though these methods generally rely on more expensive equipment, like wavelength specific detectors or lasers, the deconvolution of many spectra is simple computationally.

The barcode technologies mentioned above are summarized in Table 1.2. The main disadvantages of many barcode technologies are the wide spectral linewidths, intensity dependence, and orientation dependence. The photoluminescence-based labels (like fluorophores and quantum dots) have wide spectral peaks because of thermal broadening and also undergo changes in emitted intensity due to photobleaching [68]. Plasmonic

antennas also tend have wide spectral features [2], and the metal particles, perhaps with the exception of platinum, will disturb cell function [36]. Simple dielectric stack structures [69] [11] do not have in-plane resonances, so the resonant frequency peaks will change relative to the tilt of the cavity with respect to the input beam. Therefore, they are not useful as tags for individual cells.

Photonic Crystal Resonant Cavity Barcodes

Photonic crystal resonant cavities, which will be made of silicon and silicon dioxide, are chemically and optically stable in most constant environments. The resonances are in-plane, so the resonant frequencies of the cavity do not change; only the intensity does. To avoid needing to rely on the intensity of the resonant peaks when building a barcode library, the line-widths of the resonances must be very small. Many researchers have developed PhC resonant cavities with line-widths of less than 0.1 nm.

Photonic crystals resonant cavities are interesting because their resonant peaks have narrow line-widths despite having a small foot print. The peak line-width corresponds to the peak's quality factor Q, which is defined as $Q = \omega/\Delta\omega = \lambda/\Delta\lambda$. Here, ω and λ are the resonant frequency and wavelength, respectively, while $\Delta\omega$ and $\Delta\omega$ are the line-widths in frequency and wavelength, respectively. Using CMOS fabrication techniques, it is possible to fabricate a chip with Q's as high as 10^5 on the order of tens of microns.

However, a tens of microns is still quite large on a biological scale. Inserting the chip into the cell passively will be challenging, and will likely disrupt cell function. Studies have shown that gold nanoparticles greater than 50 nm show a decreasing probability of being absorbed by a HeLa cell [9]. Furthermore, nonspherical gold nanoparticles have a lower probability of being absorbed. Actively inserting the cell may be possible with larger cells, like macrophages and neurons. We may have a higher chance of attaching the barcodes to the cell wall. Iron oxide-doped latex particles 0.83 μm in diameter have been successfully attached to the cell wall of lymphocytes [62].

In addition to the size issue, there are many other concerns that need to be addressed when integrating a silicon micro-chip with a cell. For example, how can the chip be attached to a cell? Will attaching a semiconducting microparticle to the outside of the cell affect its behavior? Clearly, the biological aspect of this project still requires extensive research. These questions are outside the scope of this thesis, but are important to consider if the use of PhCs as biological barcodes will be pursued.

However, as mentioned, tagging individual cells is not the only application for barcodes in biology. Many of the encoded microsphere types presented above are 0.3 microns to 6 mm in diameter [93]. The larger spheres are used for multiplex immunoassays, since more combinations of markers can be made on the larger

Table 1.3: PhC Cavities with Vertical Emission

This table lists PhC cavities that show strong vertical emission. The * marks that the results presented were simulation results.

Author	Cavity Design	Quality Factor	Line Width FWHM (nm)	Modal Volume	Coupling Efficiency
Painter [56]	H1 dipole	250	6	0.03 μm^3	–
Kim* [37]	H1 hexapole	20000	0.075	–	0.325
Tran [82]	L3 and L5	39000	0.040	–	0.3-0.4
Haddidi [27]	L3	10000	1.5	–	0.15
Takagi [77]	H1 dipole	25000	0.038	$0.47(\lambda/n)^3$	0.38
Deotare [12]	5-hole taper in nanobeam	750000	0.002	$0.39(\lambda/n)^3$	–

surface area. Photonic crystals can easily be less than 6 mm in diameter, so they could also be used for labeling multiplex immunoassays.

Previous Work in Free Space Photonic Crystals

In order to use photonic crystal resonator cavities as barcodes, we need to couple light from free-space into and out of the resonant mode of the crystals. The resonant mode causes some of the light to be back scattered, but the polarization of the back-scattered light is determined by the orientation of the crystal. Therefore, it can be differentiated from the specular reflection from the incident light by filtering.

There has been significant work done already on improving the vertical emission of light from photonic crystals for nonbiological applications, such as photonic crystal lasers [56], cavity quantum electrodynamics [85]. Researchers optimize cavities to increase the quality factor Q, increase the output coupling efficiency, and decrease the modal volume V. Because of time reciprocity symmetry, if a light source centered in the middle of the resonant cavity can radiate power into the far-field, then light that is able incident on the cavity from free space should be able to be excite the resonant mode of the cavity. Therefore, their photonic crystal cavity designs can be used for our back-scattering application.

In 1999, Painter et al. published a paper reporting the first photonic crystal laser [56]. The cavity was a single hole missing from a hexagonal lattice of air holes in a thin InGaAsP membrane, and 2 holes on opposite sides of the cavity were enlarged to break the degeneracy of the resonant dipole modes. The resonant cavity had a low Q-factor of 250, which could be increased further by optimizing the cavity.

Kim et al. discussed modifications that could be made to increase the out-coupling of the many resonant

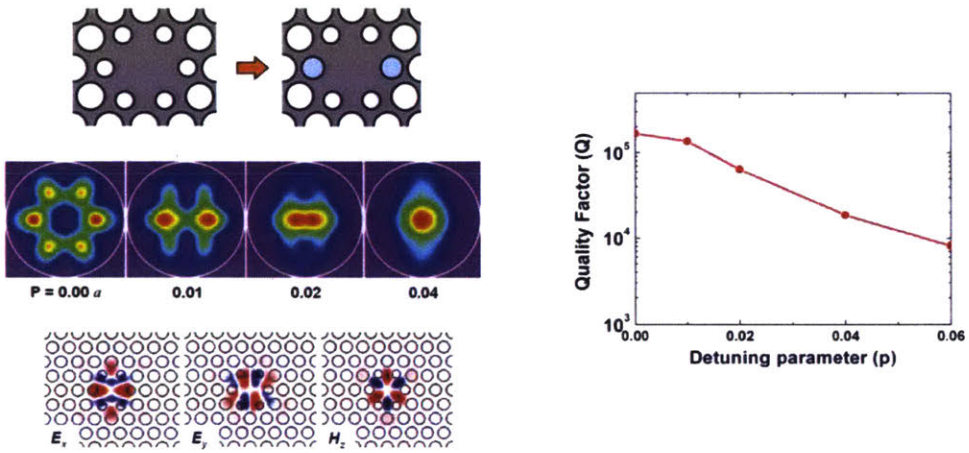

Figure 1.3: Cavity Modifications and Far-field Effects
By slightly modifying the size and position of the holes around the defect cavity, the far-field radiation pattern can be engineered to have vertical emission. All figures are from Kim's paper [37].

cavity modes of the single defect cavity [37]. They observed in their simulations that by slightly modifying 2 holes on opposite sides of the cavity, the far-field radiation pattern could be shaped to nearly vertical emission. They optimized their cavity design for the hexapole resonant mode, which they claimed had a higher Q. Having a high Q generally means that the radiation loss (and out-coupling efficiency) is low. However, as expected, as they modified the 2 holes, the quality factor of the cavity dropped and became comparable to the Q's of the dipole and the monopole.

Since the far-field pattern can change significantly with seemingly nearly identical near-field patterns, Kim's technique of just modifying 2 holes means the radiation pattern sensitive to disorder [82]. Tran et al. proposed band-folding, a more robust method of improving the vertical emission of light from a resonant cavity [82]. Using band-folding, they designed a 5-hole cavity with a theoretical Q of about 39000 and efficient vertical out-coupling. The measured Q was about 25000. Band-folding is achieved by introducing a periodicity of $2a$, where a is the lattice constant of the photonic crystal, right next to the defect, as shown in Figure 1.4. The wavevector of the unperturbed resonant mode is usually near $k = \pi/a$. The doubled periodicity halves the corresponding maximum k-vector to $k = \pi/2a$, creating another line of symmetry. To maintain symmetry, some of the light was previously confined in the crystal with $k \approx \pi/a$ appears at $k = 0$. The light at $k = 0$ is above the light line, so it is radiated out from the cavity.

Haddidi et al. presented work on a 3-hole cavity variant with band-folding in an InP membrance, which had a coupling efficiency of 15% and quality factor greater than 10000 [27]. Furthermore, Haddidi observed

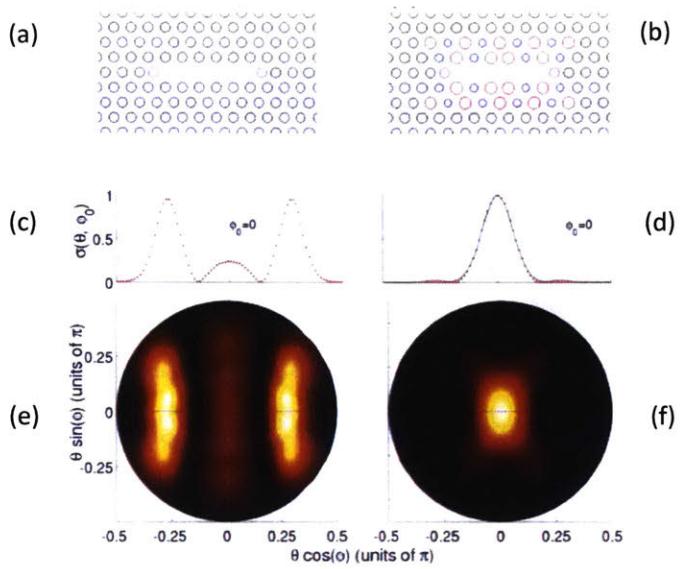

Figure 1.4: Out-coupling from PhC Resonant Cavity
(a, b) These figures show the resonant cavity structure. (c, d) These figures show the radiated power as a function θ at $\phi = 0$, while (e, f) show a 2D map of the power radiation. Pictures (a), (c), and (e) correspond to a cavity without band folding, while pictures (b), (d) and (f) correspond to a cavity with band folding. It is clear that band folding helps increase emission from the cavity. All figures are from Tran's paper [82].

Fano resonances that resulted from multiple vertical reflections as they coupled light into the cavity. Fano resonances could reduce the effective width of the resonance peak, allowing for even higher resolution of barcodes.

Takagi et al. used the dipole mode to generate high Q H1 photonic crystal cavities [77]. Their photonic crystals were suspended in air, and had a high dielectric constant of 11.96. By making small shifts in the holes within three lattice periods of the defect, they were able to engineer devices that showed experimentally Q factors of about 25000, and an external coupling efficiency of 0.38.

Deotare et al. showed that high extraction efficiencies can be achieved in a 1D silicon photonic crystal as well [12]. Their photonic crystals were on suspended nanobeams, so higher Q factors are expected, and they were able to obtain Q factors of about 750000. Deotare's work is suggestive that completely detached barcodes may be able to obtain high Q factors as well.

These references clearly shown that spectral line widths of less than 0.1 nm should be acheivable with photonic crystal cavities. To bridge the biological barcode field to the photonic crystal field, we will focus on recreating the photonic crystal cavities in CMOS, and detect the back-scattered fields from the resonators.

Since we are interested in the physical size of the scatterer as well, we will observe how many mirror holes are needed to maintain the high Q modes. We chose to first work with the cavities presented by Tran and Haddidi to achieve high Q and efficient out-coupling despite the larger modal volume.

1.4 Introduction to Silicon Photonic Modulators

1.4.1 The Proposed Technology

The previous set of technologies were passive devices that we could gain information from by observing how the incident light was scattered as a function of wavelength. In this last device, we use an electrical signal to change the refractive index of PhCs. By applying an electric current, the transmission of light is either increased or decreased at a given wavelength. This allows us to transfer binary information from an electrical signal onto a optical signal.

The motivation for transferring information onto an optical signal is to increase computation bandwidth while not greatly increasing power requirements. Therefore, these EO modulators need to operate on minimal amounts of energy, work well even at high bit rates, and generate a readable binary optical signal (usually defined to be 3 dB or 50% extinction). Modulators with 3 dB extinction can already operate at about 3 fJ/bit, requiring only 1V peak-to-peak, while transmitting data at 12.5 Gbits/s. Though our modulators as of now have not been as carefully optimized, we hope that by employing Fano resonances, we can also achieve similar or better numbers.

1.4.2 Motivation for Optical Interconnects

Microprocessors of the past decade dissipate approximately 100 W of power on average. It is estimated that 60% of the power is from computation, 20% is from on-chip communication, and the last 20% is from off-chip communication [53] [10]. If 60 W of power is used for computation, and the target energy cost of one FLOP (floating point operation) is 10 pJ/FLOP [53], a processor can operate at 6 TFLOPs per second. If the processor accesses memory at the targeted goal of 1 byte per FLOP, the read and write paths would each require 48 Tbit/s link bandwidth; together they would require 96 Tbit/s bandwidth. Therefore, off-chip communication would ideally be able to operate at 96 Tbit/s while using less than 20 W of power.

As single channels are likely to continue operating at around 8-12 Gbit/s (Gbps) to maintain energy efficiency of computation (assuming the computation clock rate stays at around 2-3 GHz) [53], a 96 Tbit/s bandwidth can only be achieved by employing parallel channels. It is here that optical channels have a large

advantage over electrical channels. Orcutt estimates that there would be 2000 electrical channels available for use (given optimistic power, cost, and manufacturing constraints), which would only be able to provide a total bandwidth of 20 Tbit/s [53]. On the other hand, optical links could employ wavelength-division multiplexing and its high carrier frequency to reduce the number of overall channels required.

However, energy costs also need to be considered. If the electrical links operated at 0.5 pJ/bit, an optimistic goal, [53] operating at 96 Tbps would require 24 W of power. For optical links, even though the number of channels can be reduced, 9600 modulators still needs to be considered, if all modulators are operated independent of each other. That means, still assuming a 20 W budget and operation at 10 Gbps, each modulator can only use 200 fJ/bit. Orcutt proposed distributing the energy per photonic link as 100fJ/bit for thermal tuning, 40 fJ/bit for modulation, and 50fJ/bit for detection [53]. This distribution also leaves 1 W for powering optical sources.

The amount of energy per bit allotted for modulation seems generous. However, in addition to turning on and off the modulator, additional energy is needed to interface the modulator with other electronic components. For core-to-memory links, operating the modulator and interfacing with microprocessor can theoretically cost around 40 fJ/bit altogether [53]. According to Orcutt's estimations, modulation itself could require only 3 fJ/bit, while the electronics that interface the modulator with the memory may require the remainder. However, the target of 40 fJ/bit is significantly lower than the best reported transmitter efficiency of 70 fJ/bit [16]. The transmitter used by Georgas used a modulator that exhibited 8 dB extinction at 3.5 Gbps.

1.4.3 Argument for Photonic Crystal Modulators

Photonic crystal (PhC) modulators are typically 1D photonic crystals patterned on a waveguide. The waveguide confines the light in 2 directions, and the photonic crystal structure imposes boundary conditions in the third direction, the direction of propagation. In contrast to the resonant scatterers, the resonant cavities here are coupled to an input and output bus waveguide, and we are interested in the transmission of light through the entire structure. The transmission spectrum is generally Lorentzian in shape, with the maximum at the resonant wavelength.

PhC modulators are modulated by changes in the index of refraction. By changing the index of the waveguide, the resonant frequency of the PhC cavity also changes. Depending on the wavelength of the input laser, the transmission will either increase or decrease. The change in index is usually obtained by applying a voltage and changing the density of electrons in the material. There are two types of electrical

Table 1.4: State of the Art Modulators

Summary of recently developed modulators in silicon.

Author	Type	Extinction	Voltage	Speed	Energy	Operation Mode
Green [25]	MZI	6 dB	7.6 V	10 Gbps	5 pJ/bit	Injection
Thomson [14]	MZI	3.1 dB	6.5 V	50 Gbps	4.2 pJ/bit	Depletion
Xu [19]	Ring	9 dB	3.5 V	12.5 Gbps	300 fJ/bit	Injection
Dong [18]	Ring	8 dB	1 V	12.5 GHz	10 fJ/bit	Depletion
Watts [17]	Disk	3 dB	1 V	12.5 Gbps	3 fJ/bit	Depletion
Tanabe [79]	PhC	10 dB	3 V	500 MHz	3 fJ/bit	Injection
Timurdogan [80]	Ring	6.18 dB	0.5 V	25 Gbps	0.9 fJ/bit	Depletion

modulation: carrier injection modulation and carrier depletion modulation. These two types of modulation are discussed further in the Appendix. Generally, carrier depletion modulation is favored because of lower capacitance and thermal heating. However, because the change in the number of electrons is smaller, the modulator is less sensitive to carrier depletion.

Compared to other EO modulators, PhC resonant modulators can potentially be operable at higher frequencies while consuming less energy. In photonic crystal resonator cavities, the resonant field is localized at the defect, which only needs to be on the order of several hundred nanometers in length. Because of this, PhC resonant cavities are able to maintain high Q factors that are localized in a small volume, compared to other modulators. A higher quality factor allows for a lower peak-to-peak driving voltage for modulation with a given extinction (on-off) ratio. A smaller modal volume allows for smaller p-n or p-i-n junctions and smaller electrical contacts compared to those used for other modulators.

The energy required for a modulator is $E_{bit} = \frac{1}{4}C_{on}V_{on}^2 + \frac{1}{4}C_{off}V_{off}^2 + \frac{I_{on}+I_{off}}{2}R_s$ where C is the junction capacitance, V is the applied voltage, I is the current through the diode, and R_s is the series resistance of the diode. The 3dB high frequency cut-off frequency for an RC-type circuit is $\frac{1}{RC}$. Therefore, having an electrical junction with a smaller cross-sectional area reduces the capacitance of the diode. The modulator should be able to run at higher frequencies while maintaining comparable gain and operate at lower energies per bit.

The current state of the art in modulator technology is summarized in Table 1.4. The modulator that shows the best performance so far operates at 0.9 fJ/bit at 25 Gbps, requiring only 0.5V AC peak-to-peak, and exhibits 6.2 dB extinction [80].

Modulators that use photonic crystal (PhC) resonant cavities with success comparable to other resonant

structure modulators have yet to be reported. However, in the past year there was a paper on the simulation results of a photonic crystal modulator design, which claimed that 6 dB modulation depth at 25-50 Gbps while only applying 0.6 V peak-to-peak is possible [29]. If the theoretical model can be supported with experimental results, this PhC design would be competitive with the modulator reported by Timurdogan et al., and potentially could show even lower energy per bit costs due to the reduced junction area. Hendrickson claims that the PhC modulator could have energy costs as low as 14 aJ/bit.

1.5 Introduction to Photonic Crystals

1.5.1 Brief Introduction to Photonic Crystals

Photonic crystals are composite materials in which the dielectric constant varies periodically on the order of the wavelength. Due to boundary conditions on Maxwell's equations, the periodicity results in optical bands and band gaps for incident light, analogous to how the periodic structure of a crystal creates electronic bands and band gaps for electrons. When light of a frequency within the band gap is incident on the crystal, the wave is completely reflected; on the other hand, light not in a band gap can pass through the crystal at a certain speed.

By changing the periodicity, the dielectric constants, the periodic structure, and so on, we are able to control the optical properties of a given structure. One common application of photonic crystals is the design of a resonant cavity, which is created by intentionally introducing a defect in a periodic structure. Just as a chemical impurity in silicon creates an energy level within the band gap, the structural defect creates an allowed state in the photonic band gap. Modes that usually cannot exist in the material but can exist in the defect will resonate locally at the defect location. Since the structures that comprise the photonic crystal are typically sub-wavelength in size, photonic crystals provide a means of designing a resonator with a small footprint but also low loss.

1.5.2 Quality Factor Q of a Resonant Cavity

The quality factor of a resonator is defined as the stored energy W_T divided by the outgoing power P_D at a given frequency ω_0.

$$Q \equiv \omega_0 \frac{W_T}{P_D} \tag{1.19}$$

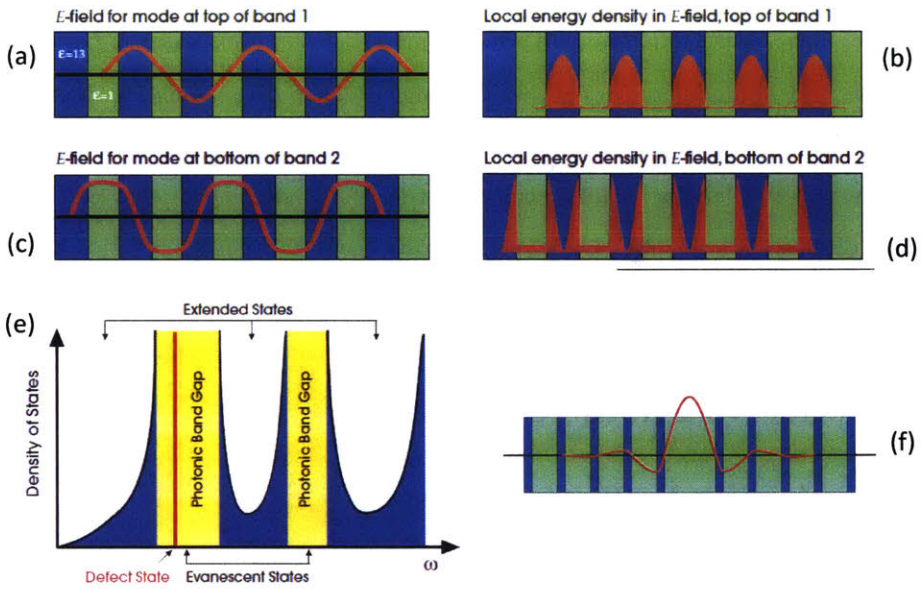

Figure 1.5: Cartoon of Photonic Crystals
(a, b, c, d) These figures show the electric field and their energy density for the first two bands of that periodic structure. Together they show how a periodic structure can create different energy levels at a given wavevector k. (e) This figure shows the bands (through the density of states) and the defect state introduced in a band gap. (f) This is a cartoon of a defect and the localized resonance. All figures are from Joannopolous's book [33]

It can also be expressed as $Q = \frac{\omega}{\Delta\omega}$, where $\Delta\omega$ is the full width half max of the Lorenztian resonance peak, and also as $Q = \frac{\omega}{\gamma}$, where γ describes the decay rate of the stored energy. Since the energy is the square of the field, the field decays exponentially with $\frac{\gamma}{2}$. From the last equation defining Q, we see that Q is directly related to the how well the field stays confined inside the resonant cavity. Radiation and coupling to other sources are also loss mechanisms, so cavities with efficienct out-coupling tend to have lower Qs.

Typically, the electric field of the resonant mode is defined to decay exponentially with $\frac{1}{\tau}$. Therefore, we can define γ with respect to the lifetime τ, and then find Q can be written as

$$Q = \frac{\omega_0}{\gamma} = \frac{\omega\tau}{2}. \tag{1.20}$$

There are some variations as to how Q and τ are defined. Consider the case where a resonant cavity field decays through two paths, both with time constant τ. The decay is twice as fast as if there were only one path with time constant τ, so the decay rate $\gamma_2 = 2\gamma = \frac{4}{\tau}$. This makes sense, because we could equivalently argue that by adding a second path, the lifetime τ is cut in half. Additionally, the argument is equivalent to saying that the decay of power of both paths is simply equal to the sum of the decay of power of both

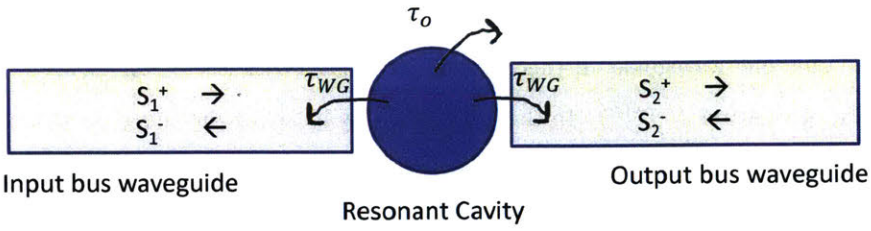

Figure 1.6: Cartoon of Coupled-mode Theory
Cartoon describing coupled-mode theory. The time constant τ_{WG} correspond to coupling from the cavity to the waveguides, and τ_0 corresponds to loss of cavity to everything else. S_l^+ corresponds to an incoming wave and S_l^- corresponds to an outgoing wave [33].

individual paths. Therefore, in this case, we see that

$$Q = \frac{\omega\tau}{4}, \tag{1.21}$$

where Q is the total quality factor of the cavity decaying through both paths, and τ is the lifetime corresponding to the decay of energy into one path.

1.5.3 Temporal Coupled-Mode Theory for Resonant Cavities

Transmission Through the Resonant Cavity

The general behavior of the photonic crystal can be modeled with temporal coupled-mode theory. The localized mode is represented as a cavity with energy $|A|^2$ and resonant frequency ω_0, coupled to the rest of the crystal with an input waveguide and an output waveguide as shown in Figure (1.6)) [33]. The amplitude of the wave going into the cavity along waveguide l is defined as S_l^+ and the amplitude of the wave going away from the cavity along waveguide l is defined as S_l^-. The cavity is coupled to the bus waveguides with coupling constant α_l, and reflects the incoming wave with reflection coefficient β_l. Energy from the cavity decays into waveguide l with a certain time constant τ_l. The temporal coupled-mode can be expressed as

$$\frac{dA}{dt} = -i\omega_0 A - \frac{A}{\tau_1} - \frac{A}{\tau_2} + \alpha_1 S_1^+ + \alpha_2 S_2^+ \tag{1.22}$$

$$S_l^- = \beta_l S_l^+ + \alpha_l A \tag{1.23}$$

If the coupling to the cavity is weak, or, in other words, the coupling between the cavity and waveguide

l does not affect the coupling between the cavity and waveguide j, we can approximate the system as a cavity coupled to only one waveguide. If there are no incoming waves ($S_l^+ = 0$), by solving Equation 1.23, we determine that $A = A(0)\mathrm{e}^{-i\omega_0 t - t/\tau_l}$. In this case, the only place for the energy to decay to is waveguide l, so the change in energy $|A|^2$ is equal to the energy $|S_l^-|^2$. Therefore,

$$-\frac{d|A|^2}{dt} = \frac{2}{\tau_l}|A|^2 = |S_l^-|^2 = \alpha_l^2|A|^2 \tag{1.24}$$

and $\alpha_l = \sqrt{2/\tau_l}$.

Because of time reversal symmetry, if $S_l^- = 0$ and $S_l^+ = \sqrt{2/\tau_l}A$, then $A = A(0)\mathrm{e}^{-i\omega_0 t + t/\tau_l}$. Solving Equation 1.23, we see that $\beta_l = -1$. As expected for weak coupling, all of the incoming wave would be reflected by the cavity (ignoring second-order effects).

Because of the symmetry of the photonic crystal structure at hand, and the fact that there is no source of light traveling towards the cavity through the second waveguide in the system, we can define $S_2^+ = 0$ and $\tau_1 = \tau_2 = \tau_{wg}$. Then, the equations can be simplified to

$$\frac{dA}{dt} = -i\omega_0 A - \frac{A}{\tau_{tot}} + \sqrt{\frac{2}{\tau_{wg}}}S_1^+ \tag{1.25}$$

$$S_2^- = \sqrt{\frac{2}{\tau_{wg}}}A \tag{1.26}$$

where τ_{wg} is the time constant characteristic of the decay of energy of the cavity into each waveguide, and τ_{tot} is the time constant representing all of the losses in the entire system, including the loss to the waveguides, radiative losses, and material losses.

Frequency is conserved in linear systems, so the field in the system oscillates at the same frequency ω as the input. Therefore, $\frac{dA}{dt} = i\omega A$. Solving equation 1.25 for A, we obtain

$$\frac{A}{S_1^+} = \frac{\sqrt{\frac{2}{\tau_{wg}}}}{-i(\omega - \omega_0) + \frac{1}{\tau_{tot}}} \tag{1.27}$$

The amplitude of the transmitted mode at the output is defined as $a_{1o} = \frac{S_2^-}{S_1^+}$, which comes to

$$a_{1o} = \frac{\frac{2}{\tau_{wg}}}{-i(\omega - \omega_0) + \frac{1}{\tau_{tot}}} \tag{1.28}$$

The transmission of a system is defined as $|T| = |a_{1o}|^2 = \frac{|S_2^-|^2}{|S_1^+|^2}$. For this system, the transmission is Lorentzian,

$$T = \frac{(\frac{2}{\tau_{wg}})^2}{(\omega - \omega_0)^2 + (\frac{1}{\tau_{tot}})^2}. \tag{1.29}$$

Relationship between Q and Transmission

Maximum transmission is observed at the resonant frequency ω_0, and is$T_{pk} = (\frac{2/\tau_{wg}}{1/\tau_{tot}})^2$. Relating the lifetimes τ_{wg} and τ_{tot} to their relative quality factors as in equations 1.20and 1.21, we get

$$T_{pk} = (\frac{Q_{tot}}{Q_{wg}})^2. \tag{1.30}$$

We can break down Q_{tot} into its major components: Q_{wg} as defined above, and Q_0, the intrinsic Q that represents the remaining losses of the cavity. Because powers add linearly, and quality factors are defined as the inverse of power, we can express Q_{tot} as $Q_{tot}^{-1} = Q_{wg}^{-1} + Q_0^{-1}$. Now we have

$$T_{pk} = (\frac{Q_0}{Q_{wg} + Q_0})^2. \tag{1.31}$$

From this equation it becomes easy to see that in order to maximize transmission, Q_0 must be much greater than Q_{WG}. In this limit, Q_{tot} is dominated by Q_{WG}. Since we typically desire high Q devices, it is necessary to reduce radiation and material losses in a resonant cavity.

1.5.4 Motivation for CMOS

We will choose to make the photonic crystal devices in CMOS. The indices of refraction of the typical materials used are varied enough to make PhCs with usable optical band gaps in the mid-IR region [46]. CMOS semiconductor processes are also well-characterized, allowing for quick and reliable fabrication of small (<100 nm) structures.

Fabrication in CMOS is precise and easy to reproduce, which is particularly useful when many versions of the device need to be made. For example, in the case of the barcodes, since we are interested in using these to identify a large number (at least hundreds of thousands) of items, being able to manufacture a large number of them quickly and precisely is important to consider.

In the case of the modulator and the diffraction grating, one additional advantage that working in CMOS gives is the potential for easy integration with an electronic platform. For an electro-optical modulator, not

only does this allow for easy incorporation of the PhC resonant cavity with the necessary driving circuitry necessary, it also provides the potential for integrating the system with existing CMOS electronic platforms, and using the modulators as photonic interconnects. The diffraction grating, if fabricated using CMOS processes, could be directly integrated with a camera system. This would save on costs required for additional processing, and help with keeping the size of the spectrometer small.

There already has been some work done with photonic crystals in CMOS. Most of the PhC modulator work done here is based off the preliminary work done by Mehta et al, who fabricated tapered 1D PhC resonant cavities in polysilicon that had a loss of about 4 dB/cm in bulk [15]. In these resonant cavities, the intrinsic quality factors were as high as 58000, ultimately limited by material absorption loss and fabrication disorder. Electrical contacts were also fabricated for these resonant cavity modulators. It was observed that the doped regions increased the lossiness of the cavity, whose intrinsic Q's dropped to around 22000. This observation is consistent with the expected increase of loss due to the increase of free carriers [72]. To prevent the resonant mode from leaking out from the waveguide through the wings that were added for the electrical contacts, the wings were hexagonally patterned with silicon oxide-filled holes.

These works show that fabricating photonic crystals (and other photonic structures) in CMOS is possible and viable, but needs to be optimized further to reduce material absorption losses, especially when the silicon is doped.

1.6 Summary

The overarching theme of this thesis is developing applications in which light interacts with periodic dielectric structures that have features that are on the order the wavelength. The boundary conditions that created by the periodic dielectric constant generate wavelength-dependent optical features that can be used in a wide range of applications. By engineering the periodic dielectric structure, one can create a material with the desired optical properties.

In Chapter 2, we will present work done on performing spectroscopy using the mid-field diffraction pattern past a typical transmission grating. This enables us to miniaturize the spectrometer while maintaining resolution and etendue. The resonant cavity barcodes will be discussed in Chapter 3. We report our experimental results ensuring that measuring the back-scattered light from a photonic crystal is possible. We also show unexpected behavior that could potentially be exploited in the future. Lastly, work on Fano silicon photonic crystal modulators will be presented in Chapter 4. Because of the Fano line-shape's strong

asymmetry, Fano modulators could show improved modulation depth and efficiency. We have not yet tested the performance of the modulators, but we present initial work on designing reliable Fano resonators.

Chapter 2

Lens-free Mid-field Imaging and Spectroscopy

2.1 Overview

The main goal of the mini-spectrometer project is to identify the spectral composition of a diffuse incoherent light source. The light source has a large etendue, as it is spread over a large area and propagates at a wide range of angles. Additionally, the spectrometer would be only a few millimeters in depth, which precludes us from using an internal lens system and far-field diffraction.

Several groups have miniaturized the spectrometer by trading off size for computation. Typically, one trains the spectrometer by creating a library of the expected responses for a range of wavelengths. Given this library and the response of the spectrometer from the unknown light source, one can determine the spectral composition of the light source by solving an inverse matrix problem. The library components must be at least semi-orthogonal to each other in order to be resolved with confidence. One problem with the on-chip designs, which so far have relied on random waveguide coupling, is that the etendue that they are able to measure, which is given by $\pi(\mathrm{NA})^2 A_{slit}$, is significantly reduced. Therefore, a free-space spectrometer is better suited for our application. We choose to investigate the Talbot spectrometer, since one can simply use the fast Fourier Transform (FFT) to determine the spectrum of the light source. In the future, the maximum resolution likely could be increased by using matrix deconvolution techniques. Additionally, understanding the Talbot spectrometer can provide insight on the design of more advanced spectrometers with multiple

diffraction gratings stacked on top of each other.

In the section 2.2, we will discuss the Talbot spectrometer from a theoretical point of view. Specifically, we will discuss the design constraints of the Talbot spectrometer to optimize resolution and maximize signal, and then start to understand how the Talbot effect changes under non-ideal conditions, like an asymmetric grating and a non-collimated light source. In the second section of the chapter, we will discuss experimental results obtained from a first iteration design of the spectrometer.

2.2 Theory of Talbot Spectrometer

As derived in the introduction, the periodicity of the Talbot self-images as one moves away from the gratin in the z direction, is

$$z_T = \frac{\lambda}{1 - \sqrt{1 - \frac{\lambda^2}{d^2}}}, \tag{2.1}$$

where d is the period of the grating. For a given grating periodicity, the Talbot pattern will have a different period depending on the wavelength. For large d, $z_T \approx \frac{2d^2}{\lambda}$.

We hope to measure the Talbot depth in order to determine the wavelength composition of our signal by simply taking the Fourier transform of a single image. Therefore, we will need to detect multiple periods in the z-direction. One method is to use a translational stage and measure variations in intensity as a function of position. Another method is to use a tilted imager, so the different pixels on the image sensor correspond to a different distance to the spectrometer (see Figure 2.1). This second method is advantageous because it avoids the need for moving parts in the system. However, it has other design constraints that we will discuss below.

2.3 Optimizing the Talbot Spectrometer

The Talbot spectrometer that was previously reported [38] only had a resolution of 42 nm. The paper also presented an equation to explain the achievable resolution for the system. However, it doesn't consider the pixel size of the detector. Furthermore, we hope to remove the magnification lens in their system to reduce the size of the system, increase resolution, and increase the etendue of the system. Therefore, here we reanalyze the constraints and limits that the detector imposes.

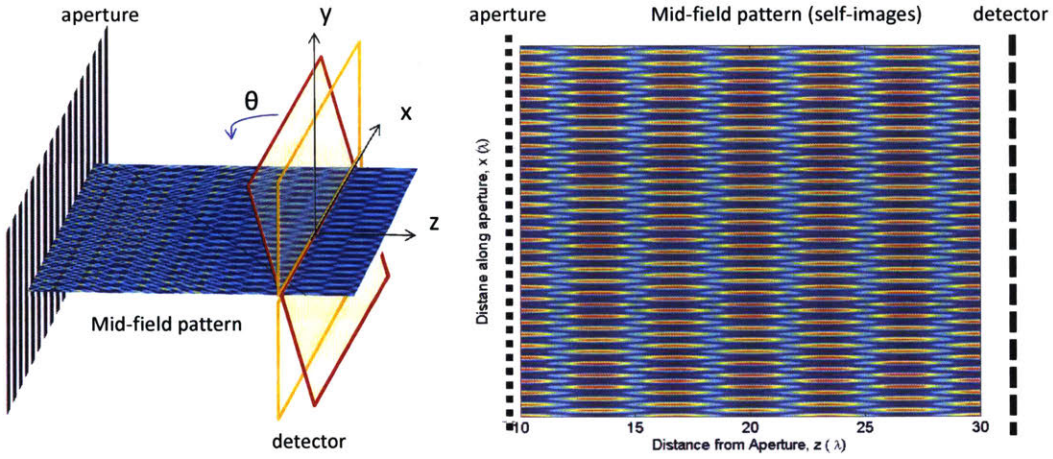

Figure 2.1: Talbot Spectrometer
Cartoon of the Talbot Spectrometer defining the orientation of the detector with respect to the grating. The detector is tilted about the x-axis, while the diffraction orders are propagating in the x-z plane.

2.3.1 Constraint on Grating Periodicity

The mid-field pattern behind a 1D transmission grating is shown in Figure 2.1. The self-images that occur every Talbot distance would appear as alternating strips of high and low intensity lines, corresponding to the teeth of the grating. However, between each of the self-images are the phase-inverted self-images, which have reversed high and low intensity lines. Therefore, when measuring the Talbot periodicity, one can only look at a single point on the along x and observe how it changes in intensity with propagation distance z.

Because the camera detector has pixels of a finite width, some care needs to be taken when choosing the periodicity of the grating, so that the Talbot effect and be detected.

Using Lord Rayleigh's approximation of the Talbot effect, the field behind the grating of grating periodicity d can be expressed as

$$I(x,z) = |A_0|^2 + 4|A_1|^2 \cos(2\pi x/d)^2 + 4A_0A_1 \cos(2\pi x/d)\cos(2\pi z/z_T) \tag{2.2}$$

,where A_0 is the diffraction efficiency of the $m = 0$ diffraction order, and A_1 is the diffraction efficiency of the $m = 1, -1$ diffraction orders. We assume the power detected by a square pixel with pixel length p is given by

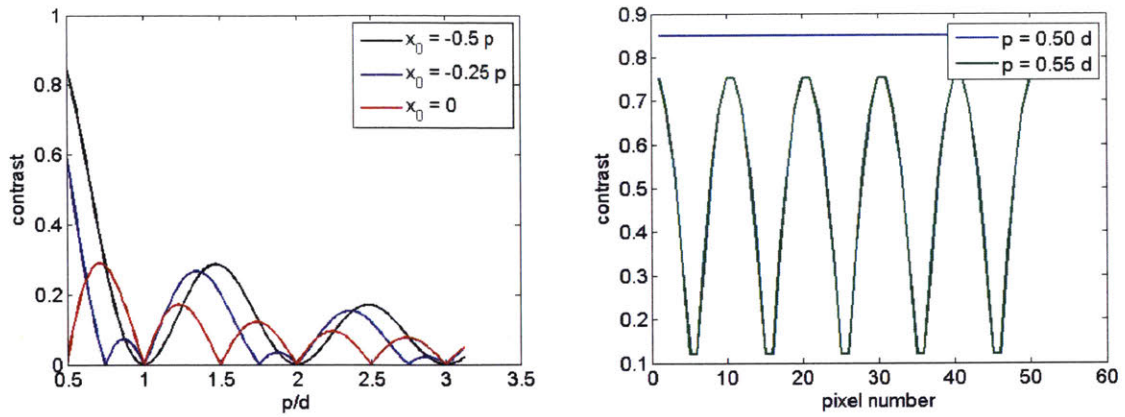

Figure 2.2: Signal Strength vs Pixel Width
p is the pixel length of the detector, and x_0 corresponds to the position of the edge of pixel 0. For $x_0 = -0.5p$, the center of the first pixel is centered at the zero of the x-axis. The grating periodicity was 1.6 μm, and the wavelength was 830 nm.

$$\begin{aligned} P_{pixel} &= \int_{y_0}^{y_0+p}\int_{x_0}^{x_0+p} I(x,z)dxdy \\ &= p[pA_0^2 + 4A_1^2(p/2 + \frac{d\sin(4\pi(p+x_0)/d) - d\sin(4\pi x_0/d)}{8\pi}) \\ &\quad - \frac{dA_0A_1}{\pi}\cos(2\pi z/z_T)(\sin(2\pi x_0/d) - \sin(2\pi(p+x_0)/d))] \end{aligned} \tag{2.3}$$

The term of the equation that gives us information about the Talbot distance is the $\cos(2\pi z/z_T)$ term. At $z = z_T$, we can see the relationship between the detected power of the Talbot effect and pixel length p is

$$P_{pix,Talbot} = \frac{dA_0A_1}{\pi}(\sin(2\pi x_0/d) - \sin(2\pi(p+x_0)/d)) \tag{2.4}$$

First, let's assume that the self-image is centered on the pixel, such that $x_0 = -p/2 + mp$, where m is an arbitary integer. Then, if the pixel width p is an odd multiple of half of the grating periodicity d, then the pixels measuring the Talbot self-images see n peaks and $n-1$ nulls and the pixels measuring the inverted self-images will see $n-1$ peaks and n nulls. Note that this assumes that the peaks from the self-image are centered on the pixel. In contrast, if the pixel width is a multiple of the grating periodicity, each pixel will see n peaks and n nulls–as a result, each pixel will appear the same, and no Talbot distance can be measured.

As expected, the best one could do is to set $n = 1$, so that the pixel width is half the periodicity of the grating, and either measures a single peak or null. However, if the grating is to only have propagating zero

and first diffraction orders for wavelengths longer than 800 nm, the grating periodicity at maximum can be 1600 nm. The width of each peak or null would be approximately 800 nm, and would require a detector with a pixel pitch of just 800 nm. Unfortunately there is no detector with a pixel pitch that small yet.

The next best we could do is to set $n = 2$, and fit 1.5 periods of the self image onto a single pixel. This would correspond to a pixel width of at most 2400 nm, which is reasonable size CMOS pixels. Unfortunately, the measured amplitude of the Talbot effect will be reduced.

Note that in order to maximize the amplitude of the Talbot effect, one needs to have good control over x_0. On the other hand, one will be unable to observe the Talbot effect if p is a multiple of d, regardless of x_0. In the cases when $p \neq m(d/2)$, where m is an arbitrary integer, the measured amplitude of the Talbot effect will vary across the detector (see Figure 2.2 (b)). This actually might be advantageous if one doesn't have precise control of the position of the grating relative to the detector, because it guarantees there will be some signal.

If the desired relationship between the grating and pixel periodicities is not available, one can rotate the grating with respect to the incident beam to reduce the effective grating periodicity to $d\cos\theta$, though this will change the diffraction efficiency of the grating.

2.3.2 Tilt Direction of Detector

We also investigated whether or not the detector should be tilted parallel or perpendicular to the teeth of the grating. Consider a set-up such that the teeth of the grating are oriented vertically along the y-axis. If the detector is rotated about the x-axis, as is shown in Figure 2.1, then the detector samples the Talbot distances along each column, and the grating periodicity along each row. If the detector is tilted around the y-axis, then the detector samples the Talbot distances and grating periodicity simultaneously along each row, and no information is collected along each column.

In terms of complexity, the first option is more attractive than the latter. The original motivation for the second option was that the tilt could allow for the peaks and nulls of the light field to correspond to a single pixel, thereby increasing the detected Talbot signal. Indeed, by integrating over the field at the detector for each pixel, where $z = x\tan\theta$, we see that depending on the tilt of the detector, the contrast of the signal is maximized when the pixel length in x is $1/2$ the periodicity of the grating. However, when looking at the signal actually measured at the detector, as shown in Figure 2.3 (c), we see that signal periodicity does not actually correspond to the Talbot distance we expect to measure (the x's in red).

In favor of simplicity and reliability, we chose to tilt the detector from the vertical axis. However, it may

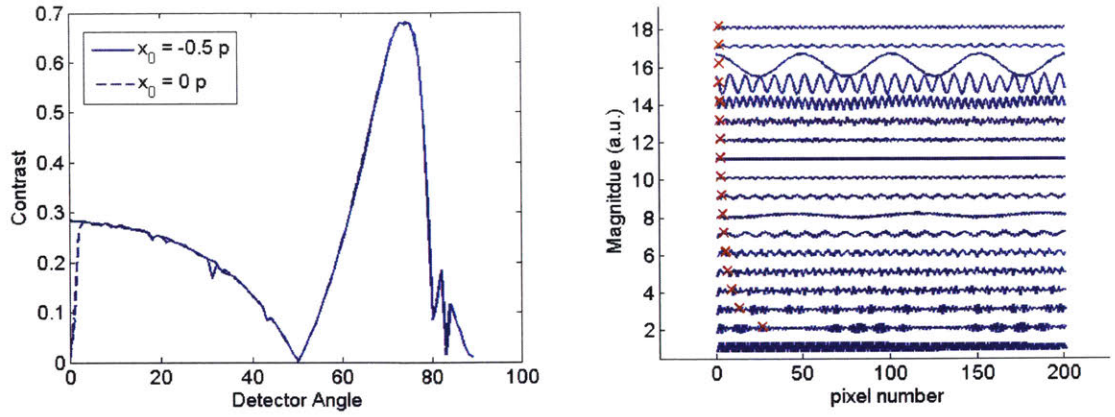

Figure 2.3: Signal Strength vs Detector Tilt around y-axis
(a) Contrast of Talbot signal with respect to DC signal as a function of detector tilt around the y-axis. (b) Detected signal across a row of the detector for increasing detector tilts. The red x's correspond to the expected period on the detector corresponding to the Talbot distance. p is the pixel length of the detector, and x_0 corresponds to the position of the edge of pixel 0. For $x_0 = -0.5p$, the center of the first pixel is centered at the zero of the x-axis. We assumed a grating periodicity of 1.6 μm, a wavelength of 830 nm, and a pixel length of 2.4 μm.

be possible to find an optimal design that uses the horizontal tilting orientation.

2.3.3 Resolution Considerations

Because we use the Fourier Transform to determine the frequency, the resolution of the spectrometer is determined by the number of periods that the detector is able to see. The bandwidth of the spectrometer is determined by the sampling frequency, which can be approximated by the pixel pitch.

The detector can be modeled as a finite series of delta functions. The spacing of the delta functions corresponds to the effective pixel pitch a, and the length of the series is determined by the number of pixels N, or the detector length. This model can be expressed as a train of delta functions with spacing a multiplied by a large rectangle function. In the Fourier space, the system is a train of delta functions with spacing $2\pi/a$ that is convolved with a narrow sinc function.

Let us now also consider a signal with a single Talbot distance z_T. This signal is multiplied onto the detector in real space, so it is convolved with the detector in Fourier space. So, if we look at a single period from $-\pi/a$ from π/a in the Fourier space, then we expect to see two sinc functions at the carrier frequencies $k_T = \pm 2\pi/z_T$. We define the bandwidth of the system to be determined by $k_T = \pi/a$ to avoid aliasing, and the resolution of this effect is determined by the width of the sinc function.

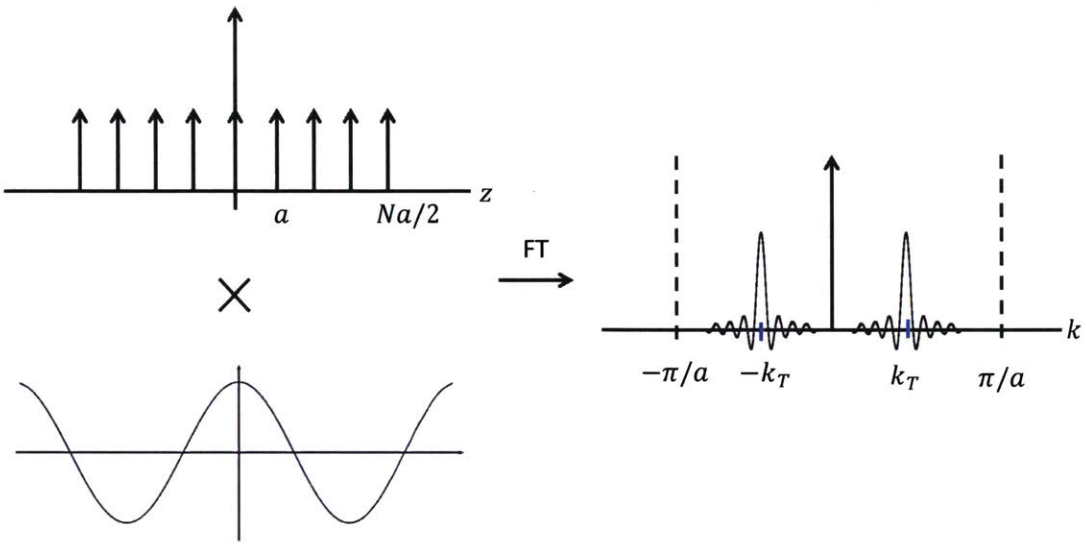

Figure 2.4: Cartoon of System in Fourier Transforms
Cartoon of the detector and Talbot signal in real space and the detected signal in Fourier space.

According the Rayleigh criterion, the next resolvable peak is at the zero of the sinc function. The discrete time fourier transform (DTFT) of a centered box with N discrete elements is $\sin(\Omega(N/2+1/2))/\sin(\Omega/2)$, where $\Omega = \omega a$. Therefore, the sinc has zeros at $\omega(N/2+1/2) = \pi/a$, and is a function of the number of pixels we have in each column of the detector.

The effective pixel length is the length of the pixel in z, and is equal to $p\sin(\theta)$, where p is the actual pixel length, and θ is the angle that the detector is tilted by from the vertical axis. Therefore, the resolution of k_T is

$$\Delta k_T = \frac{2\pi}{(N+1)p\sin\theta} \tag{2.5}$$

and the bandwidth is

$$k_{T,max} = \frac{2\pi}{(p\sin\theta)}. \tag{2.6}$$

Recall that when $d >> \lambda$, where d is the period of the grating, we can make the approximation $z_T = 2d^2/\lambda$. In this case, the wavelength resolution is

$$\Delta\lambda = \frac{2d^2}{(N+1)p\sin\theta}. \tag{2.7}$$

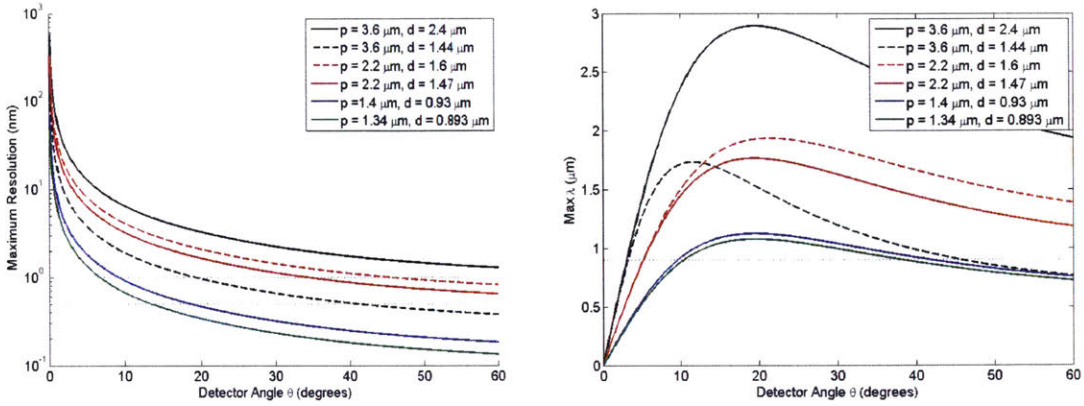

Figure 2.5: Resolution and Bandwidth Limitations for Example Systems
(a) Maximum resolution achievable for a given pixel length p and grating periodicity d as a function of detector angle. (b) Bandwidth for a given pixel length and grating periodicity, as a function of detector angle. The pixel lengths used above are pixel sizes we have access to. The solid curves have $d = 2/3p$ for maximum signal under ideal conditions. The black dashed curve has $d = 2/5p$. The red dashed curve represents parameters from our experimental system.

This equation is consistent with the equation reported by Kung et al [38]. It appears that the minimum resolvable feature decreases with increasing p, so a large pixel size would actually be desirable. This makes sense because having a longer pixel size would enable us to sample more periods of the Talbot effect. However, as discussed above, p is constrained by grating period d, which is constrained by the operating wavelength.

We anticipate not being in the limit $d >> \lambda$, so we solve for the resolution numerically. Sample curves are shown in Figure 2.5.

The bandwidth can be solved for analytically without approximation,

$$\begin{aligned} \lambda_{max} &= \frac{2d^2 + z_{T,max}}{d^2 + z_{T,max}^2} \\ &= \frac{2d^2 p \sin\theta}{d^2 + (p\sin\theta)^2} \end{aligned} \tag{2.8}$$

, and is also shown in Figure 2.5.

Using geometrical arguments, we can also determine the grating size needed for a detector of length L and width W. The Talbot self-images occur when the +1, 0, and -1 diffraction orders overlap, but the Talbot distance can only be measured where either the +1 and 0 or -1 and 0 diffraction orders exist,

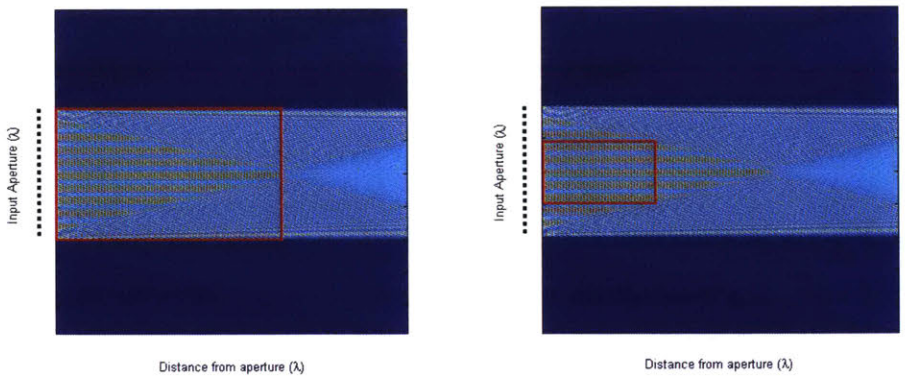

Figure 2.6: Definition of Minimum and Ideal Grating Size
Diagrams show assumed set-up when calculating the minimum grating size and ideal grating size for the system. The box shows the space in the x-z plane that the detector occupies when calculating for the minimum and ideal grating size.

though the strength of the signal will not be as strong. We define the minimum grating size as the size for which the Talbot effect ends just at the farthest point of the detector. In this case, the grating size is $G = 2L\sin\theta\tan\theta_{diff}$, where θ_{diff} is the farfield diffraction angle. This analysis neglects the width of the detector, which enforces that the minimum width of the grating is at least W. We define the ideal grating size as the size for which the entire detector is in the region where the +1, 0, and -1 diffraction orders all exist. In this case, the grating size is $G = 2(L\sin\theta + W/(2\tan\theta_{diff}))\tan\theta_{diff}$. The minimum height of the grating is $L\cos\theta$, though in practice it should be larger to avoid edge effects.

Using these various constraint equations, we can determine the parameters required to obtain a certain resolution. Because the pixel length and grating period are closely related for optimal performance, all the constraints can be expressed in terms of pixel length. Figure 2.7 shows the detector tilt required and corresponding bandwidth as a function of pixel length, for various resolution requirements. The period of the grating is assumed to be $2/3p$. As the graph shows, for a given relationship between d and g, detectors with smaller pixel sizes are needed in order to achieve higher resolution.

2.4 Generalizing the Talbot Effect

Since the above analysis uses the Talbot Effect in its ideal form (e.g. plane wave incidence, symmetric binary grating), we need to investigate the robustness of the Talbot effect.

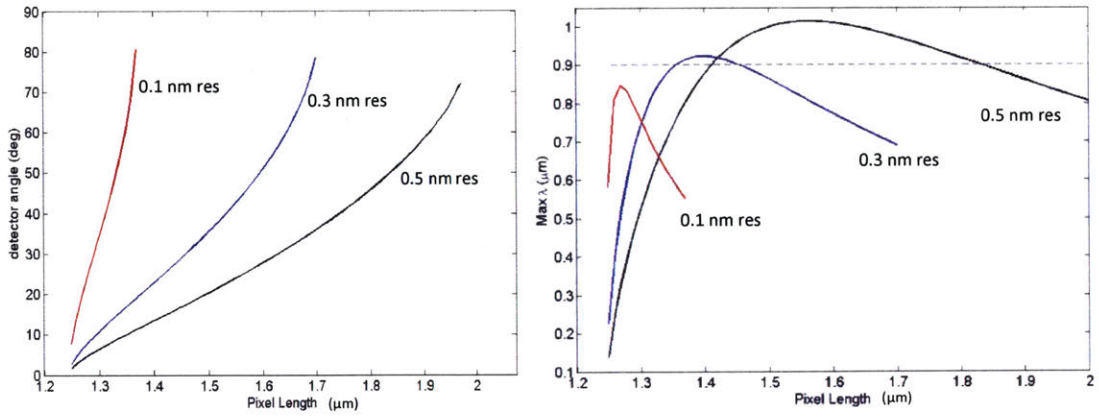

Figure 2.7: Parameters Required to Achieve Certain Resolution
(a) Curves relating pixel pitch to detector tilt required to acheive a certain resolution. Grating periodicity is assumed to be $d = 2/3p$. (b) Corresponding bandwidth of the system with the parameters required to acheive a certain resolution.

2.4.1 Asymmetric Grating

The diffraction efficiency of each diffraction order m is given by A_m. For an asymmetric grating, $A_1 \neq A_{-1}$. The field behind the grating where the three diffraction orders interfere is

$$\begin{aligned} E(x,z,t) =& A_0 \exp(j(\omega t - kz)) + \\ & A_1 \exp(j(k_{\parallel,1}x)) \exp(j(\omega t - k_{\perp,1}z)) + \\ & A_{-1} \exp(-j(k_{\parallel,1}x)) \exp(j(\omega t - k_{\perp,1}z)) \end{aligned} \tag{2.9}$$

Assuming the field amplitudes A_m are real, the intensity of the field is

$$\begin{aligned} I(x,z) =& |A_0|^2 + |A_1|^2 + |A_{-1}|^2 + 2A_1A_{-1}\cos(2k_{\parallel,1}x) + \\ & 2A_0[A_1 + A_{-1}]\cos(k_{\parallel,1}x)\cos((k - k_{\perp,1})z) + \\ & 2A_0[A_1 - A_{-1}]\sin(k_{\parallel,1}x)\sin((k - k_{\perp,1})z) \end{aligned} \tag{2.10}$$

The field intensity is still periodic in z, with a period of z_T.

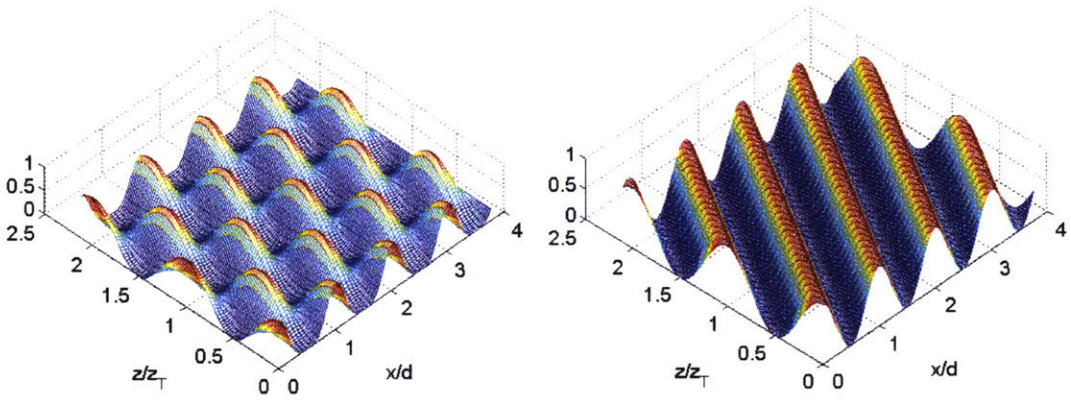

Figure 2.8: Comparison of Symmetric and Asymmetric Grating
Graph shows how the self-images propagate in the case of a (a) symmetric grating, and (b) asymmetric grating.

To maximize the cosine term, with the constraint that $1 = A_0 + A_1 + A_{-1}$, we need $A_0 = 1/2$, while $A_1 = A_{-1} = 1/4$. The amplitude of the cosine is then $1/2$, while the sine term goes to 0. The DC terms equals $1/2$, so the ratio of the Talbot effect to the DC background is 1. To achieve this, we would need a perfect cosine grating.

To maximize the sine term, we need a perfectly asymmetric grating, with $A_0 = 1/2$ and $A_1 = 1/2$ and $A_{-1} = 0$. (A_1 ad A_{-1} are interchangeable). This means the cosine term has an amplitude of $1/2$ and the sine term has an amplitude of $1/2$. The DC terms equal $1/2$.

The only difference between the perfectly asymmetric grating is the lateral shifts of the Talbot self-images. For an asymmetric grating, the self-images shift in x as they propagate in z. For a symmetric grating, the the self-images remain at a constant lateral position. This is shown in Figure 2.8.

Given a diffraction grating, one can optimize the relative angle of the incident beam to maximize the amplitude of the Talbot signal. However, any orientation of the grating will generate the Talbot effect.

2.4.2 Angular Sensitivity

The analysis for the Talbot Effect assumes that the incident light is a perfect plane wave. But, since the light source might not be perfectly collimated, we would like to observe the sensitivity of the Talbot effect with respect to the angular spread of the beam.

First, we should understand the the behavior of the Talbot effect in response to angled incidence. Using

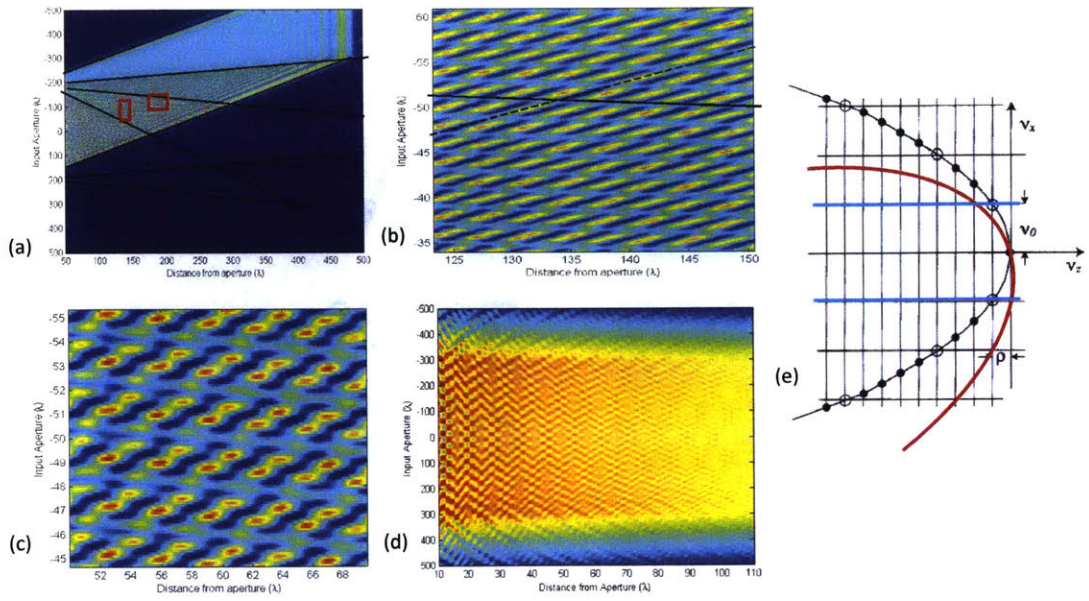

Figure 2.9: Talbot Effect with Angled Incidence
Pictures (a)-(c) show the Talbot effect from angled incidence at different positions and different zoom levels. Picture (d) shows what the detected Talbot effect might look like for a non-collimated beam input (NA = 0.17). Figure (e) shows the k-space diagram of the propagating beam at normal incidence (black) and angled incidence (red). The blue lines are at $k_x = 2\pi/d$ and show the constraint on k_x imposed by the grating. The figure is adapted from [39]

the intuition from Lord Rayleigh's derivation of the effect, we expect the self-images point in the direction of the zeroth order diffraction beam. We simulated this by applying a phase $exp(-j\phi)$ at the grating, where ϕ is the angle of incidence. And indeed, we do see that the self-images are tilted at an angle. In regions with higher diffraction orders, texture within the self-images were observed.

In k-space, the valid combinations of the components of k for a propagating beam at a diffractive medium can be represented by the surface of a sphere, with the origin positioned at the value of the propagating k-vector. For example, if the beam is propagating with $\vec{k} = k_z\hat{z}$, then the origin is at $x = 0$, $y = 0$, and $z = -k_z$. For simplicity, we can consider a 2D system, and if we use the paraxial approximation, the valid solutions of k are represented by a parabola.

The grating puts a constraint on the k_x values the propagating beam can have. As a result, the beam must have a particular k_z, which actually corresponds to the Talbot distance. However, for a beam of angled incidence on the grating, the origin of the circle would be elsewhere, and the same k_x constraint will cause the diffracted beam to have two different values for k_z. If the incident beam has a range of angles, the

diffracted beam will have a range of k_z's, and so the Talbot images will begin to blur together and we will be unable to extract any information from the mid-field diffraction pattern.

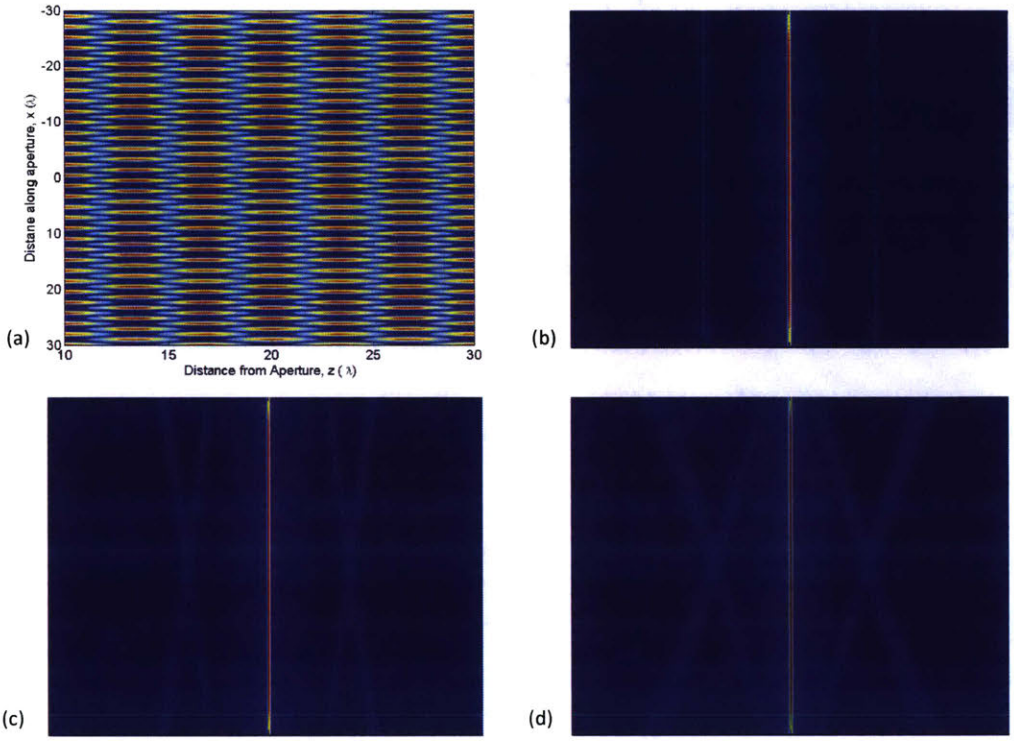

Figure 2.10: FFT of Noncollimated Light Source
(a) shows a zoomed in image of the Talbot self-images for a grating with an acceptance angle of 10 degrees. At this level, no difference is immediately apparent by eye. (b)-(d) show FFTs of the simulated diffraction pattern assuming 0 degree, 4 degree, and 10 degree acceptance angles.

To better understand the behavior of the system with non-collimated light sources, we illuminate the grating (in Matlab) with a point source some distance away, such that the grating has a certain angle of acceptance. Acceptance angle is defined as the angle from normal incidence that the point source makes with respect to the edge of the grating. We assume that the light source is small, so that the response can be represented by a single point source. It turns out that for small acceptance angles, having multiple point sources does not affect the detected pattern significantly, since the phase front at the grating looks approximately the same for each point source.

A summary of the results is in Figure 2.10 and Figure 2.11. From the figures, one can see that increasing the angle of acceptance increases the breadth of the wavelength peak. In particular, the peak tends to be

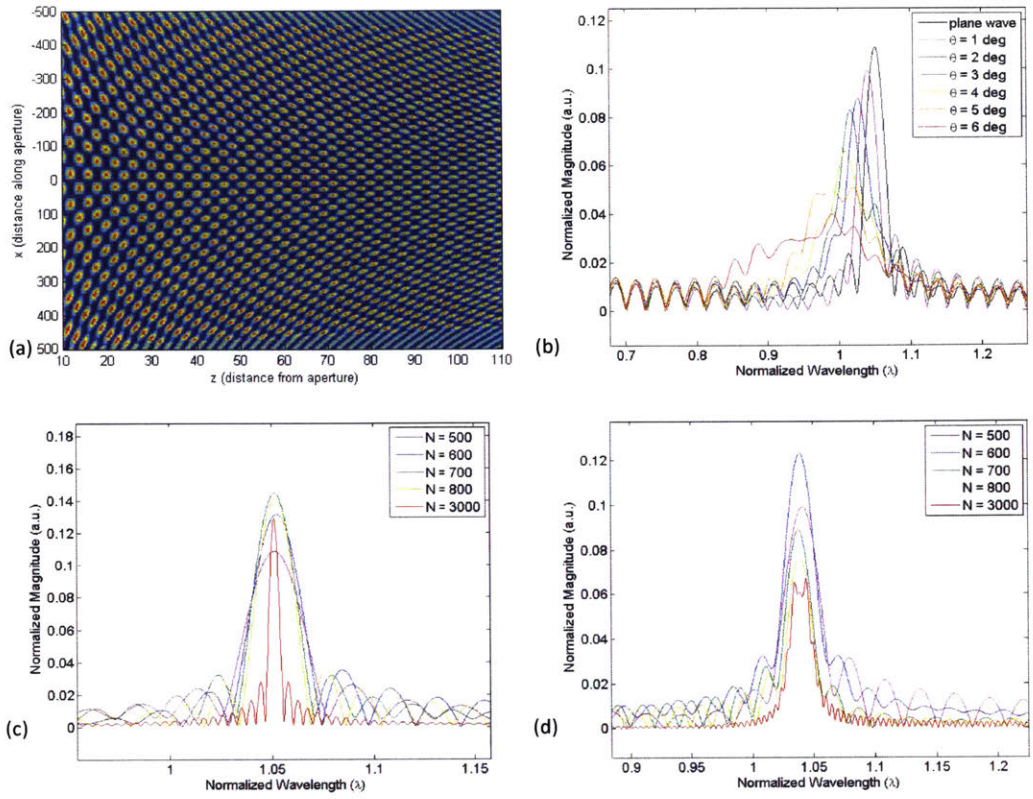

Figure 2.11: Resolution Limits for Noncollimated Light Source
(a) shows a zoomed out image of the Talbot self-images for a grating with an acceptance angle of 10 degrees. Clear warping of the self-images is apparent. (b) shows resolution for a $N = 500$ grating with various acceptance angles. Data was taken from the Fourier transform of a single column of pixels near the center of the grating. (c) shows the limit of resolution as a function of grating size. (d) shows the limit of resolution as a function of grating size. It shows that at some point, the resolution is no longer determined by the size of the grating but by the angle of acceptance instead.

broaden out towards shorter wavelengths.

The FFT images of the entire detector plane show that the response from a spherical wave is well-defined. Therefore, it may be possible to correct the images to remove the spherical phase front, and thereby reduce the peak width of the FFT signal.

2.5 Experimental Section

To prove the concept of a lens-free Talbot spectrometer, we used a binary transmission grating with 622 lines per mm (Ibsen Photonics) with a monochrome Aptina imaging sensor (MT9P031) with a 2.2 μm pixel pitch.

On top of the camera detector is a microlens array and is protected by a glass window. It was purchased with a read-out board from The Imaging Source. The 2.2 μm pixel pitch detector would work best with a grating with a period of 1.47 μm, and absolutely would not work with a grating with a period of 1.1 μm or 2.2 μm (see Figure 2.2). The Ibsen grating, which has a period of 1.6 μm, was the closest commercially available grating that we were able to obtain quickly.

A Ti:Sapphire laser is used in CW mode as the tunable laser source. The beam from the Ti:Sapph is passed through a neutral density filter (OD 4.0), and then focused down using an aspherical lens and spatially filtered using a 50 micron pinhole. The beam was expanded using a 10x beam expander from Thorlabs (GBE10-B). Placing a lens between the pinhole and the beam expander did not greatly affect the measurements, so no lens was used.

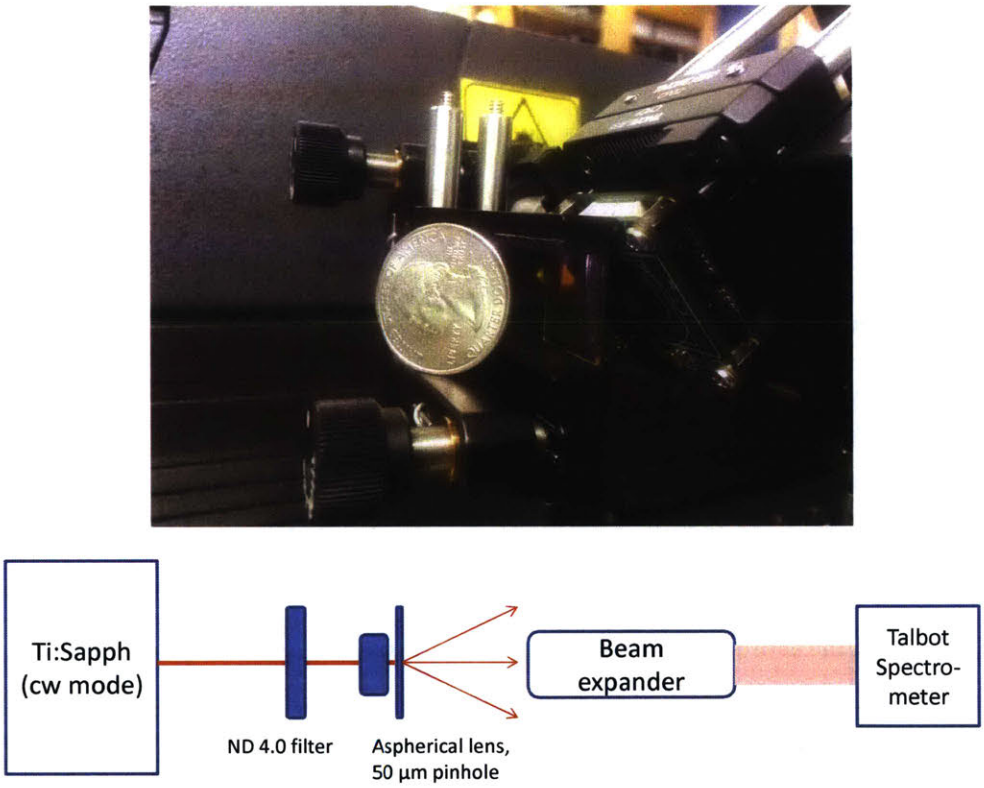

Figure 2.12: Talbot Spectrometer Experimental Set-up
Picture of the Talbot set-up used for our experiments. A cartoon of the optics set-up.

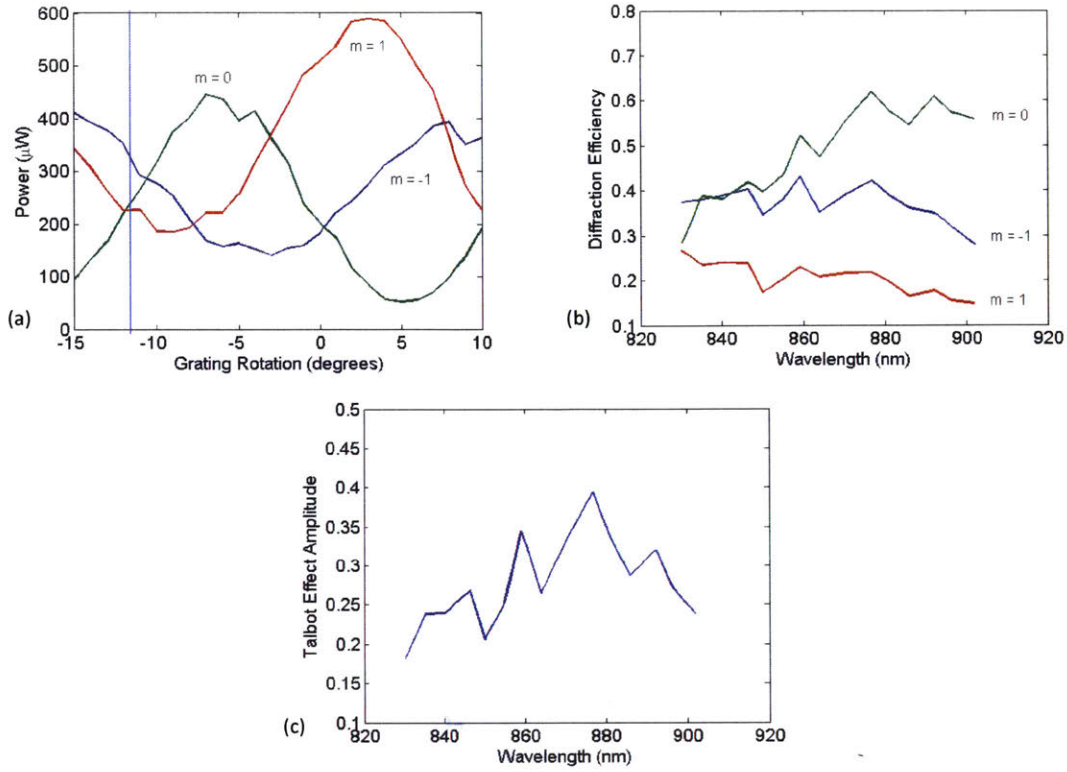

Figure 2.13: Transmission Characterization of Grating
(a) shows the measured powers in farfield for the $m = -1, 0$, and 1 diffraction orders as the grating with respect to the incident beam. Note that the degree of rotation is with respect to a reference point that does not correspond to normal incidence. (b) shows the diffraction efficiency of the three modes as a function of wavelength with the detector was tilted at approximately -11 degrees. The graph on the right is the maximum Talbot signal expected at each wavelength. It is calculated from $A_0(A_1 + A_{-1})$, and shows significant oscillation with wavelength.

2.5.1 Grating Characterization

The grating was characterized by investigating the diffraction efficiency of the $m = -1, 0$, and 1 diffraction orders. The Ti:Sapph beam without any spatial filters was incident on the grating, and the power of each diffraction order was measured roughly 4 inches away using a Thorlabs 5 mW power meter. The diffraction efficiency was first measured as a function of grating rotation with respect to the incident beam. We chose to optimize the grating when the amplitudes of all three diffraction orders have comparable power, with the expectation that at longer wavelengths the zeroth order diffraction efficiency will increase. The measurements are summarized in Figure 2.13.

We see that the diffraction efficiency of each order is not monotonic with wavelength. As a result, the

expected signal for the Talbot effect, which we calculate as $A_0(A_1 + A-1)$, is also not monotonic with wavelength.

2.5.2 Response as a Function of Detector Tilt

When using a laser source, if we zoom into the image so that we can see the individual pixels, we can very clearly see the periodic variations in intensity along each column of the of image (see Figure 2.14). Depending on the angle of the detector relative to the grating, the periodicity changes visibly. Recall from Figure 2.1 that we expect that each column of the detector to independently measure the Talbot distance from the mid-field diffraction pattern. When the detector is parallel to the grating, we expect each column to be alternating light and dark, since it's the self-image of the transmission grating. As we increase the angle, we expect to sample more and more self-imaging planes, and therefore expect the observed periodicity to decrease.

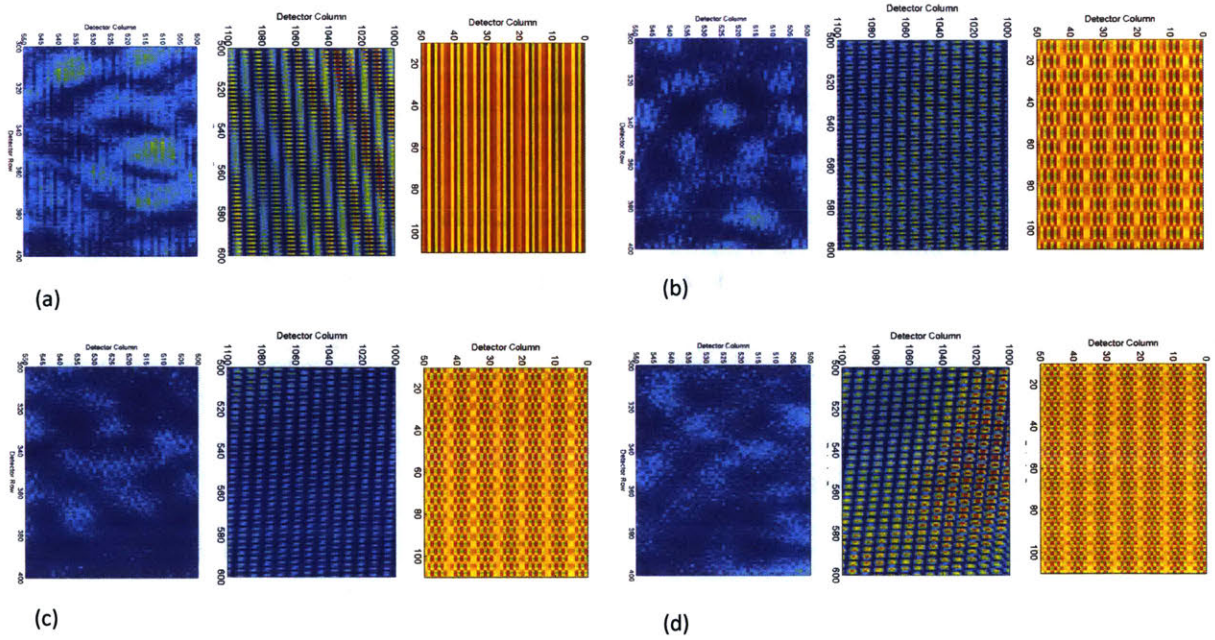

Figure 2.14: Talbot Spectrometer Detector Images
Raw images, images after bandpass filter, and the simulated detector response when the detector is tilted approximately (a) 0 degrees (b) 10 degrees (c) 20 degrees (d) 30 degrees. As the simulated detector images show, in (a), we expect to see alternating light and dark rows, such that the picture resembles the transmission grating. From (b) to (d), along each row of the image, we expect to see higher frequency oscillations as we measure more and more self-images. In the filtered images, there is some horizontally striped artifact

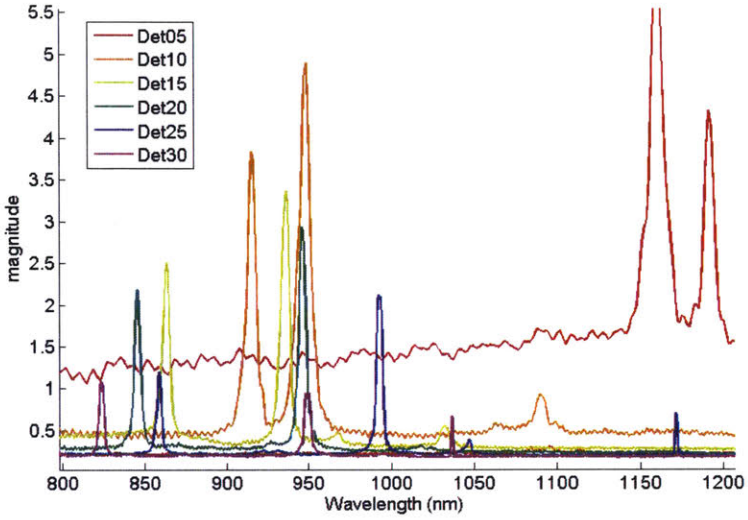

Figure 2.15: Talbot Spectrometer vs. Detector Angle
Spectrum obtained by taking the 1D Fourier Transform along each column of the image.

If we look closely at the image that was taken at 0 degrees, we see that the dark and light lines are not continuous through the entire image. One explanation is that the detector was not at exactly 0 degrees. Another explanations is that the detector was unintentionally rotated about another axis in addition to the x-axis, such that the columns of the detector are not perfectly aligned with the teeth of the grating. Because the current experimental set-up has many degrees of freedom, either or both possibilities are likely factors, and can change every time the system is adjusted.

We can also see a background pattern in the images. The origin of this pattern has not yet been identified, but may suggest that the phase front of the incident beam is not perfect. There seemed to be some issues with the spatial mode of the Ti:Sapph beam, and the optical system most likely could be better aligned to produce a collimated beam at the output. Additionally, it could be a result of crosstalk or back-reflection caused by the microlens array and glass slide cover. Once these issues are accounted for, it's possible that cleaner data could be obtained.

To analyze the image obtained on the detector, we take the 1D FFT of each detector column, and then take the mean of all the columns to reduce the noise in the 1D FFT signal. To convert the x-axis of the FFT data from k_z to λ, we use the equation

$$\lambda = \frac{2d^2(2\pi/k_z)}{d^2 + (2\pi/k_z)^2}. \tag{2.11}$$

When taking the fast Fourier transform along each column of the image (see Figure 2.15), we can identify peaks that correspond to the wavelength of the incident light. As expected, the resolution of the measured frequency increases with the angle of the detector, since the detector is able to sample more periods of the Talbot effect. The calculated wavelength appears to vary with detector angle, but, because there is no consistent trend, the variation in wavelength is likely a result of the uncertainty of the detector angle.

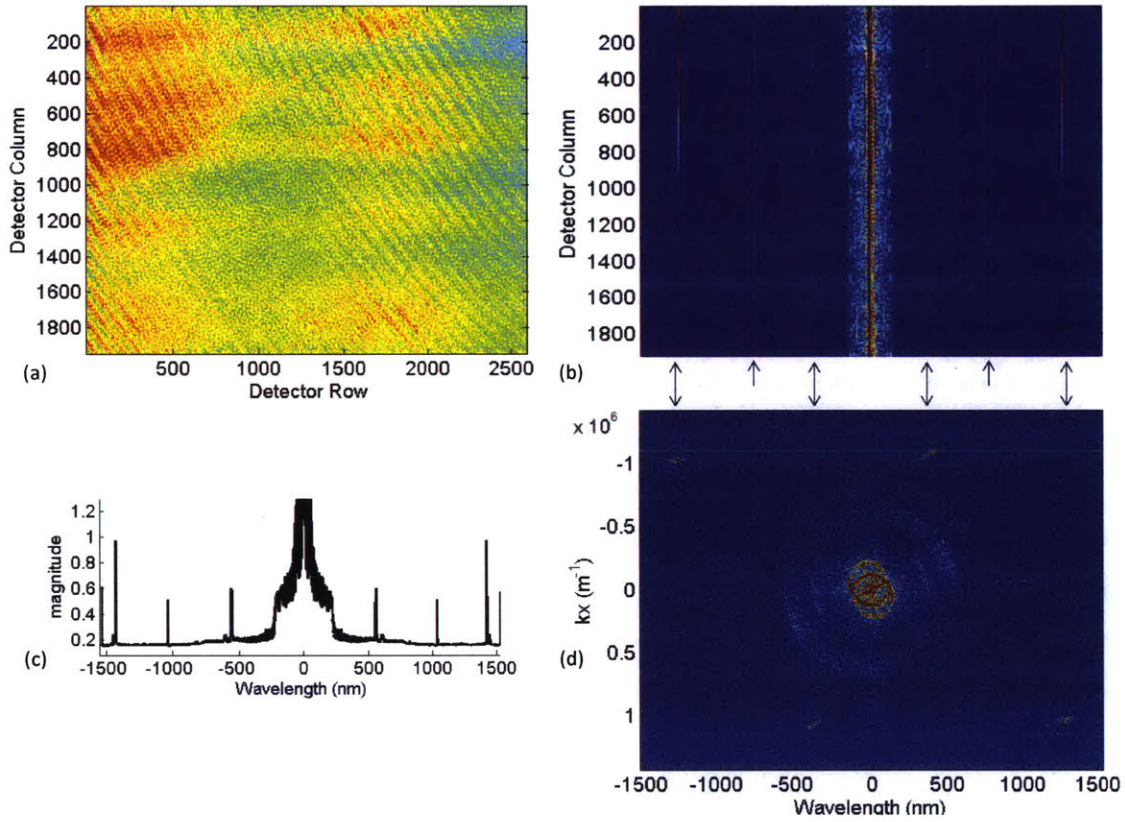

Figure 2.16: Data-Processing of Experimental Result
(a) Image from detector taken at 818.20 nm, 45 degree tilt. The triangle in the upper left hand corner is the region where all 3 diffraction orders exist. It is the region where the Talbot effect exists. (b) 1D-FFT taken along each column of the detector (row of the image). Note that the line corresponding to the wavelength (at about 1300 nm) only exists in the top half of the image, where the Talbot self-images exist. (c) Mean of the 1D-FFT data across all the columns of the detector (d) 2D-FFT of the image revealing an asymmetry in the frequency domain. Peak features in 2D-FFT image map onto 1D-FFT image.

We also observe that for each measurement, we have two significant peaks in our spectrum correlated to wavelength, even though we only expect a single frequency component. In Figure 2.16, we see that these two

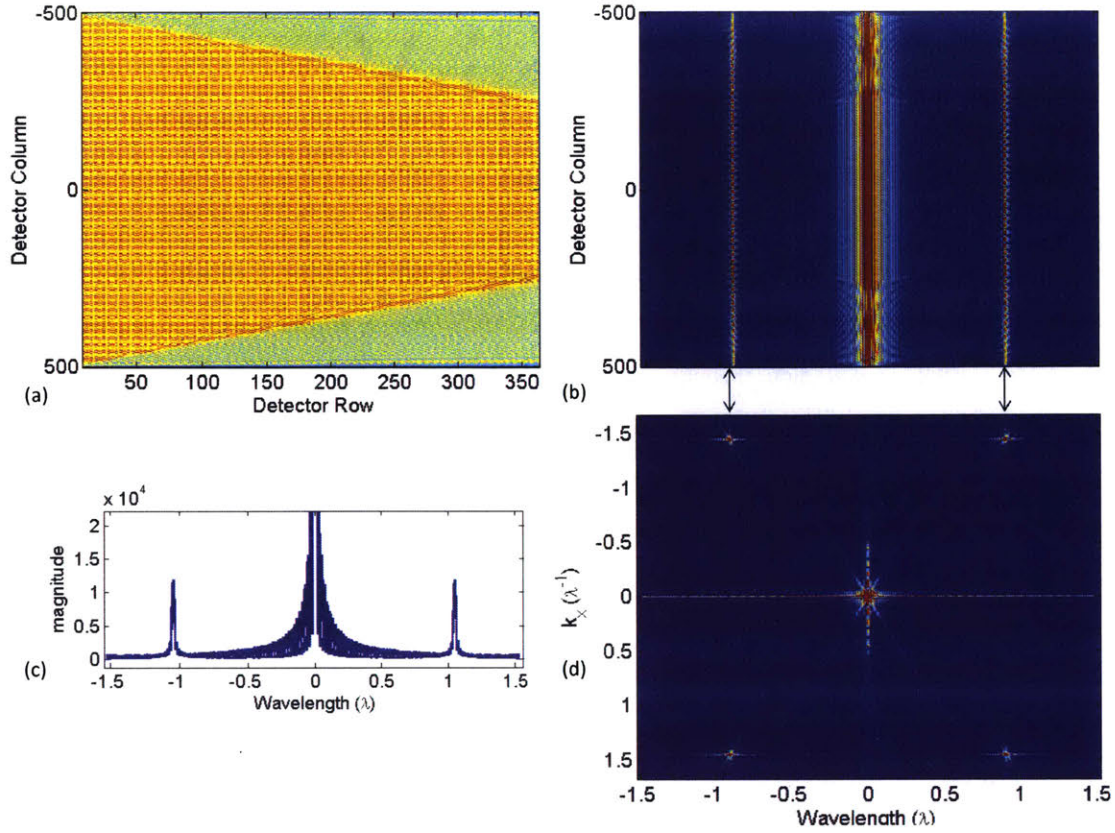

Figure 2.17: Data-Processing of Simulated Result
(a) Expected detector response given a normalized wavelength $\lambda = 1$, and 45 degree tilt. The triangle in the upper left hand corner is the region where all 3 diffraction orders exist. In this region the Talbot effect exists. (b) 1D-FFT taken along each column of the detector (row of the image). Note that the line corresponding to the wavelength (at about $\lambda = 1.05$) only exists in the top half of the image, where we expected the Talbot self-images to exist. (c) Mean of the 1D-FFT data across all the columns of the detector (d) 2D-FFT of the image. Peak features in 2D-FFT image map onto 1D-FFT image.

peaks correspond to an asymmetry in the 2D FFT. Comparing the 2D FFT image (d) to the 1D FFT image (b), we see that the peaks actually line up. The horizontally shifted peaks in the top half of the image line up with the 1st and the 4th non-DC peaks in the 1D FFT. The peaks in the bottom half correspond to the 3rd and 6th non-DC peaks. This suggests that we see multiple peaks in the 1D FFT because the image and the detector are not perfectly aligned. We also note that if the 2D FFT was symmetric, the calculated wavelength would be more accurate. For comparison, Figure 2.17 shows what our model predicts the collected data to look like. There is no asymmetry in the 2D FFT, so there is something in our experiments that our model does not account for. We also notice that in the simulated calculations, the measured wavelength is actually $\lambda = 1.05$, even though the input was $\lambda = 1$. At 830 nm, this would correspond to a redshift of about 40 nm.

As we will see later, the 2nd and 5th peaks in the 1D FFT image are frequency components that are inherent to the image. The peak location is not sensitive to wavelength, but is sensitive to the detector angle. It turns out the peak corresponds to a period equal to four times the effective pixel length, so it most likely is a feature of the detector itself.

When tuning the laser source, we see the peaks tune accordingly. We are to resolve different peaks from about 780 nm to 900 nm, as shown in Figure 2.18. The bandwidth can be greater, but ultimately is limited at longer wavelengths due to the limited sensitivity of the CMOS imager, and limited at lower wavelengths due to the unoptimized transmission through the grating. Note that at about 1038 nm, there is a peak feature that stays constant regardless of wavelength. This is the peak we believe to be from the detector itself, since it is wavelength independent.

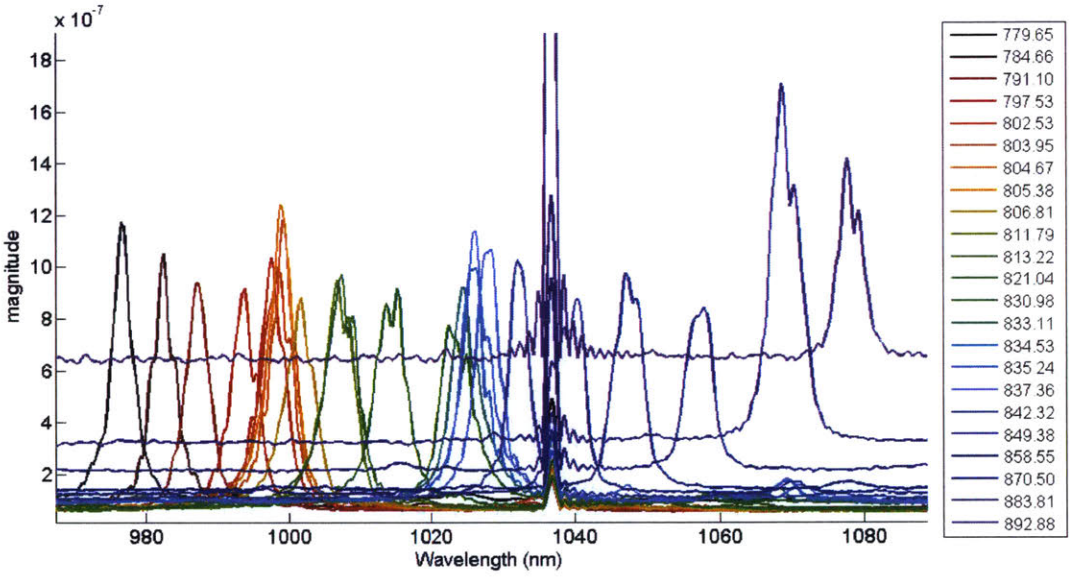

Figure 2.18: Talbot Spectrometer vs. Wavelength
Spectral response of Talbot spectrometer with the detector at 30 degrees (above) for input wavelengths from 780 nm to 905 nm. At approximately 1038 nm, we see the wavelength independent peak which likely is a feature inherent to the detector image.

Figure 2.19 shows the resolution limitations of the spectrometer response. When the detector is tilted at 30 degrees, the measured peaks have an average FWHM of about 4.58 nm, but wavelengths about 1.1 nm apart can be differentiated and likely could be resolved using deconvolution techniques. When the detector is tilted at 45 degrees, the peak widths are slightly decreased. The average FWHM is about 2.71 nm, and wavelengths about 0.8 nm apart can be differentiated. When peaks are not resolvable, the peak shapes are

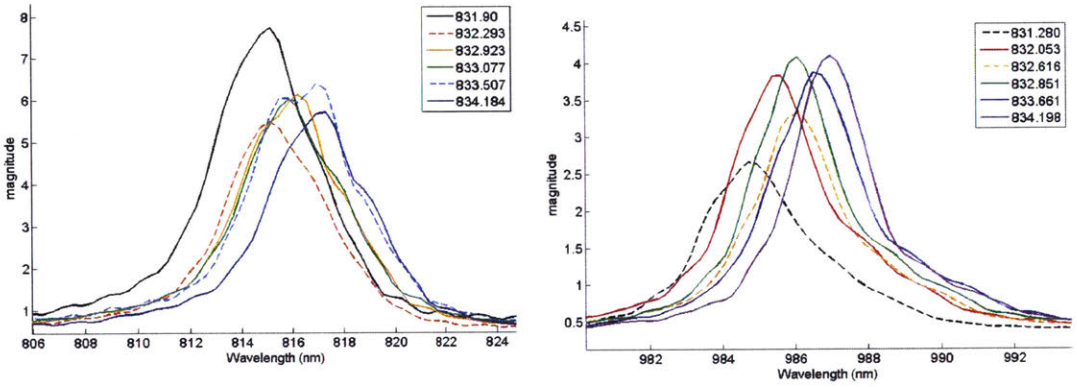

Figure 2.19: Talbot Spectrometer Resolution
Spectral response of Talbot spectrometer with the detector at (left) 30 degrees and (right) 45 degrees. The average FWHM of peaks in (left) is 4.58 nm. The minimum FWHM for is about 4.20 nm. The average FWHM for (right) is 2.71 nm, and the minimum FWHM is 2.38 nm.

not readily distinguishable from neighboring peaks, and tend to be broader since they overlap both of the peaks of the neighboring wavelengths.

The most obvious discrepancy is that the measured wavelengths are not accurate. In Figure 2.20, we see that the estimated wavelength has a reasonable slope (about 0.92), though is offset by 256 nm. We also see this offset change when adjusting the positioning of the detector. By looking at the experimental data presented in the section, we see the measured wavelength vary significantly even though all of the actual wavelengths are all between 780 to 900 nm. Therefore, this discrepancy most likely is because the detector is not perfectly aligned with the grating. This would cause the measured Talbot distance to be smaller than expected, resulting in a longer wavelength than expected. On the other hand, if the detector is not perfectly collimated, then one expects the Talbot distance to increase and the measured wavelength to decrease as we go farther away from the grating. This does not seem to be the main issue, since the wavelengths are significantly redder than expected.

Another concern is that the amplitudes of the peaks are not all the same, even though the pictures have been normalized by the power collected by the detector. The normalization power was found by multiplying the total intensity of the image by the detector's reported quantum efficiency at the wavelength of interest. The diffraction efficiencies (as reported in Figure 2.13) most likely contribute to the change in amplitude

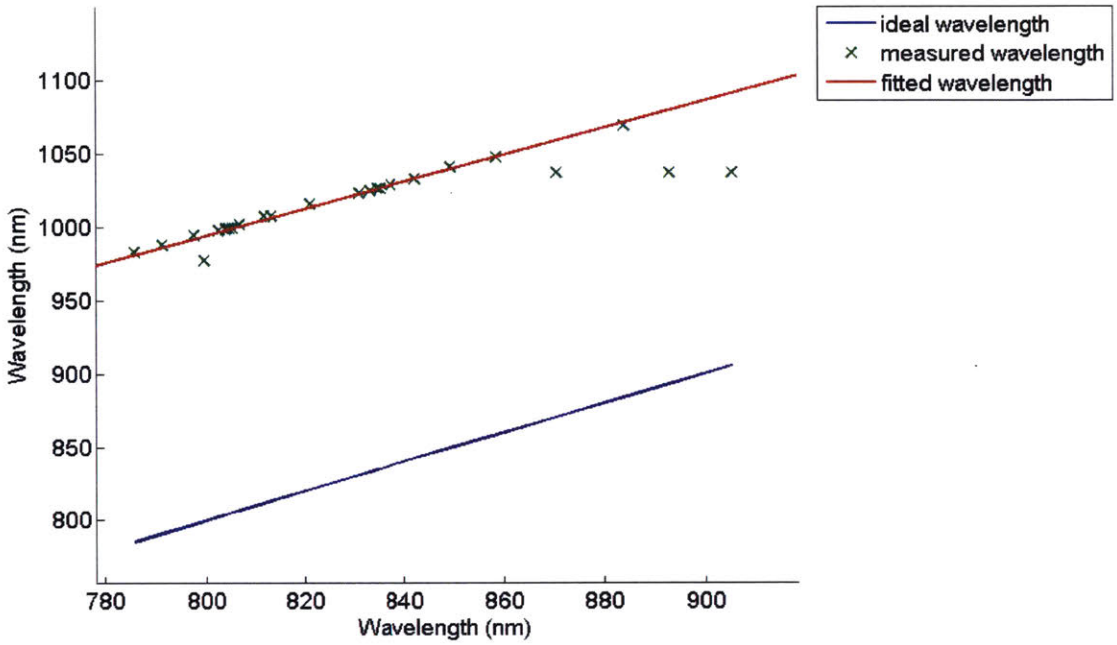

Figure 2.20: Talbot Spectrometer vs. Wavelength
Measured wavelength with respect to the actual wavelength. The wavelength was found by finding the maximum point in the high frequency region. The three outlier x's at the longer wavelengths correspond to the wavelength insensitive peak that is inherent in the detector.

over a wide range of wavelengths. However, in some cases, like in Figure 2.19, we notice that if the change in wavelength is too small, the measured peak position does not change, though the amplitude usually decreases.

Lastly, the observed peak width is not as good as was predicted theoretically. On the other hand, the minimum $\Delta\lambda$ that the spectrometer can differentiate matches the design curve well. This might mean that the incident wavefront is not a perfect plane wave. So, the peak width likely will be reduced when the optics are better aligned so that the beam incident on the spectrometer is well collimated. The Ti:Sapph beam also has a spectral bandwidth of about 0.2 nm, as measured by the HP Optical Spectrum Analyzer (HP70951B). The spectral non-zero bandwidth also will increase the observed peak width.

We were also able to clearly, simultaneously resolve lasers at two different wavelengths (see Figure 2.22). We managed to couple an Ondax laser operating at 829.95 nm and the Ti:Sapph beam to single-mode fibers, and used a 50/50 beam splitter so to combine the two. At the end of the fiber was a collimation lens, so most of the emitted light was incident on the beam expander. The expanded beam directly illuminated the grating and detector, which was roughly 2 inches away.

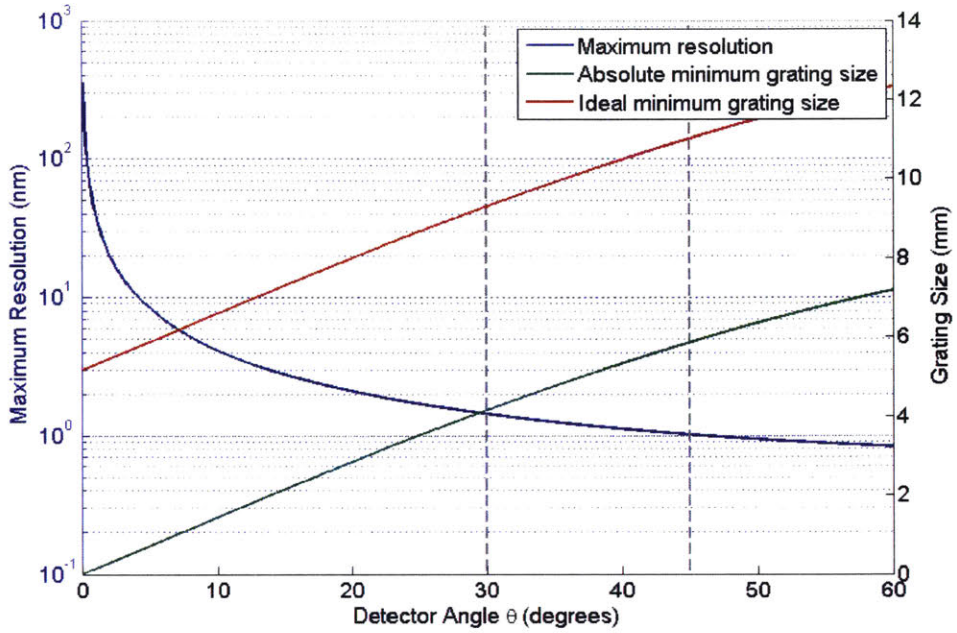

Figure 2.21: Resolution Limit for Current Spectrometer
Design curves for the experimental spectrometer. With a30 degree tilt, we expect a resolution about about 1.5 nm, and with a 45 degree tilt, we expect a resolution of slightly less than 1 nm. Notice that when at a 45 degree tilt, our grating size is smaller than the ideal grating size.

When we attempted to use a non-laser light source, no distinguishable signal could be obtained. This is somewhat unexpected because there are reports of the Talbot effect with white light sources [26]. We first tried using a neon calibration source. We spatially filtered the light through a 50 micron pin-hole or variable diameter iris, and then attempted to collimate the beam using a lens. The attempts at using neon calibration source were cursory, so the incident light was not properly collimated. However, it also might be the case that the peaks are too broad, so the periodic Talbot effect appears as white noise on the detector. This explanation does not make sense from the Fourier perspective and the superposition principle, which claims that as long as there is no aliasing, the detector should be able to successfully measure each frequency component that is present. However, in reality, the detector pixels are not simply delta functions. Instead, they report a single number which is the sum of the field at the detector. A better description of the pixels would be delta functions convolved with a rectangular function, though that still neglects the error that arises by summing over the field at each pixel.

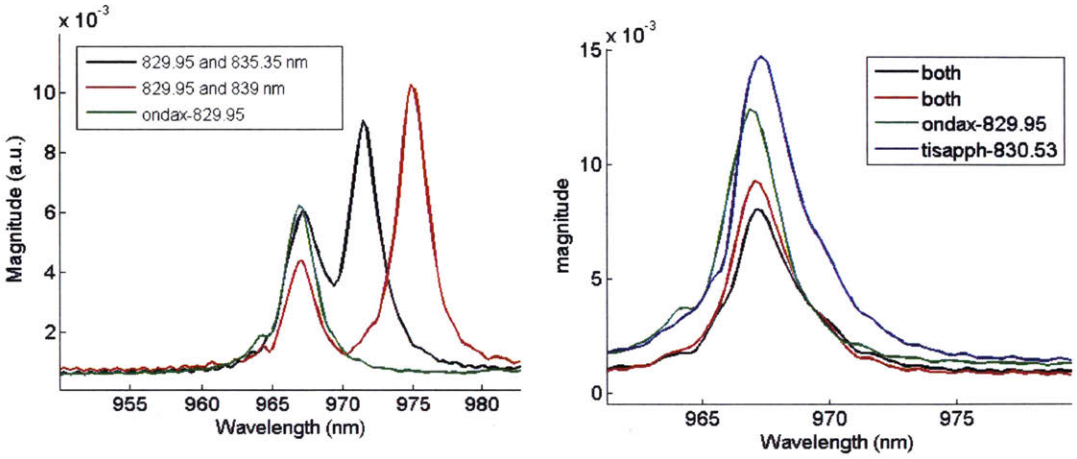

Figure 2.22: Talbot Spectrometer with Two Lasers
(left) The Ondax laser at 829.95 nm and a Ti:Sapph beam at two different frequencies (835.35 and 839 nm). Both peaks are clearly resolvable. (right) The Ondax laser at 829.95 nm and the Ti:Sapph beam at 830.53 nm. Though the two lasers can be differentiated separately, the spectrum when both lasers are on only has a single peak. Using FFT, these two peaks are not resolvable.

2.6 Summary

Plugging in our results into the table from the introduction, we see that, ignoring the size of the read-out electronics used for the testing phase, we have successfully engineered a miniature spectrometer with comparable resolution and etendue specifications. According to our theoretical design curves, we should be able to build a spectrometer with even higher resolution by changing the pixel pitch and grating periodicity.

For the most part, our simple theoretical model was able to correctly predict the experimental results of the system. However, our model was unable to account for the unexpectedly large peak width, and also was unable to explain the offset of the measured wavelength and why there are two peaks in the FFT spectrum instead of just one. One contribution to the large peak width is the non-zero linewidth of the laser. For a linear system, the detected linewidth should be a convolution of the expected resolution and the linewidth of the light source. However, the peak width is still significantly wider. The offset in the measured wavelength an the presence of the two peaks might be because of extra degrees of freedom in the experimental set-up, allowing the detector to be rotated around multiple axes. However, it could also be crosstalk caused by the

Table 2.1: Miniature Spectrometers

This table lists recent miniature spectrometers that have appeared in the literature, as well as our experimentally-verified Talbot spectrometer and the theoretical high resolution version. The estimates of the spectrometer size included the space in between the grating and the detector. Etendue is calculated from $\pi(\mathrm{NA})^2 A_{slit}$.

Author	**Spectrometer Type**	**Resolution**	**Etendue (mm^2)**	**Size (mm x mm x mm)**
Kung 2001 [38]	Talbot	42 nm	0.003	40+ x 4.9 x 6.5
Xu 2003 [92]	Disordered 3D PhC	2-20 nm estimate	0.024	30+ x 5 x 5
Redding 2013 [67]	Disordered 2D PhC	0.75 nm	1e-7	0.100 x 0.050 on chip
Park 2008 [58]	Fresnel	10-23 nm	8.2e-4	1-7 x 0.750 x 0.750
Momeni 2009 [48]	Waveguide	0.010 nm	1e-7	0.080 x 0.200 on chip
Wang 2014 [87]	Broadband Diffractive Optic	1 nm	0.077	500 x 9 x 9
This work (exp.)	Talbot	4 nm	0.033	5 x 10 x 10
This work (theor.)	Talbot	0.5nm	0.033	3 x 10 x 10

microlens array, or a result of the reflections off the glass cover slide. To understand this observation, we could expand our simulation so we can determine the detector response when it is tilted at any arbitrary angle with respect to the grating. On the experiment side, we can attempt to remove the glass cover and microlens array to ensure that they are not generating extra artifacts.

Additionally, though two independent lasers were detected simultaneously, it would be better if the spectrum of a multi-line non-laser light source could be measured.

Chapter 3

Photonic Crystal Resonant Scatterers

In this Chapter, we will discuss the second of three applications, the resonant scatterer barcode. We investigate the possibility of using a silicon/silicon dioxide 2D photonic crystal (PhC) resonant cavity for this application.

In order to be useful as a barcode, the scatterer needs to have at least 10000 optically differentiable variants within a 100 nm spectral range. Furthermore, to be useful in a biological setting, the scatterer cannot interfere with cell function, and must be on the order of a few micrometers. At first glance, silicon PhCs are a sensible solution. Photonic crystal resonant modes can have spectral line-widths that are less than a nanometer, while the mode is confined to volumes on the order of a few microns. So, a PhC cavity could potentially be very small. Furthermore, silicon dioxide is a non-toxic material, so it would be suitable for biological applications.

In the following sections, we first will review the theory on optical back-scattering from a resonant cavity, and then discuss simulation results of a first iteration design. Finally, we will compare the theoretical simulations with experimental observation from the first iteration of devices.

3.1 Photonic Crystal Resonant Cavities

In order to design resonant cavities for this application, we need to understand the main loss mechanisms and be able to engineer them to achieve high Q radiative emission.

The possible losses in an isolated 2D PhC resonant cavity are material absorption losses, losses from the cavity into the rest of the 2D plane, radiative losses into free space. Material absorption loss is simply

the loss due to the absorption of energy by the cavity material. For now, we will assume the absorption loss is negligible compared to the other loss mechanisms. In reality, the measured loss in these cavities are approximately 30 dB/cm at 1300 nm, which actually is quite high, and will limit the maximum achievable Q of a resonant cavity. In the future, this loss should be more carefully considered but our experiments show that absorption is not the dominant loss mechanism. The experimental results from Chapter 4 also support this approximation. The in-plane loss is from the fields that are no longer confined by the PhC cavity. The loss describes how well the resonant mode is confined to the cavity. For PhC cavities, this loss is decreased for an increased number of mirror holes surrounding the cavity. (For reference, a picture of a 2D PhC resonant cavity is shown in Figure 3.1.) This makes sense intuitively because the periodic boundary conditions that generate the PhC's optical band gap assume an infinite number of periodic elements. A photonic crystal with a reduced number of periods would have higher transmission for frequencies in the band gap. The radiative loss is from the fields that are scattered out of the cavity and out of the chip.

The radiative loss mechanism is what we will utilize in order to couple a free space beam into the cavity and detect a back-scattered signal. By fine tuning the defect cavity structure, the radiative emission of the cavity can be engineered further. We will use simulation software to predict the resonant modes of the cavity and their far-field radiation pattern.

3.1.1 Back-Scattering Coupled-Mode Theory

To understand how these losses play a role in the the back-scattered signal from a PhC cavity, we use temporal coupled-mode theory, which was introduced in Section 1.5.1.

The electromagnetic energy stored in the cavity, $\int \varepsilon|E|^2/2 + \mu_0|H|^2/2dV$, is defined to be $|A|^2$. If the cavity is perfect so that the energy remains completely confined in the cavity, $A(t) = A(0)e^{(-i\omega_0 t)}$. However, the cavity always has loss, and A and is assumed to decay with a lifetime of τ_{tot}. The lifetime is determined by the radiative coupling out of the resonant cavity mode (τ_{rad}), as well as loss of energy through absorption or other means (τ_{loss}), and can be expressed as $\tau_{tot}^{-1} = \tau_{rad}^{-1} + \tau_{loss}^{-1}$. Energy also can be coupled into the cavity. Here, we consider an incoming wave with amplitude S_+ that couples into the cavity at a rate given by τ_{in}^{-1}. In this case, since the incident wave is coupled into the cavity from free space, and the radiated wave is coupled into free space from the cavity, $\tau_{in} = \tau_{rad}$. As a result, the rate equation for A is

$$\frac{dA}{dt} = -i\omega A = -i\omega_0 A - \frac{A}{\tau_{tot}} + \sqrt{\frac{1}{\tau_{rad}}}S_+ \tag{3.1}$$

The electric field leaving the cavity has an amplitude S_- and can be found from

$$S_- = -S_+ + \sqrt{\frac{1}{\tau_{rad}}}A \tag{3.2}$$

The incident field of frequency ω drives the time dependent oscillation of A, such that $A(t) = e^{-i\omega t}$, since frequency is conserved for linear systems. The intensity of the reflected wave is

$$\frac{|S_-|^2}{|S_+|^2} = \left| \frac{(i(\omega - \omega_0) + (\frac{1}{\tau_{rad}} - \frac{1}{\tau_{tot}}))}{(i(\omega - \omega_0) - \frac{1}{\tau_{tot}})} \right|^2 = \frac{((\omega - \omega_0)^2 + (\frac{1}{\tau_{rad}} - \frac{1}{\tau_{tot}})^2)}{((\omega - \omega_0)^2 - \frac{1}{\tau_{tot}})} \tag{3.3}$$

If we are able to isolate the back-scattered signal radiating from the cavity from the specular reflections from the incident wave, then S^- becomes $S^- = \sqrt{\frac{1}{\tau_{rad}}}A$, and the intensity of the reflected wave is

$$\frac{|S_-|^2}{|S_+|^2} = \left| \frac{\sqrt{\frac{1}{\tau_{rad}}}}{(i(\omega - \omega_0) - \frac{1}{\tau_{tot}})/(\sqrt{\frac{1}{\tau_{rad}}})} \right|^2 = \frac{\frac{1}{\tau_{rad}^2}}{((\omega - \omega_0)^2 - \frac{1}{\tau_{tot}^2})} \tag{3.4}$$

Note that if the radiative lifetime is much longer than the lifetime of other loss mechanisms ($\tau_{rad} \gg \tau_{loss}$), then the intensity of the back-scattered light will be 0 regardless of wavelength. On the other hand, if the radiative lifetime is significantly shorter ($\tau_{rad} \ll \tau_{loss}$), then $\tau_{tot} \approx \tau_{rad}$, and the reflected intensity is 1 when on resonance and approaches 0 farther away from resonance. This is the ideal case for the back-scattering measurements. But, in order for the resonant cavity to have a narrow spectral line-width, the cavity needs to be low loss.

Therefore, there are two challenges that need to be overcome for this application. The first is to control the radiative quality factor to balance between having a high quality factor cavity and getting detectable back-scattered signal, and the second is to decrease the in-plane loss while miniaturizing the resonant cavity.

3.1.2 Resonant Cavity Simulation

The cavity design was based on the cavity in Haddidi's paper [27]. As discussed in the introduction, by changing the size and shifting of the lattice holes at the edge of the resonant cavity, the far-field pattern can be engineered to maximize vertical emission. Specifically, according to Tran et al., by modulating the hole sizes to create a $2a$ periodic structure, fields that were originally trapped beneath the light line can be "folded" above the light line, thereby increasing the intensity of the far-field radiation [82].

A picture of the 2D cavity is shown in Figure 3.1. We define $r_{lattice}$ to be the radii of the unmodified holes in the lattice and a to be the lattice constant of the hexagonal 2D PhC. The radii of the band-folding

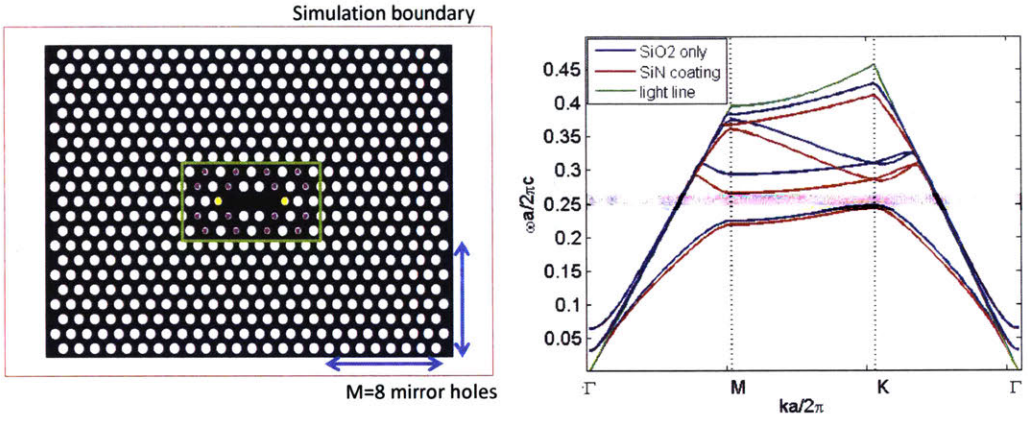

Figure 3.1: Resonant Cavity Design
(a) A 2D slice of the resonant cavity as simulated in MEEP. The red box shows the simulation boundary and the green box marks the defect cavity. The holes filled with purple are responsible for the band-folding effect and have radius $r_{fold} = 0.28a$. The holes filled with yellow are the cavity-edge holes. They are shifted outward by $\Delta x_{edge} = 0.16a$ and have a radius of $r_{edge} = 0.24a$. Here, $r_{cavity} = 0$. (b) The optical band structure of the 2D hexagonal photonic crystal with and without a SiN cladding layer. The region in pink shows the frequencies for which there is an incomplete band gap for the crystal with a 70 nm cladding layer.

holes, marked in purple, are $r_{fold} = r_{lattice} - \Delta r_{fold}$. The radii of the cavity-edge holes, marked in yellow, are $r_{edge} = r_{lattice} - \Delta r_{edge}$, and are shifted outwards by Δx_{edge}. The holes in the cavity can be reinserted, and their radii is r_{cavity}. There are M_x and M_y mirror holes in the x and y directions of the cavity.

The default structure for the simulations and measurements are $r_{lattice} = 0.30a$, $\Delta r_{fold} = 0.02a$, $\Delta r_{edge} = 0.06a$, $\Delta x_{edge} = 0.16a$, and $r_{cavity} = 0$. Unless otherwise specified, one can assume these parameters for the device. Typically, $M_x = M_y$ and is simply referred to as M.

The band structure of a hexagonal lattice of SiO_2 holes in a slab of silicon about 0.22 μm thick was simulated using MPB, a software program that uses fully vectorial eigenmode solutions of Maxwell's equations to determine the band structure of periodic dielectric structures [34]. This simulation confirmed that a hexagonal lattice of $r_{lattice}$ with oxide only would have a band gap from about 1413 nm to 1189 nm, if a was 0.350 nm. Most of the following simulations were done assuming the body was silicon and everything else was silicon dioxide. However, in practice, a conformal nitride layer is grown on top of the silicon to minimize material absorption loss. The red lines in the band diagram correspond to when a 70 nm nitride layer covers the silicon body. It shows that the band gap starts at a slightly redder wavelength, about 1436 nm, but ends at about 1313 nm.

Table 3.1: PhC Resonant Cavity Modes

This table lists resonant modes of the PhC cavity, their quality factors, and their out coupling efficiencies.

Resonant Mode	**Frequency** ($\omega a/2\pi c$)	**Quality Factor**	**Coupling Efficiency (NA = 1)**	**Coupling Efficiency (NA = 0.5)**
Y3	0.25016	3549.5	1.217e-4	4.317e-5
X2	0.26684	234.41	0.3069	0.1365
X1	0.26980	189.95	0.1178	0.0489
Y5 [a]	0.28235	1219.7	0.0125	0.0025

[a] This mode is not well confined when the silicon is lined with SiN.

Because the nitride layer is thin, and because the index of refraction is similar to the index of SiO_2, we expect that the simulated results with or without the nitride layer will give us comparable results, but with slightly different values. In particular, we expect that the simulated resonant modes will have slightly bluer wavelengths than what we observe in our experimental results. We can account for this difference simply by adjusting the lattice constant a or the thickness of the silicon in our simulations. We also neglect material absorption in the simulation.

Farfield Radiation Pattern and Band Folding

The near-field resonant field solution of the cavity was calculated using MEEP, a finite-difference time domain (FDTD) software [55], and the built in harminv resonant mode finder [43]. The far-field radiation pattern was found by taking the 2D Fourier transform, as elaborated in the paper by Kim et al. [37] and in the Appendix.

The resonant modes of the cavity and their farfield patterns are shown in Figure 3.2. The quality factors and resonant frequencies (normalized to lattice constant a) is listed in Table 3.1. The modes are labeled by the dominant polarization (X or Y) and the number of peaks along the x-axis.

To verify the band folding technique, we vary r_{fold} and observe how the farfield patterns of the Y3 mode are affected. As is noted by others [37], even though the near-field patterns do not appear to change significantly, the far-field patterns can vary significantly, as is shown in Figure 3.3. As discussed in Tran et al., changing band-folding holes can increase or decrease the band-folding effect. By changing Δr_{fold} from 0.02 to 0.10, the vertical emission from the Y3 mode is significantly increased.

These findings support the results presented in previous papers [82] [27], confirming the accuracy of our simulations. However, our simulations also revealed that there are highly emissive x-polarized modes that

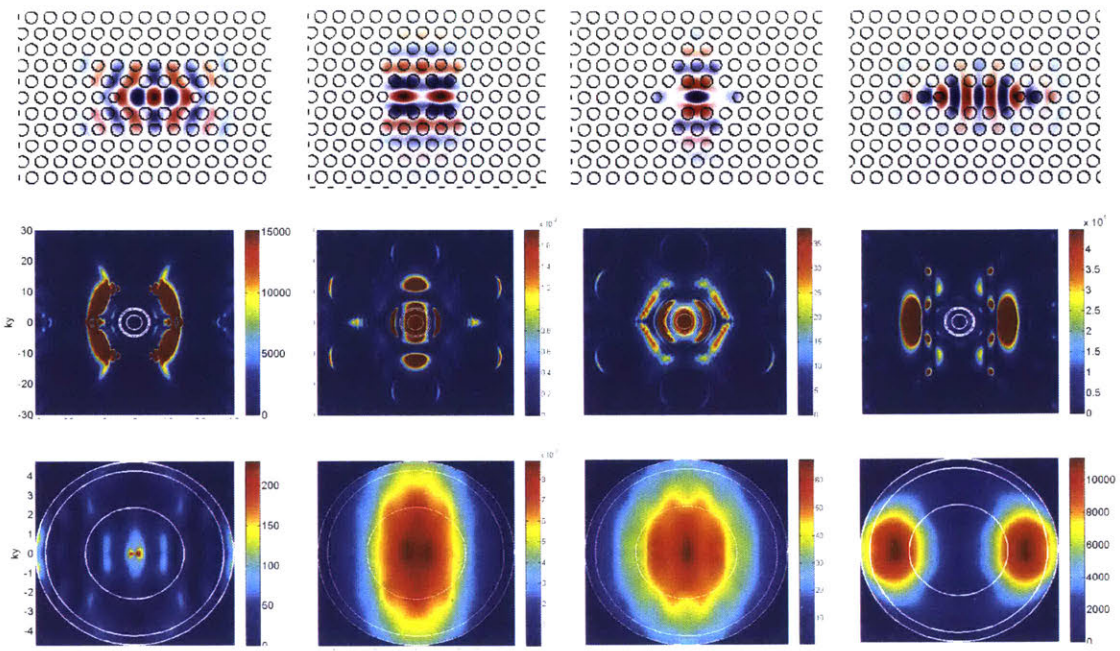

Figure 3.2: Resonant Modes of PhC Cavity
Resonant modes in the defect cavity (Top) Near-field resonant cavity fields as calculated by MEEP in increasing frequency. (Middle and Bottom) Far-field radiation patterns, found by taking the 2D FFT of the near-field pattern. The circles in white show the range of light that is collected for objectives with numerical apertures of 0.5, 0.9, and 1. Here, Δr_{fold} is 0.02a. These modes (left to right) will be referred to as Y3, X2, X1, and Y5, respectively.

Table 3.2: Band-Folding for Y3 Modes

Resonant frequency, quality factor, and out-coupling efficiency of the Y3 mode for different Δr_{fold}.

Δr_{fold} (a)	**Frequency** $(\omega a/2\pi c)$	**Quality Factor**	**Coupling Efficiency (NA = 1)**	**Coupling Efficiency (NA = 0.5)**
0	0.25147	4015.5	1.645e-5	2.667e-6
0.02	0.25016	3549.5	1.217e-4	4.317e-5
0.06	0.24789	1829.4	5.956e-4	3.739e-4
0.10	0.24594	1219.7	0.0449	0.0310

the previous papers did not report. Without modification of the cavity structure, these modes have vertical emission patterns, which provides a strong signal for back-scattering. Unfortunately, because the radiative losses are so high, the quality factor of those modes are too low.

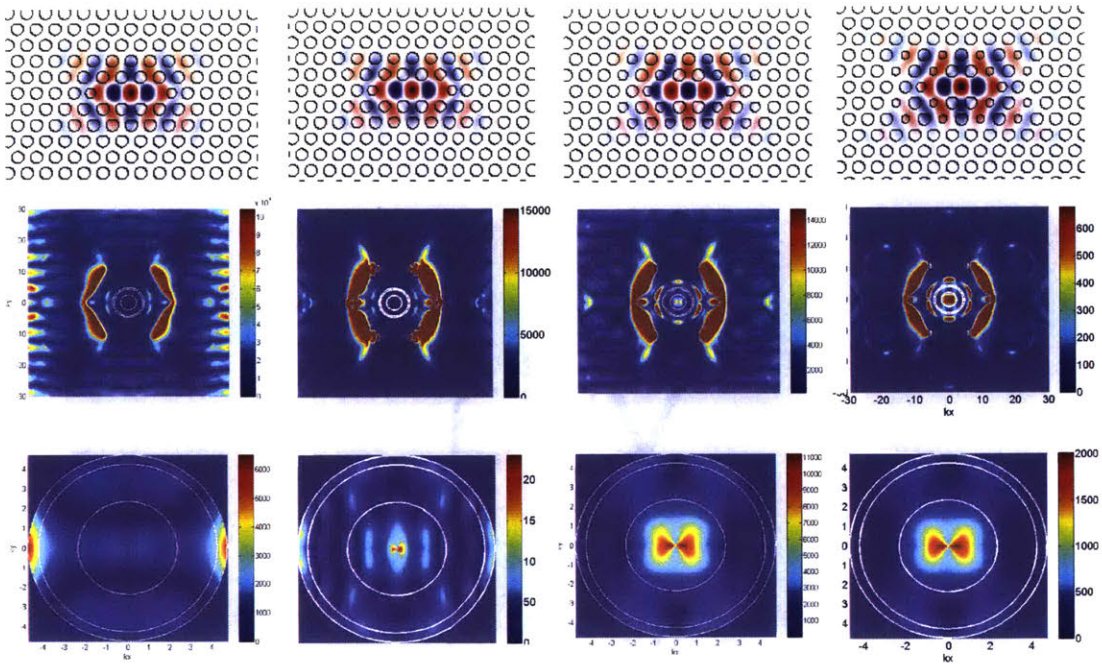

Figure 3.3: Effect of "Band Folding"
These simulations show how the farfield radiation pattern changes with variations of the radius r_{fold} in the resonant cavity. Δr_{fold} = 0, 0.02, 0.06, 0.10 from left to right.

Simulations of Size Dependence

One important factor for us that has not been mentioned explicitly in the previous work is the total size of the cavity. For the current device design, a device with M mirror holes is approximately $(2M + 10)a$ by $(2M + 5)a$ in size. Therefore, a device with 8 mirror holes is approximately 9.1 μm by 7.35 μm. A device with 16 mirror holes is approximately 14.7 μm by 12.95 μm. Because of the size constraints for our applications, we need to limit the number of mirror holes M, increasing the in-plane loss of the defect cavity.

In 3D numerical simulations, when the absorptive losses are set to zero, the main loss mechanisms are radiative losses and in-plane losses. In a 2D simulation, since no energy can be radiated out-of-plane, the radiative losses are also zero. Therefore, the reported quality factor from a 2D simulation is the quality factor for lateral confinement (Q_{lat}).

As expected, the quality factor of the cavity in our 2D simulation increases with the number of mirror holes surrounding the cavity. Notice that Q_{lat} is at least a few magnitudes larger than Q found from the 3D simulations as presented above in Table 3.1. This tells us that for our cavity design, radiative loss is the

Table 3.3: In-Plane Quality Factor vs Number of Mirror Holes

This table lists the simulated Q of the resonant modes as a function of the number of mirror holes.

Mode	M=0	M=8	M=12	M=16
Y3	N/A	66540.2	775788.9	951370.1
X2	N/A	8500.8	71244.5	158827.7
X1	N/A	7571.1	14303.2	15692.0

dominant loss mechanism. Because of this, the effect the number of mirror holes has on the quality factor will be negligible.

Also note that in order to have a $Q_{tot} \approx Q_{rad}$ at about 10^5, Q_{lat} needs to be orders of magnitude larger. For the current cavity design, Q_{lat} for the X1 mode is noticeably low, and is not greater than 10^5 even with 16 mirror holes. Therefore, in addition to increasing the quality factor of the radiative losses, we will need to find a way to miniaturize the system further while increasing the lateral confinement of the mode.

3.2 Measurements

To verify our numerical simulations, we measure the back-scattering from devices with different variations of the defect cavity. The devices were fabricated by CNSE using a 65 nm bulk CMOS process. These devices are patterned in polysilicon that is about 0.220 μm thick, and remained embedded in the chip for these measurements. The lattice constant of the photonic crystals was 350 nm. Again, unless otherwise stated, the default structure for the measured devices are $r_{lattice} = 0.30a$, $\Delta r_{fold} = 0.02a$, $\Delta r_{edge} = 0.06a$, $\Delta x_{edge} = 0.16a$, and $r_{cavity} = 0$.

3.2.1 Experimental Set-up

The experimental set-up was based off of the method used by Deotare [12], and is shown in Figure 3.4. A tunable laser source (Santec TSL-210F) was used to provide 100 μW of power from 1260 nm to 1620 nm. A polarizing beam splitter (PBS) (Thorlabs PBS254) was used to polarize the incoming light. The s-polarized light is reflected down through a microscope objective (Mitutoyo M Plan NIR 100, NA=0.50, f=200). If the light is at the correct frequency, then one of the resonant modes of the cavities is excited and some radiated light is recollected by the objective. The p-polarized light radiated from the PhC cavity will be transmitted through the PBS to the IR Camera (Xenics Xeva-1785). An integration time of 25 ms is used to capture each frame. This integration time was chosen to avoid saturation of any of the pixels while still getting

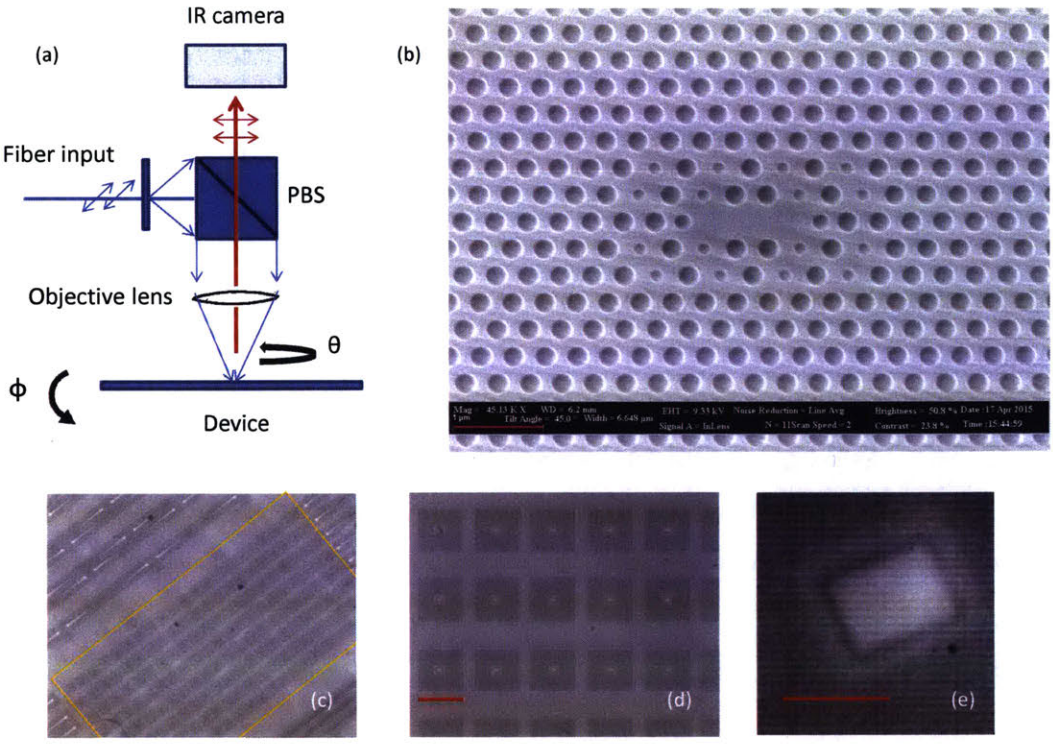

Figure 3.4: Experimental Set-up
(a) The optical set-up of a slightly modified optical microscope with an NIR camera on top. A polarizing beam splitter (PBS) is used to polarize the incident beam and also to filter out the specular reflections that are not back-scattered reflections from the photonic crystal. (b) SEM image of sample photonic crystal device. As is done in Haddidi and Tran, holes every 2a are modified in size to create the "band-folding" technique. The holes at the edge of the cavity are slightly smaller and slightly shifted outward to increase the quality factor Q. The scale bar in red is 1 micron. (c-e) are images taken with a 5x, 20x, and 100x microscope objective. The scale bar in (d) is approximately 35 microns and the scale bar in (e) is approximately 12 microns.

appreciable signal.

The polarization of the radiated field is determined by the resonant mode of the cavity, whereas the polarization of the specular reflection largely remains the same as the polarization of the incident beam. Therefore, if the cavity is rotated by an angle θ with respect to the axes of the polarizing beam splitter, the back-scattered beam will have both s-polarized and p-polarized light. Since only p-polarized light is transmitted through the PBS to the IR Camera, only that component of light will be observed.

Using the NIR camera, pictures of the resonant cavity and the back-scattered light at a various wavelengths are taken. The back-scattered signal at a given wavelength is calculated from

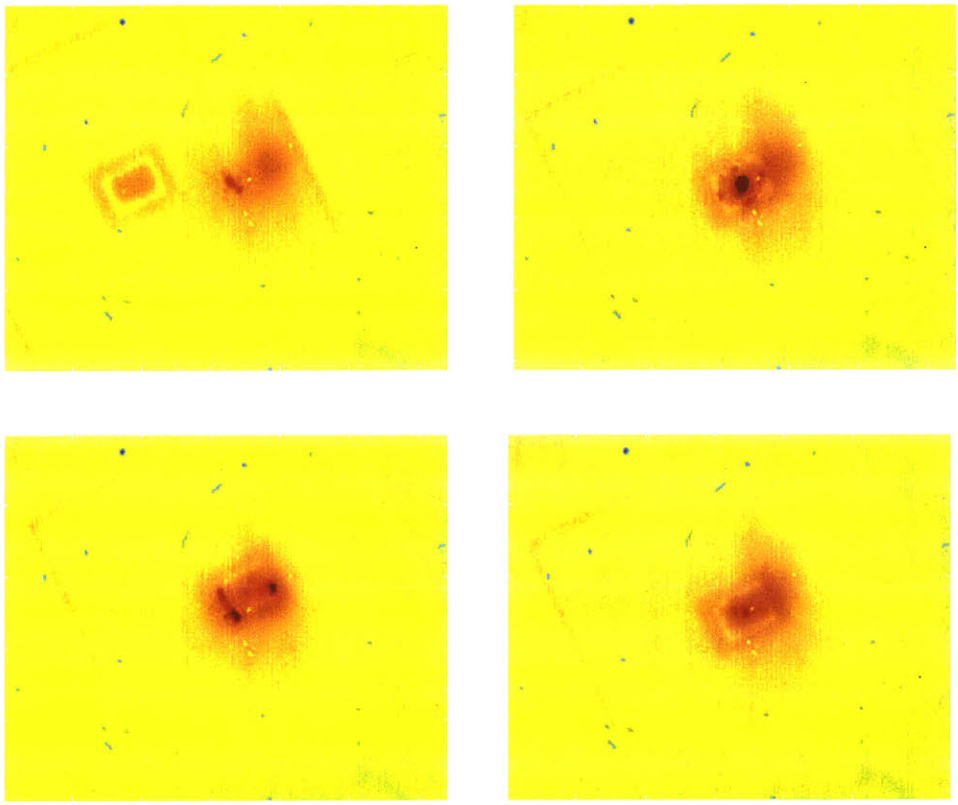

Figure 3.5: Images of Back-Scattering Devices
Images of back-scattering response when the excitation source (on resonance at 1296 nm) is focused outside the device, in the center of the device, on the edge of the device, and off centered but in the device (right to left, top to bottom).

$$\text{background} = \text{percentile(pixel values,0.98)}$$

$$\text{signal} = \sum \text{pixel values - background}$$

From the camera images, it is easy to see the observe the back-scattered light at the resonant frequency. As shown in Figure 3.5, when the cavity mode is on resonance and centered on or close to the resonant cavity, a strong signal from the center of the device is seen. When the excitation source is clearly not centered on the cavity, no back-scattered signal is observed.

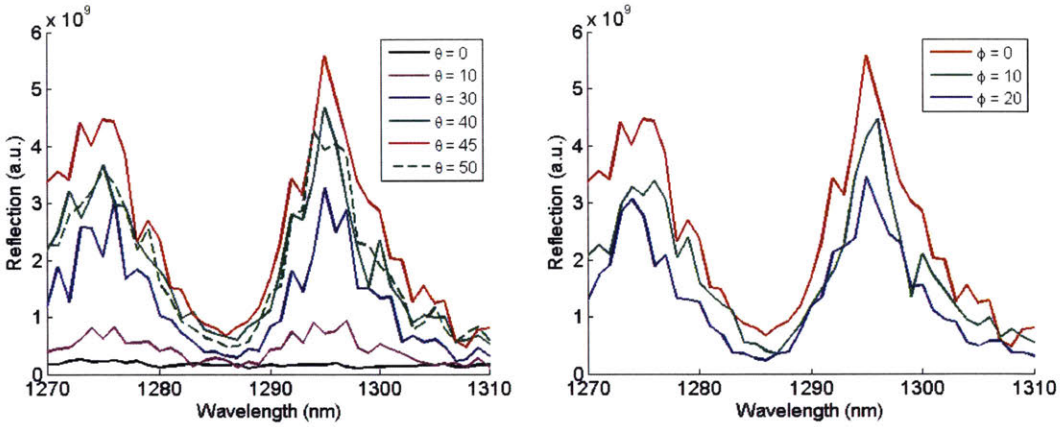

Figure 3.6: Spectra with Various Theta and Phi
Reflection spectra as the chip is rotated (a) in-plane by angle θ and (b) out-of-plane by angle ϕ.

3.2.2 Spectral Dependence on Orientation

Because the resonant mode is an in-plane resonance, we expect the signal to only vary in intensity and not in frequency as the orientation of the device changes. For different θ, we expect the detected signal intensity to be zero when $\theta = 0, 90, ...$ and to increase as we get closer to $\theta = 45$, because the signal is filtered by the PBS, which acts as cross polarizers.

By changing the out-of-plane rotation angle ϕ, we expect better or worse coupling to each mode, depending on the farfield radiation pattern. In the case of the dipole modes, we expect that reflection will decrease with increasing phi, since radiation from the cavity is mostly vertical. On the contrary, if the farfield pattern shows greater emission at certain angles, when the chip is tilted at that angle, the coupling efficiency should increase. Unfortunately, due to the size of the chip the PhC barcodes are on, and the short working distance of the microscope objective, it is difficult to increase the angle of incidence beyond the 20 degrees.

Our experimental results shown in Figure 3.6 clearly shows that the resonant frequencies stay constant with changes in θ and ϕ. Unlike Fabry-Perot devices, these photonic crystal resonator cavity devices can be identified by a given frequency of light under any orientation–only the efficiency of the back-scattering is affected. It may be possible to design a cavity such that the farfield pattern is relatively uniform for any given angle, but this comes at the cost of a reduced intensity of the back-scattering .

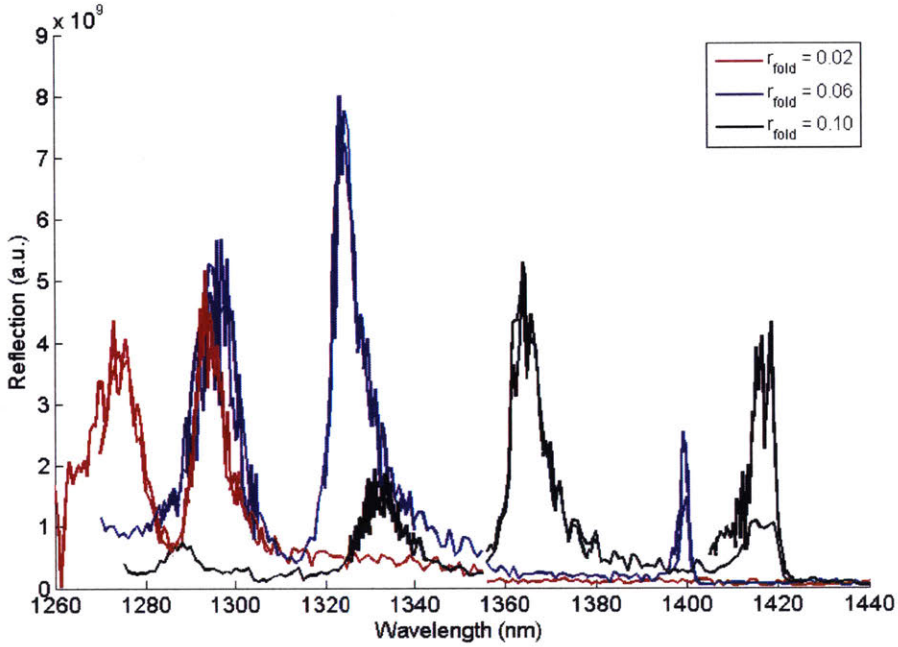

Figure 3.7: Back-Scattering Spectra for Cavity Variants
The reflection spectra measured for cavities with different Δr_{fold}. For increased Δr_{fold}, the Y3 mode was detectable, but also had broadened linewidths.

3.2.3 Effect of Band-Folding

When measuring devices with larger Δr_{fold}, the band-folding effect is more pronounced and the Y3 mode can be observed.

The anticipated collection efficiency for the Y3 mode in the cavity with $\Delta r_{fold} = 0.06a$ with a NA = 0.5 objective was 3.74e-4. The measured Q is approximately 728. In order to detect signal from even higher Q resonant modes, the sensitivity of the measurement set-up will have to be improved significantly. Increasing the NA of the objective might assist in collecting more signal, but also will collect more background light. As a result, with the current set-up and image processing method, the signal will be reduced.

This quality factor of the $\Delta r_{fold} = 0.06a$ and 0.10a Y3 resonant mode is noticeably lower than the simulated Q's of 1829.4 and 1219.7, respectively. This suggests that either the SiN cladding, which was not included in the simulation, reduces the quality factor of the resonant mode, or that the material absorption loss of the silicon is actually not negligible. The loss on the chip at 1300 nm was approximately 30 dB/cm for a wave propagating in a waveguide. If we assume that the modal overlap with the silicon body is roughly

80%, and the effective index is about 2.7, then we can approximate the energy decay rate at -30 dB per 10^{-10} seconds. The lifetime is defined as when the intensity in decays by $1/e$, which is about -4 dB. Therefore, if we assume the entire mode profile exists in the polysilicon, the lifetime is approximately 10^{-11}. This corresponds to a quality factor, which can be calculated from $Q = \omega_0 \tau/2$, is approximately 10^3. Therefore, the quality factor of the cavity actually is limited to about 1000.

3.2.4 Dependence on Number of Mirror Holes

We also observed the behavior of the barcodes with respect to the number of mirror holes. The cavity had default parameters ($r_{lattice} = 0.30a$, $\Delta r_{fold} = 0.02a$, $\Delta r_{edge} = 0.06a$, $\Delta x_{edge} = 0.16a$, and $r_{cavity} = 0$).

Aside from the cavity with no mirror holes, the peak width of the x-polarized modes X1 and X2 remain relatively constant for at least more than 8 mirror holes. This is because Q_{rad} is much less than Q_{lat}, so the radiative loss dominates the lifetime and peak width. This is true even for the Y3 modes, as the mode's Q does not increase with the number of mirror holes. For the device with zero mirror holes, we most likely are measuring a resonant mode of the silicon slab itself, hence the very broad spectral feature.

What remains unexplained is the clear dependence of the resonant frequency on the size of the cavity. Increasing the number of mirror holes by 4 shifts the resonant frequency by about 5 nm. This trend is unexplained by our simulations in MEEP, and suggests that our modeling of the confined resonant cavity is incomplete. The frequencies of the resonant modes as found in a 3D simulation of the defect cavity are listed in Table 3.4. Though some modes show a small change in resonant frequency as a function of size of the cavity, the shift is not 5 nm large. Because two physically different devices about 1400 μm apart, with the same barcode design, show the same reflection spectrum (Figure 3.10 (b)), it is unlikely that the shift in wavelength is due to fabrication uncertainty. Therefore, our understanding of these barcodes is still incomplete.

Table 3.4: Resonant Frequency vs Size

Frequencies of the simulated resonant modes as a function of the number of mirror holes. As expected, the frequencies do not change significantly with cavity size. Here we assume $a = 350$ nm.

Mode	M=0	M=8	M=12	M=16
Y3	1390.7	1387.8	1387.9	1387.9
X2	1311.2	1311.6	1311.8	-
X1	1293.4	1297.2	1298.7	-

In addition to the shift of the resonant frequency of the cavity, the amplitude and the line-shape of

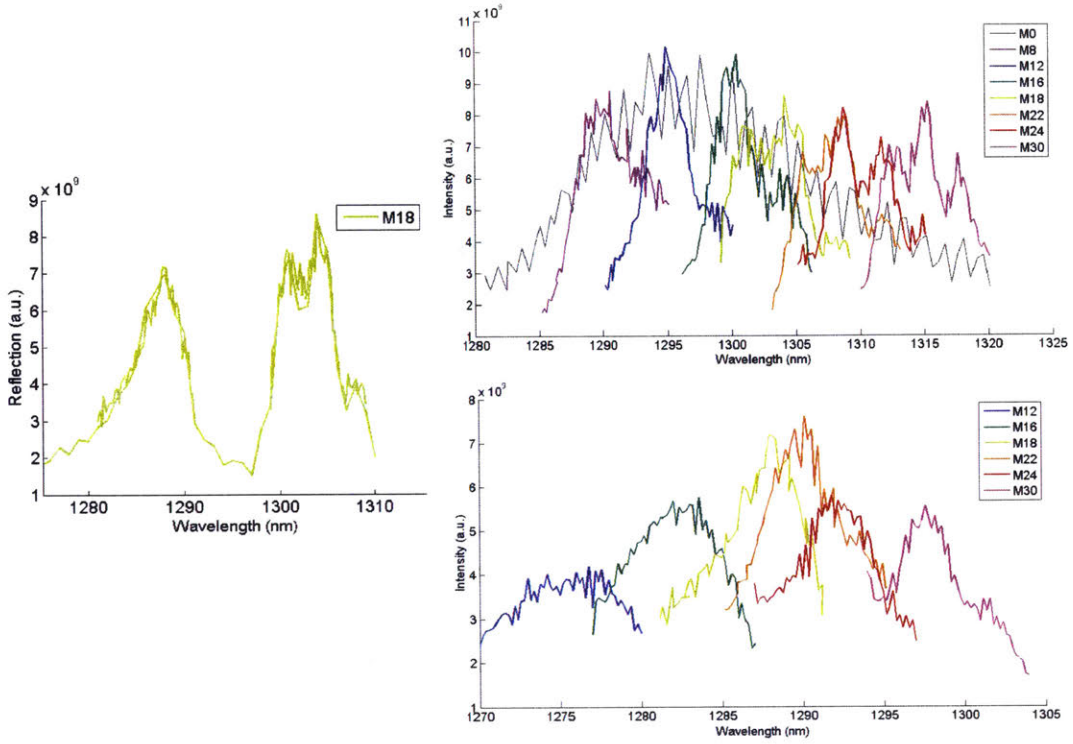

Figure 3.8: Effect of Cavity Size on X2, X1 modes
The reflection spectra of the X2 and X1 resonant modes are measured for cavities of different sizes. (a) shows the full spectrum for the M18 cavity, while (b) and (c) show the each peak as a function of cavity size. The peaks within each reflection peak may be in-plane resonance due to the small size of the entire device. The redder peaks correspond to the X2 mode.

the peaks were unusual. Instead of being constant, the amplitude of the resonant modes seemed to vary in a shape similar to the $M0$ resonant peak. This might provide some insight on how the photonic crystal resonant modes interact with the isolated silicon body. The line-shape of some of the resonant peaks also were non-Lorentzian and clearly showed fine-structure. These peaks might result from coupling of the resonant cavity mode to other resonant modes (like Fabry-Perot resonances) of the silicon body. Though it was not done here, it would be interesting to see how the fine structure changes with device tilt. If the fine structure is not sensitive to device orientation, then it would provide another method of encoding information for the barcode application.

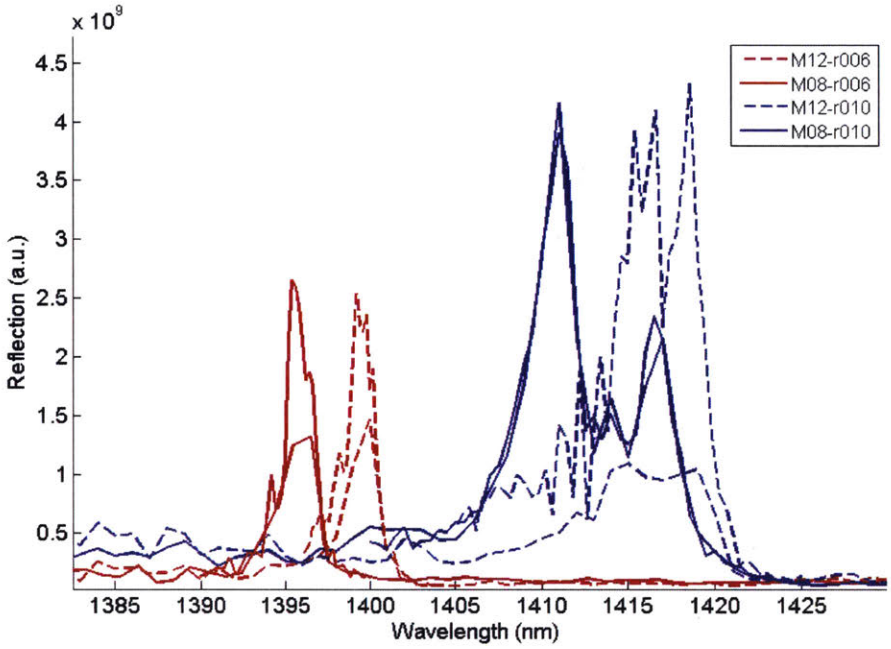

Figure 3.9: Effect of Cavity Size on Y3 Modes
The reflection spectra measured for cavities of different sizes. The approximate Q's for the $\Delta r_{fold} = 0.06a$ cavities are 852 and 702 for the M=8 and M=12 cavities respectively. The Q's for the $\Delta r_{fold} = 0.10a$ cavity cannot be estimated accurately because of the resonant mode's non-Lorenztian peak-shape. The FWHM linewidth is about 10 nm and 6 nm for the $M = 8$ and $M = 12$ resonant cavities.

3.2.5 Device Summary

In addition to the devices mentioned above, the chip contains other variants of the barcode device. The barcodes were predominantly free-space devices, as shown in Figure 3.1, with variations in the hole size or placement near the defect cavity. In addition to the devices with different r_{fold} and different M that are discussed above, barcode variants also have varied radii r_{edge} and positions Δx_{edge} of the holes at the edge of the resonant cavity. Some variants also have holes of $r_{cavity} = 0.2$ in the cavity center.

Variants with non-default values of r_{edge} and Δx_{edge} were not investigated because those parameters did not appear to significantly affect the resonant modes of the cavity. The observed resonant modes were actually the X2 and X1 modes, so it makes sense that the different variants, which were meant to improve the Q of the y-polarized modes, had similar reflection spectra. Therefore, these variants should be investigated further on devices where the Y3 mode is clearly visible.

There were also devices coupled to the straight and cosine waveguides to determine the coupling efficiency

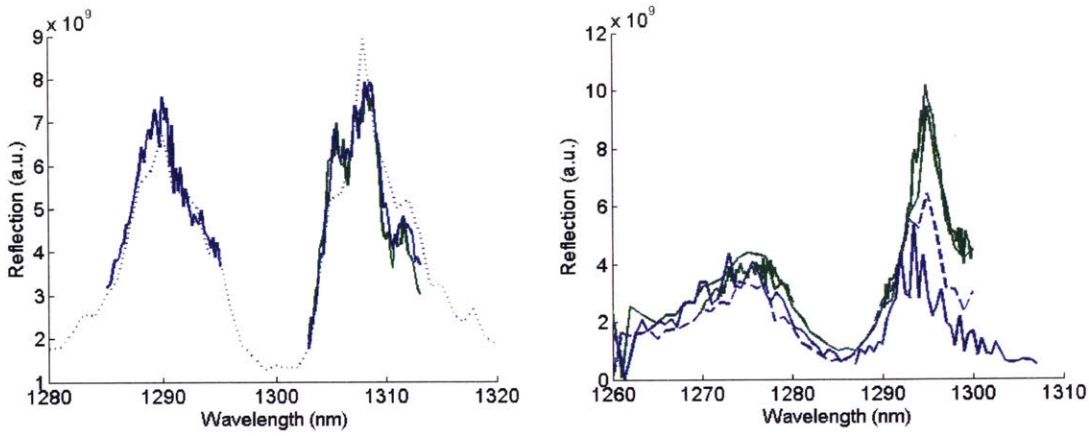

Figure 3.10: Reproducibility of Barcode Measurements
(a) Multiple measurements of the reflection spectrum of the M22 cavity. Note that the fine structure in the redder peak is reproducible. (b) The spectra of two physically different devices with the same cavity design (default parameters, $M = 12$). The devices are approximately 1400 μm apart. The spectra are overlaid to show how the spectra show the same resonant frequencies, though the measured signal amplitude is slightly different. The dashed lines show repeated measurements of the same cavity.

of the waveguide to the Y3 mode, depending on the number of mirror holes. However, the grating couplers were optimized for coupling at 1550 nm, so they were unable to be used to measure the resonances of the cavity.

Devices with $a = 330$ nm and $a = 350$ nm were fabricated, but the devices with lattice constant $a = 350$ nm were reported above. A map of the devices on the chip is in the Appendix.

3.3 Discussion

We successfully were able to measure frequency dependent back-scattering from photonic crystal resonant cavities that are roughly 10 microns by 10 microns in size. However, there are a few observations that were not expected from our simulations.

Most obvious is the correlation between the size of the cavity and its resonant frequency. The consistency of the resonant cavities across multiple iterations of the same device suggests that the dependence of resonant wavelength on device size is not just fabrication error. Because the resonant modes are low Q and therefore not well-confined to the defect cavity, the size of the chip may influence the resonant frequencies of the

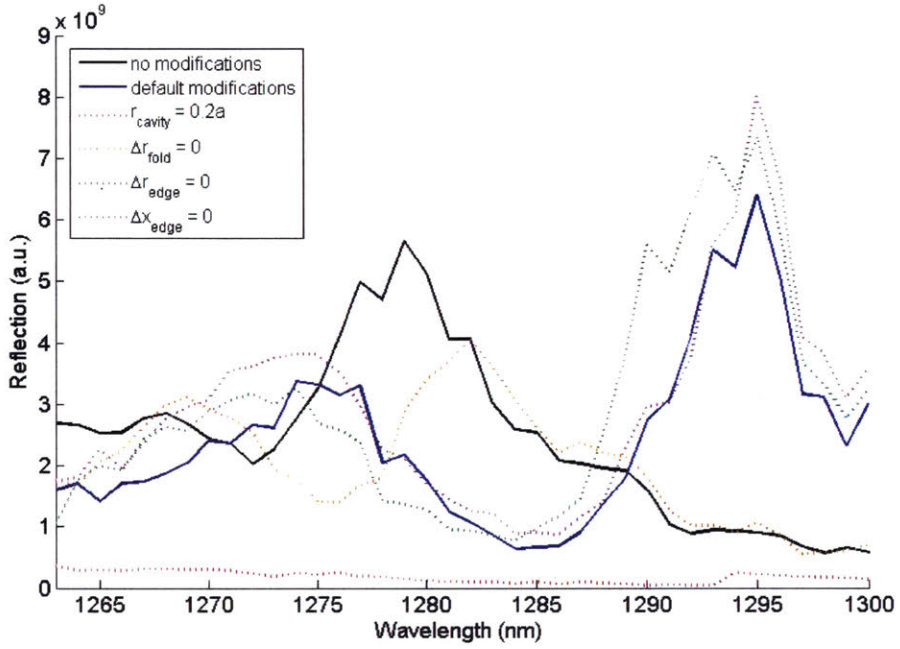

Figure 3.11: Effect of Different Modifications on X2 and X1 Modes
The reflection spectra measured for cavities with different r_{shift}, Δx, r_{cavity}, and r_{fold}.

cavity. However, our simulations suggest that the mode is relatively well-confined, and do not anticipate large changes in the resonant frequency with M. Experimentally, one could verify this effect by studying devices with different numbers of mirror holes in x but a constant number in y, and compare the shifts in resonance frequency for the x-polarized and y-polarized modes.

The second unpredicted observation is the intensity of each of the resonance peaks. Depending on M, the resonant peak height changes. The quantum efficiency of the detector remains approximately constant (within 10%) for wavelengths from 1 μm to 1.5 μm, so the change in intensity is related to the cavity. From the size series data in Figure 3.8, it seems like the back-scattering intensity is related to the resonant mode of the cavity with

Another observation is the presence of multiple peaks inside the supposedly Lorenztian peak of the resonant mode. This noise might be from other resonances of the non-radiated fields propagating in the device (like Fabry-Perot resonances). These extra peaks are probably more noticeable for low Q modes because of the breadth of the peak and also for the weaker confinement of the mode in the cavity. Some of the non-reproducible peaks might be noise, since for some of the measurements there were oscillations in the

measurement set-up that we were unable to dampen.

Our experimental results show that we are able to achieve spectral features with linewidths of less than 10 nm, for a device that is about 10μm by 10μm in size. Though the linewidths are about half of what is reported for quantum dots and similar barcodes, they are considerably bigger and would be more difficult to incorporate into a cell. Reducing the size of the barcodes while achieving Q's of 100000 seems impossible with the current approach. We may be able to increase Q to 10000 while maintaining the current size of the barcode, though the applications in cellular environments may be limited.

3.3.1 Next Iteration of Devices

Increasing Q to 10000 will still be difficult and will require optimization of the cavity design since, there are still limitations on the achievable Q_{rad} due to the thickness of the silicon in the device, and limitations on the achievable Q_{lat} because of the size of the device.

To reduce the line widths of the resonances, we most likely cannot solely rely on trying to reduce the losses of the device. Instead, we can also use interference. For example, it might be possible to use Fano resonances to reduce the line-width. In Haddidi et al., the observed Fano resonances were a result of the reflection of the incident light off of other layers of the device in addition to the back-scattered light. However, this might only work for normal incidence, since the reflection off the non-PhC layers will scatter away otherwise.

Alternatively, one could potentially interfere two resonant modes to increase the radiative Q [33] [86] [35]. This technique, which is called cancellation, will generate nodal planes in far-field radiation pattern [33], but that may be acceptable for our application if it decreases the linewidths of the cavity's resonance peaks.

Chapter 4

Silicon Photonic Crystal Modulators

4.1 Overview

In this Chapter we will present work on silicon resonant cavity modulators that have Fano line-shape transmission curves. These transmission curves have a very steep slope near the resonant wavelength. So, if a modulator were to operate near that wavelength, a slight change in the index of the material would result in a large change in the transmitted intensity. Therefore, utilizing a Fano transmission curve could greatly increase the extinction and efficiency of the modulator.

Experiments of all-optical modulation utilizing the Fano line-shape was reported by Mehta et al [47]. By adjusting the fiber position, they were able to couple to the fundamental and first excited TE modes in the waveguide, and observed a Fano line-shape transmission spectrum. The modulator showed higher extinction when the cavity exhibited a Fano resonance as opposed to a Lorentzian resonance.

Here we hope to extend the concept to electrically-driven optical modulators, and also design devices that consistently show Fano resonances, without dependence on the fiber position. We will start by quickly reviewing the basic physics of silicon photonic crystal modulators, and then characterize a few traditional devices to have a baseline expectation of the devices. In the next section of the Chapter, we will review the theory for obtaining Fano resonances, and then present results from the two ways we tried to achieve Fano resonances. Unfortunately, we were unable to characterize the actual Fano modulators due to time constraints, but investigating that would be the obvious next step.

4.2 Silicon Photonic Crystal Modulators

The architecture of the silicon photonic modulators are shown in Figure 4.1. The figure is adapted from the paper by Mehta et al [15], and shows the entire structure of the modulator on chip. To couple light from a fiber onto the chip, we use a standard grating coupler designed by the Popovic et al [53]. The light propagates through the silicon bus waveguides to the resonant cavity, at which the light is reflected or transmitted. The transmitted light is coupled out of the waveguide to an output fiber. The details of designing the silicon modulator and grating couplers is discussed in previous work [46] [53], so it will not be discussed in depth here.

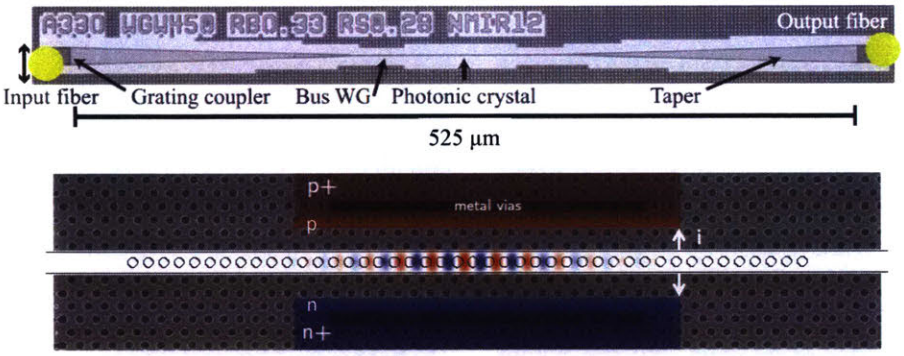

Figure 4.1: Basic Architecture of Modulator Devices
(a) This picture shows the entire modulator structure on the chip. The yellow spots mark the approximate location the fibers should be. (b) A zoomed-in image of the photonic crystal resonant cavity. The field profile of the resonant wave is overlayed on the PhC image.

These modulators were fabricated using two different processes, one with Micron Technologies and one with CNSE. The devices on the Micron chips are older, and were designed by Karan Mehta. On both of the chips, there are a few variants of the photonic crystal modulators. There are passive devices, which are the modulators without any of the accompanying electronics, as well as active devices, which are the full modulators. The structure of the defect cavity is the same across all of the modulators, but the number of holes (mirror holes) confining the mode to the defect cavity varies. This helps us characterize the intrinsic loss of the devices on this chip, and allows for a variety of Q's and peak transmissions when characterizing modulators. The CNSE chip also has more interesting modulators that have varied architectures to achieve Fano resonances. In addition to the default TE, Lorenztian photonic crystal modulators, there are two different variations in transmission grating, and four types of asymmetric tapers connecting the bus waveguide to the resonant cavity. These variations will be discussed in this Chapter.

4.2.1 Waveguiding in Silicon

The waveguide body is 0.480 microns by 0.220 microns, and has 0.100 thick wings that extend about 3.5 microns on either side (see Figure 4.2). The modes of the waveguide were simulated using CST Microwave, a fully vectorial electromagnetic wave solver. This waveguide design supports multiple modes, including both the fundamental TE and TM modes and higher order TE modes. This feature is important to achieve a Fano line-shape, which requires the interference of two different modes.

The fundamental TE mode has a propagation constant $\beta_{TE,1} = 10.627\ \mu\text{m}^{-1}$, and the propagation constant for the first excited TE mode is $\beta_{TE,2} = 9.111\ \mu\text{m}^{-1}$. For fundamental TM mode, $\beta_{TM,1} = 6.994\ \mu\text{m}^{-1}$.

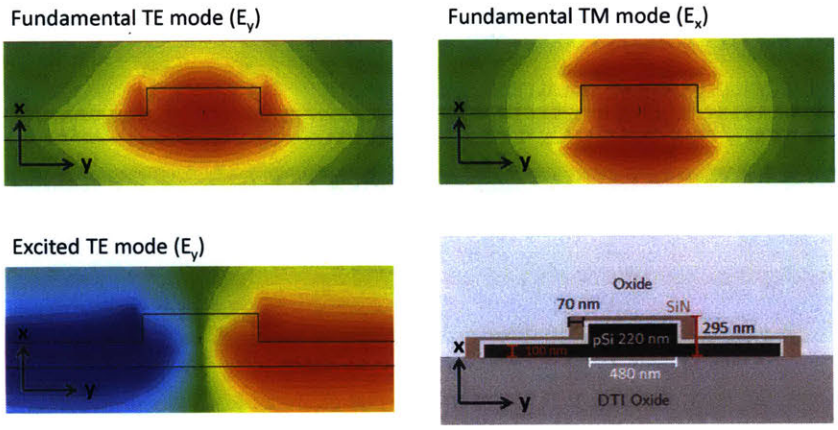

Figure 4.2: Modes of the Silicon Waveguide
The figure shows the a cross-section view of the waveguide, and shows the mode profiles for the fundamental TE, fundamental TM, and first exited TE mode. The propagation constants of each or mode are summarized in the table.

4.2.2 Theory and Design of Resonator Cavity

The 1D PhC resonant cavity for the modulator and the waveguide was designed in previous work [46]. The photonic crystal is a series of holes with radius $r = 0.28a$ in the silicon waveguide. The main defect in the PhC is 2 holes with $r = 0.33a$,but to reduce reflective losses, the hole sizes are tapered from $r = 0.28a$ to $r = 0.33a$ and back across 20 holes. This set of holes is what we will refer to as the defect cavity. The number of mirror holes M is defined as the number of $r = 0.28a$ holes on each side of the defect.

The band structure of the 1D row of holes with radius $r = 0.28a$ and $r = 0.33a$ is shown in Figure 4.3. Near $k = \pi/a$ for (quasi)-TE polarization, the band for the $r = 0.33a$ PhC structure is in the band gap of the PhC structure with $r = 0.28a$. Therefore, the defect cavity of larger holes supports a mode that is not

allowed in the remainder of the PhC. That mode is confined to the defect cavity and is called the resonant mode of the cavity.

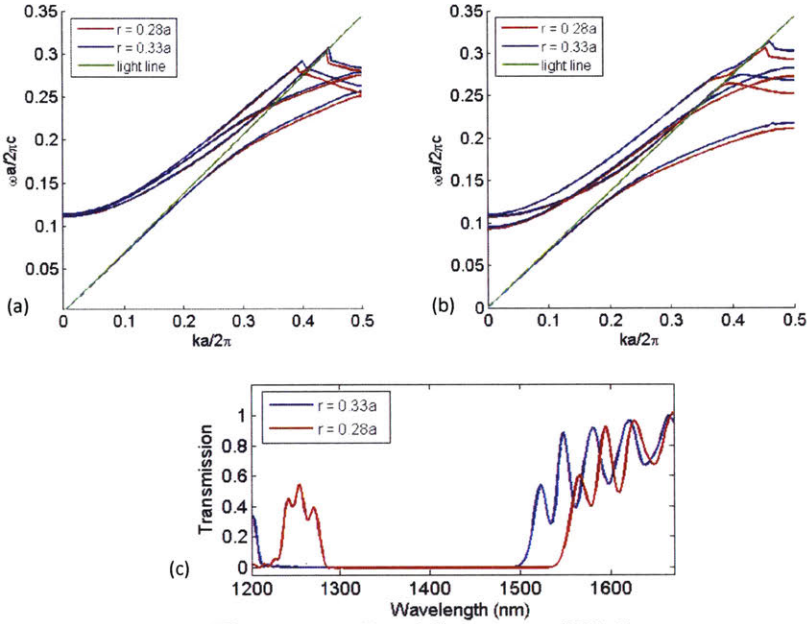

Figure 4.3: Band Structure of PhC
(a) shows the band structure assuming quasi-TM polarization, and (b) shows the band structure assuming quasi-TE polarization, for $r = 0.28a$ and $r = 0.33a$. (c) shows the predicted tranmission curve for the fundamental TE mode when $r = 0.28a$ and when $r = 0.33a$.

4.2.3 Characterization of Passive Cavities

The first set of cavities were fabricated at Micron Technologies, using a 180 nm bulk CMOS process. The second set of cavities were fabricated at CNSE, using a 65 nm bulk CMOS process. The CNSE is a newer process, so the processing is still being perfected to minimize losses. The devices are fabricated in polysilicon, covered first with a thin layer of SiN to reduce material loss, and then covered with SiN.

The measurements below have been corrected for the coupling and waveguide loss, which was about 20 dB for the Micron measurements and about 13 dB for the CNSE measurements.

The chips were characterized by observing the changes in the Q of the resonant peak with the number of mirror holes. For devices with larger number of mirror holes, the coupling from the bus waveguide to the cavity decreases, so we expect the peak transmission to decrease and the Q to increase. By observing the variation in peak transmission with Q_{tot}, the intrinsic Q (Q_0) of the cavity can be predicted using the

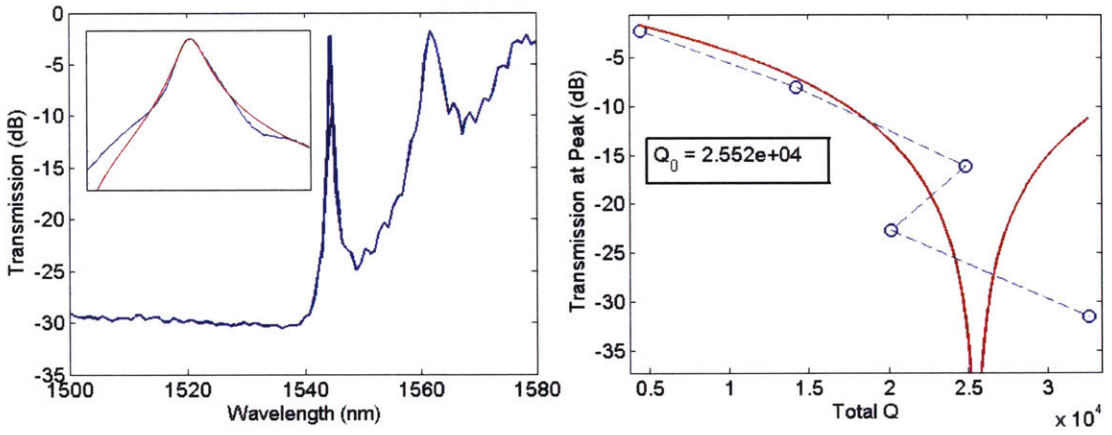

Figure 4.4: Characterization of Passive Cavities in Micron Process
Characterization of chip and simple resonator cavities. As expected, increasing the number of mirror holes increases the quality factor Q of the resonator, but also increases the insertion loss of the resonant cavity. By comparing the transmission at the resonant peak to the quality factor of the cavities, we can determine the loss inherent to the physical device. For this chip we measured an intrinsic Q of 25520.

relation $T_{peak} = (Q_{tot}/Q_{wg})^2 = (1 - Q_{tot}/Q_0)^2$. The intrinsic loss is defined as $Q_0^{-1} = Q_{tot}^{-1} - Q_{wg}^{-1}$ and represents the loss of the device. It typically is affected by the fabrication process.

The intrinsic Qs of the devices, which corresponds to the absorption and radiative losses of the resonant cavity, are both quite low. If these losses are reduced, the modulator devices could show improved performance.

Observations

The behavior of the transmission with respect to fiber position and polarization was observed. The transmission line-shape of the cavity is sensitive to the positioning of the fibers with respect to grating couplers, but is not sensitive to the polarization. This confirms that the waveguide is able to support modes in addition to the fundamental mode, and that the grating coupler is optimized for coupling to TE polarized input light.

By changing the lateral position of the fiber, such that the fiber is no longer centered with respect to grating coupler, the input light can couple to the first excited TE mode. As we will explain more in depth later in the chapter, coupling to the first excited TE mode causes the asymmetry in the resonant peak. Depending on which side the fiber is relative to the grating, the asymmetry of the peak changes sign. This is consistent with the work presented by Mehta et al [47].

When the TM component of the input light is increased, the detected transmission decreases because less

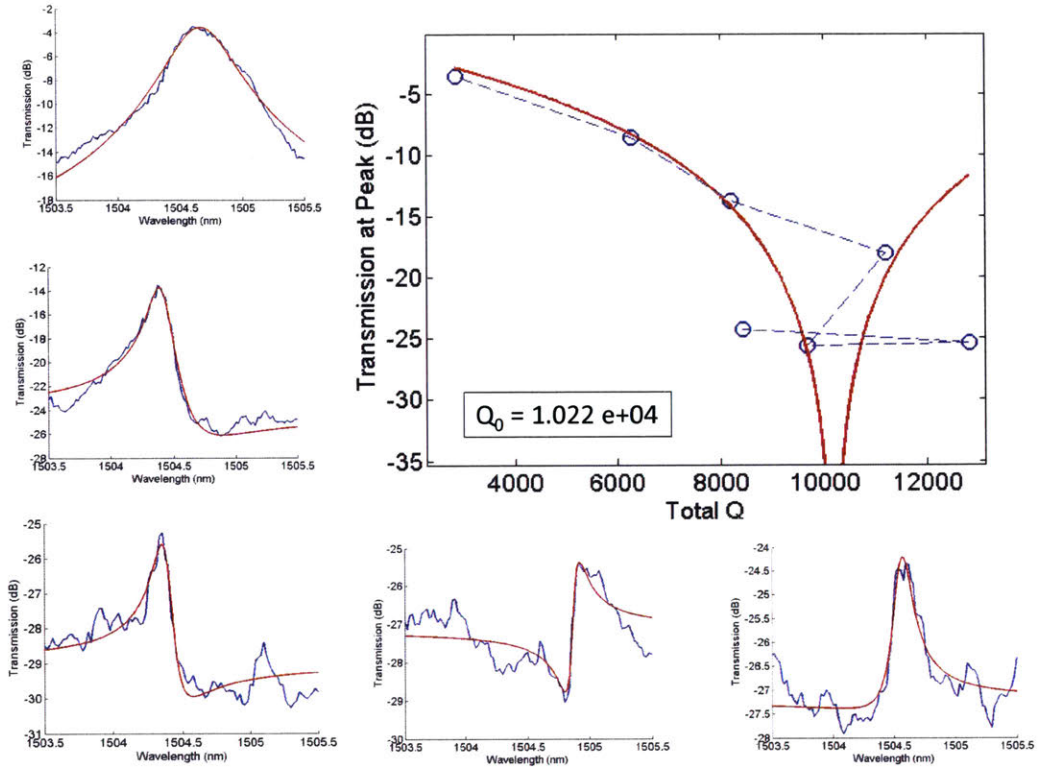

Figure 4.5: Characterization of Passive Cavities in CNSE Process
Characterization of chip and simple resonator cavities. As expected, increasing the number of mirror holes increases the quality factor Q of the resonator, but also increases the insertion loss of the resonant cavity. By comparing the transmission at the resonant peak to the quality factor of the cavities, we can determine the loss inherent to the physical device. For this chip we measured an intrinsic Q of 10220. For devices with higher mirror holes, it was difficult to obtain a symmetric resonance peak.

light is coupled to the waveguide. The transmission curves are all normalized to the waveguide transmission assuming a purely TE input. The transmission line shape does not change at all, suggesting that the only change is reduced coupling from the fiber to the waveguide. We expect that if each transmission curve was normalized to the wavegide transmission for the corresponding mixed TE/TM input, the transmission curves would all appear to be the same.

4.2.4 Characterization of Active Cavities

We investigated the sensitivity of cavity performance on the design of the p-i-n junction around the cavity for the Micron chip. Though there were several variations on the distance of the p/n and p+/n+ doping regions from the resonant cavity, we will summarize the results of only two cavities. In general, decreasing

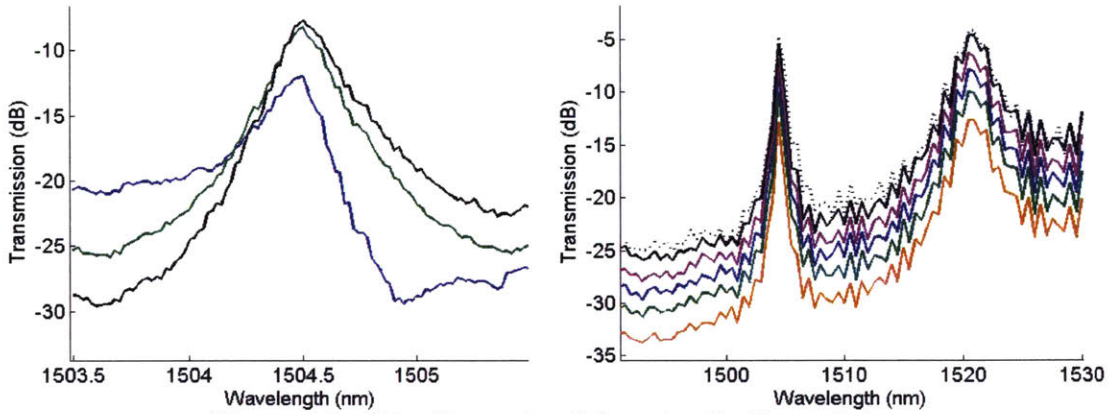

Figure 4.6: Other Parameters Influencing the Transmission
(a) shows how the symmetry of the resonant peak changes with the lateral (y) position of the fiber relative to the grating coupler. (b) shows how the transmission varies as the input polarization has an increasing TM component. The dashed line represents a reference transmission spectrum for a TE-only input.

the distance between the p/n or p+/n+ doped regions increased loss significantly, though the sensitivity of the resonant wavelength was also increased due to the larger change in carrier density with applied voltage. The p+/n+ doped regions tended to generate more loss than the more lightly doped regions.

Here we will report measurements taken for two modulator devices. The p-i-n junction is characterized by the distance from which the p/n and p+/n+ doping regions start with respect to the edge of the waveguide. The first device has a large 'i' region. For this device, the p/n regions in the wing regions start 2 rows of holes away from the body of the waveguide, as shown in Figure 4.1. The 'i' region is approximately 1.31 microns wide. The second device has a small 'i' region. Here the p/n regions start right next to the waveguide, and the width of the 'i' region is approximately 0.48 microns wide. For both devices, the p+/n+ regions start a 3 rows of holes from the waveguide. The defect cavity for both devices has 12 mirror holes. The transmission curves and i-v curves for these devices are shown in Figure 4.7. We expect the increased insertion loss (reduced peak transmission) is a result of the doping regions adjacent to the defect cavity.

Because the resistance of the p-i-n junction is higher for the large 'i' cavity, the index change due to carrier depletion or injection will be less than for the small 'i' cavity. Therefore, we expect to see lower extinction modulation for a given peak-to-peak operating voltage. The characterization results of the large and small 'i' regions, shown in Figures 4.8 and 4.9 respectively, agree with our expectations.

Notice that at high bias voltages, bistability of the resonant cavity causes a sharp drop in the DC

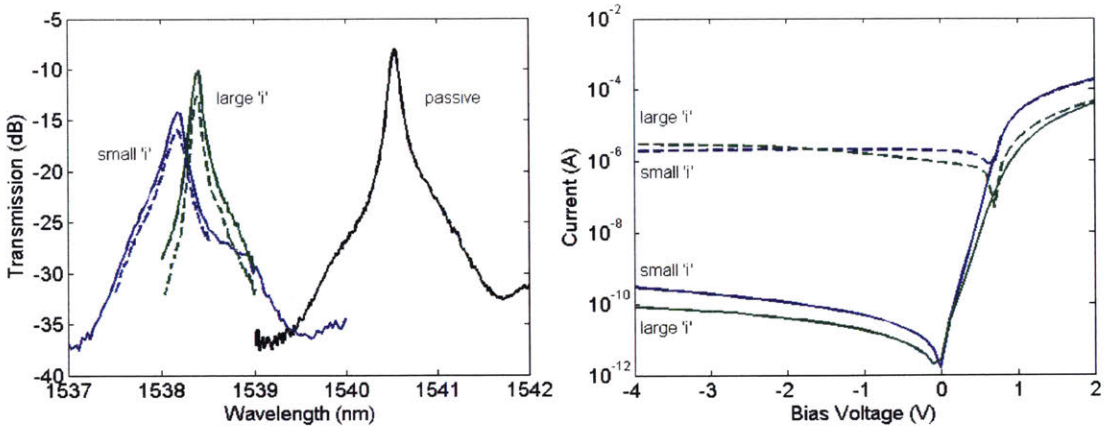

Figure 4.7: Characterization of Active Cavity with Large Intrinsic Region
(a) Transmission curves of the resonant cavity at different reverse bias voltges. (b) Modulation extinction versus frequency. (c) High (solid) and low (dashed) intensity levels during modulation, as a function of frequency. (d) Shows extinction as a function of wavelength for various bias points, with a 4V peak-to-peak applied voltage.

transmission spectrum. Since the bistability is observed at high reverse bias voltages, we expect the bistability to be a thermal effect, induced by the Joule heating from the high energy charge carriers. Because the bistability is a thermal effect, it likely will be relatively slow. Therefore, when the bistable device is modulated at a high frequency, the bistability does not generate increased extinction. When plotting the high and low intensity values of the transmitted power as a function of wavelength, the transmission spectrum still shows the bistability. However, both the 'high' and 'low' values of the modulated signal drop from high transmission to low transmission at the same wavelength. Therefore, it appears that modulation at 100 MHz or greater frequencies is too fast for bistability to affect modulation.

The modulation behavior of the cavities under forward bias was also observed. All the devices seem to have similar cut-off frequencies/similar frequency responses, regardless of whether they are operated at forward or reverse bias . We did not optimize the positioning or structure of the pads, so it likely is that the capacitance of the pads is the dominant capacitance of the modulator, as opposed to the capacitance of the junction. This suggests that by designing better electrical contacts, the frequency cut-off of these modulators could be much higher. The pads used for these junctions were designed for 100 μm pitch GSG probes, and were 60 μm by 60 μm in size. The p-i-n junction was about 6.4 microns wide.

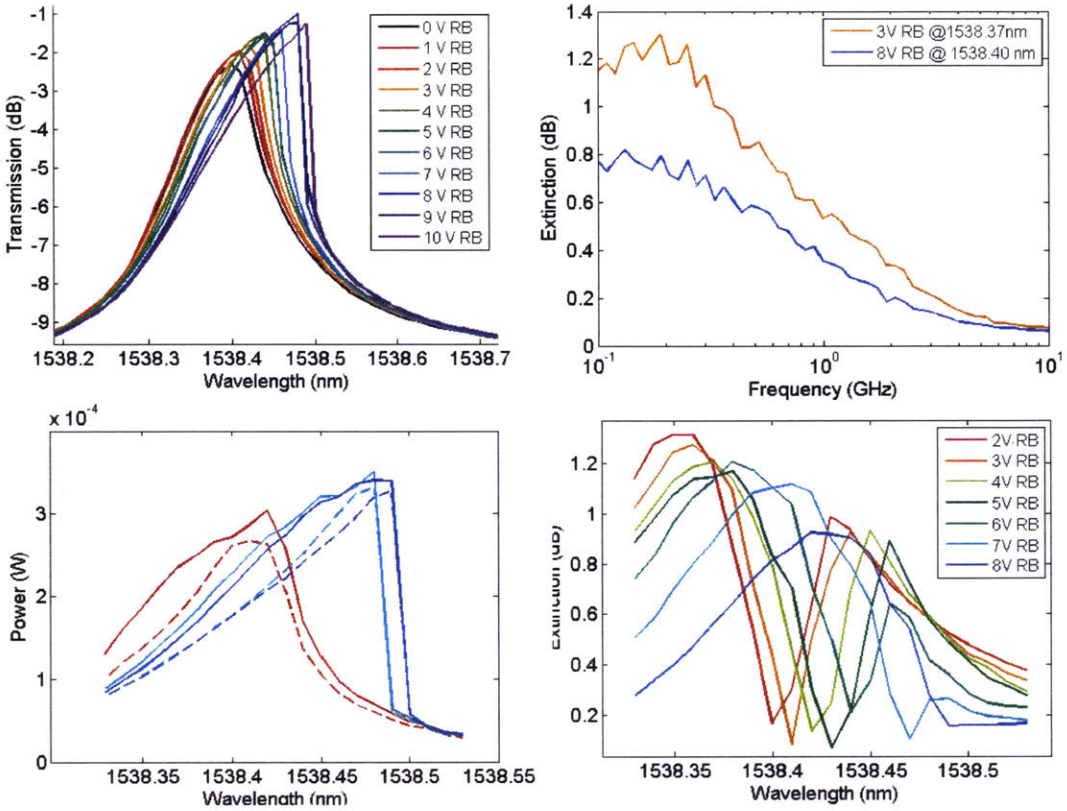

Figure 4.8: Characterization of Active Cavity with Large (1.31 μm) Intrinsic Region (a) Transmission curves of the resonant cavity at different reverse bias voltges. (b) Modulation extinction versus frequency. (c) High (solid) and low (dashed) intensity levels during modulation, as a function of frequency. (d) Shows extinction as a function of wavelength for various bias points, with a 4V peak-to-peak applied voltage.

4.3 Theory and Design of Fano Cavities

Fano line-shape resonances occur when a non-resonant mode interferes with a discrete resonant mode. Therefore, the modulator architecture would have to be such that the fiber input coupled to both the fundamental TE mode and another continuous propagating mode.

Consider the case when the input light couples to the fundamental resonant mode and an excited propagating mode that has a propagation loss of $(1-\eta)$. Assume the coupling efficiency to the fundamental mode is κ_i at the input and κ_o at the output, the coupling efficiency to the excited mode is $1-\kappa$, and no other modes are excited.

With both the resonant cavity mode and a propagating mode, the transmitted field at the output is

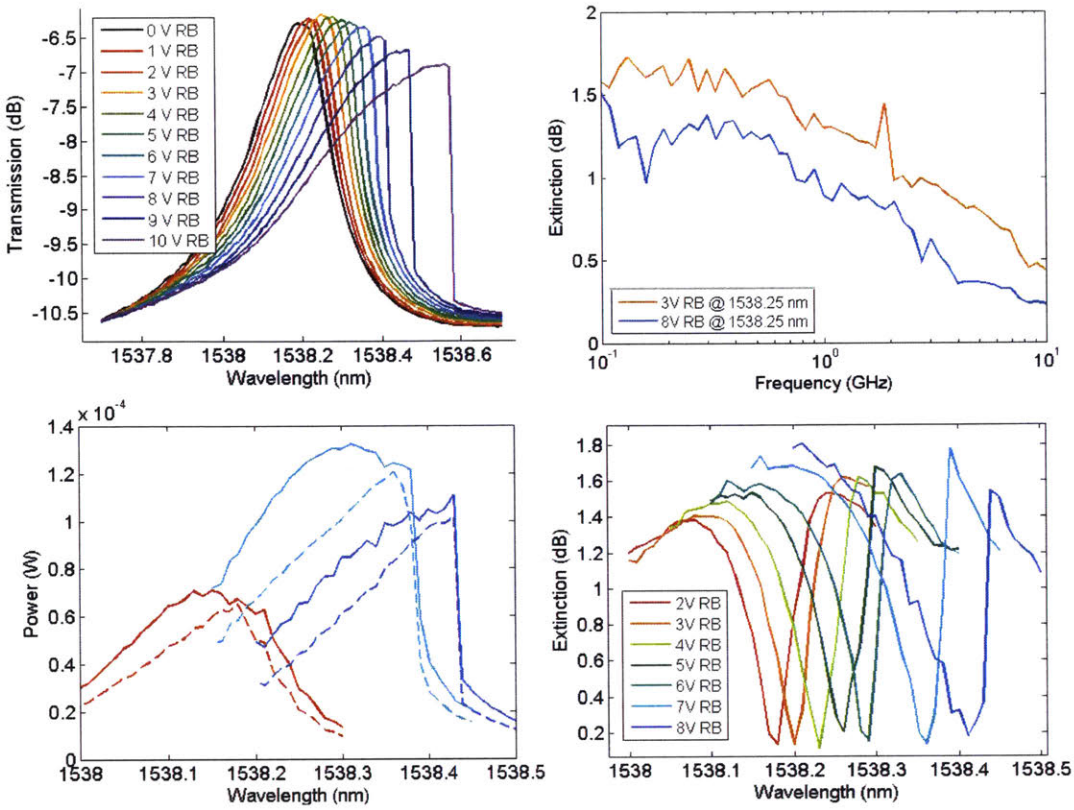

Figure 4.9: Characterization of Active Cavity with Small (0.48 μm) Intrinsic Region (a) Transmission curves of the resonant cavity at different reverse bias voltges. (b) Modulation extinction versus frequency. (c) High (solid) and low (dashed) intensity levels during modulation, as a function of frequency. (d) Shows extinction as a function of wavelength for various bias points, with a 4V peak-to-peak applied voltage.

$$t = \frac{\sqrt{\kappa_i \kappa_o}(2/\tau_{wg})}{j(\omega - \omega_0) + 1/\tau_{tot}} + \sqrt{(1-\kappa_i)(1-\kappa_o)}\eta e^{j\phi}. \tag{4.1}$$

The intensity is therefore

$$T = |t|^2 = \frac{\kappa_i \kappa_o (2/\tau_{wg})^2}{(\omega-\omega_0)^2 + (1/\tau_{tot})^2} + (1-\kappa_o)(1-\kappa_i)\eta^2 + \frac{4}{\tau_{wg}}\eta\sqrt{\kappa_i\kappa_o(1-\kappa_i)(1-\kappa_o)}\frac{\cos(\phi)/\tau_{tot} - \sin(\phi)(\omega-\omega_0)}{(\omega-\omega_0)^2 + (1/\tau_{tot})^2} \tag{4.2}$$

This bulky equation helps us understand how the propagating mode affects the resonant cavity mode, but it has too many fitting parameters. The Fano lineshape can be more concisely expressed as [27],

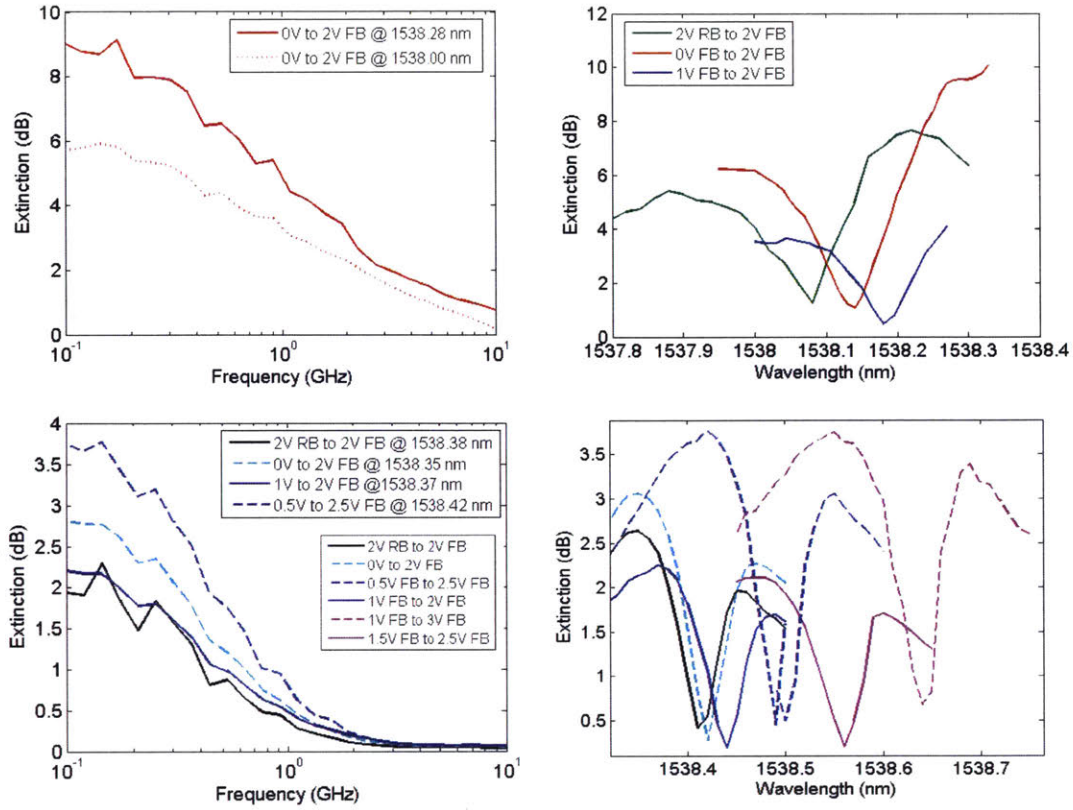

Figure 4.10: Characterization of Active Cavity in Forward Bias
(a) Extinction versus frequency for modulation from 0V to 2V forward bias at different operating wavelengths. (b) Extinction versus wavelength for different modulation voltages. (c) and (d) are the same as (a) and (b) but for the large i region device.

$$F = A_0 + F_0 \frac{(q + 2(\omega - \omega_0)/\gamma)^2}{1 + (2(\omega - \omega_0)/\gamma)^2}. \tag{4.3}$$

According to this expression, the asymmetry of the Fano resonance is maximized when $|q| = 1$. When $|q|$ is much less than 1 or much greater than one, then the transmission curve appears Lorenztian. The sign of the peak depends on the sign of F_0.

Comparing Equations 4.2 and 4.3, we determine that the quality factor of the cavity can be determined from $\gamma = \omega_0/Q_{tot}$. Comparing the terms of both equations, we can determine that

$$\gamma = \omega_0/Q_{tot} \tag{4.4}$$

$$q = \frac{-(1+K\cos\phi) \pm \sqrt{2+2K\cos\phi}}{K\sin\phi}$$

$$F_0 = -2\eta\sqrt{\kappa_i\kappa_o(1-\kappa_i)(1-\kappa_o)}\frac{\tau_{tot}}{\tau_{wg}}\sin\phi/q$$

$$A_0 = (1-\kappa_o)(1-\kappa_i)\eta^2 - F_0$$

, where $K = \eta\frac{\tau_{wg}}{\tau_{tot}}\sqrt{\frac{(1-k_i)(1-k_o)}{k_i k_o}}$. When deriving these definitions, we used the relation $Q_{tot} = \tau_{tot}\omega_{tot}/2$.

Here, we see that the maximum asymmetry of the peak, which is given by q, depends on the waveguide coupling parameters, the total lifetime of the cavity, and also the phase of the propagating wave with respect to the confined mode. Therefore, in order to reliably fabricate Fano modulators, in addition to knowing the quality factor of the cavity and the coupling strength to the waveguide, one would need to understand and control how the phase between the two modes is determined.

Since both the fundamental TM modes and the first excited TE mode are not confined to the cavity, they both potentially could exhibit Fano resonances. To couple into these modes, we slightly modify the modulator architecture, as is explained in the following sections.

4.3.1 Exciting Higher Order Spatially Confined Modes

As seen in some of the passive measurements and in the literature [47], the second order excited mode can be excited by shifting the fiber position with respect to the grating coupler. Quick simulations in MEEP confirmed this. However, ideally, we would be able have a Fano resonator that is not sensitive to fiber position.

To achieve this, we hope to use an asymmetric taper that excites both the fundamental and the excited mode of the waveguide. The input waveguide is chosen such that the TE mode is the only mode that is well-confined to the body of the waveguide–the fields of the excited modes are predominantly in the wings of the waveguide.

By changing the width at the output of the taper, the coupling efficiency to the fundamental and excited modes can be engineered. For output tapers that are wider than the waveguide itself, the asymmetric taper is connected to the waveguide via a symmetric taper. The tapers at the input and output are mirror images of each other. Increasing the waveguide width decreases the power transmitted by the two relevant modes,

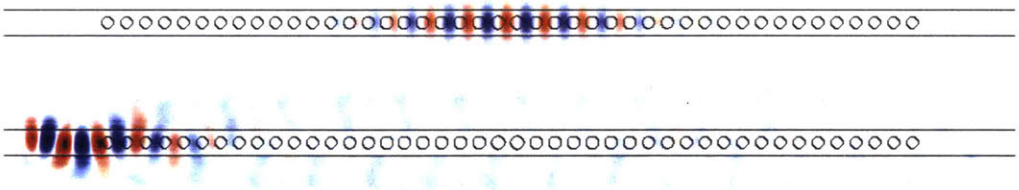

Figure 4.11: Transmission through Crystal with Offset Source
The top image is the field in the resonant cavity when the input source is perfectly centered on the waveguide. The bottom image is the field when the input source is along the upper edge of the waveguide. The first excited mode profile is visibly propagating through the entire crystal.

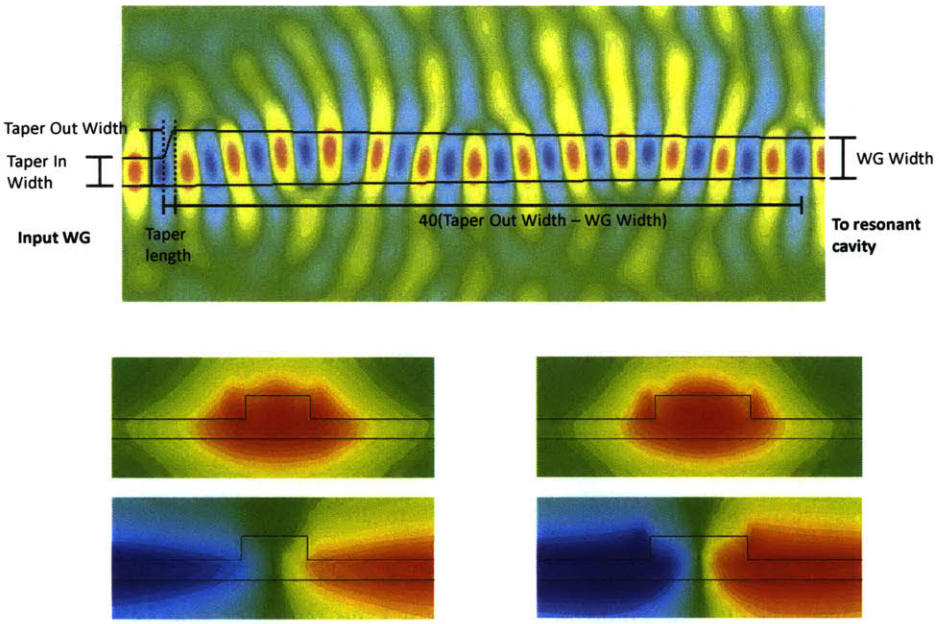

Figure 4.12: Fano Taper Design
The picture on top shows the field profile as the excited wave propagates through the taper, and also shows the nomenclature for each part of the taper. The bottom pictures show the mode profiles of the waveguide assuming (left) "taper in width" = 0.33 μm and (right) "wg width" = 0.48 μm. The mode profile on top is the fundamental mode and the mode profile on the bottom is for the first excited mode.

likely because coupling to higher order modes is increased. Increasing the taper length increase the overall power transmitted by the two modes, but the coupling efficiency to the excited mode is decreased because the expansion of the waveguide is closer to adiabatic.

The experimental results of devices with various taper lengths and taper widths are shown in Figures

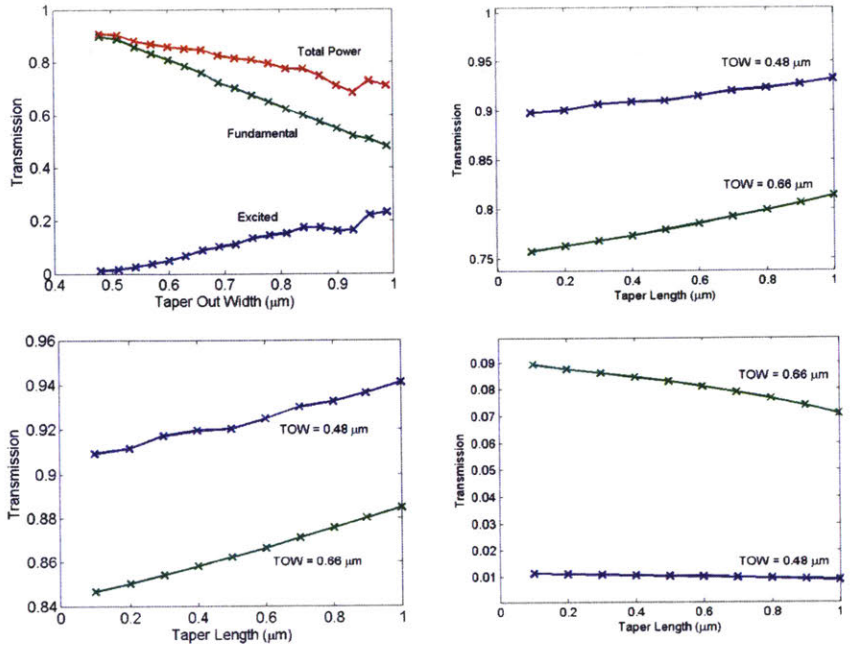

Figure 4.13: Fano Taper Design
(a) shows the coupling efficiency of fundamental mode at the input of the taper to the fundamental and first excited mode at the output of the taper, as well as the total power transmitted with those two modes. (b)-(d) show effect of the taper length on the coupling efficiency to the fundamental mode, the total power transmitted at the output of the taper, and the coupling efficiency to the first excited mode. TOW refers to the output width of the taper.

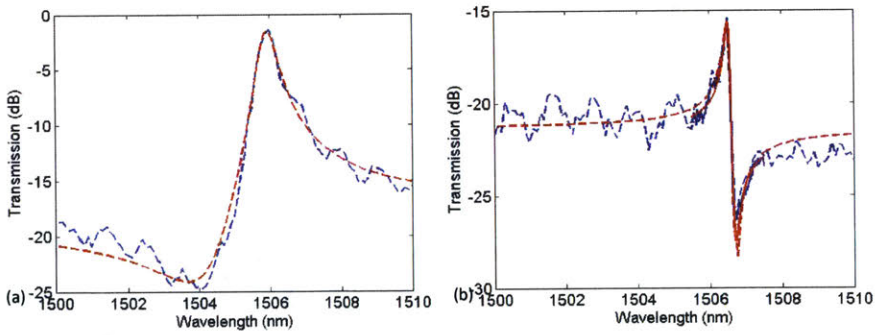

Figure 4.14: Fano Transmission Spectra of Tapered Devices
The graphs show the transmission spectra for two example devices with an asymmetric Fano resonance. (a) has a taper length of 0.1 μm and a taper output width of 0.48 μm (device P2F1), and has 8 mirror holes. (b) has a taper length of 0.1 μm, a taper output width of 0.48 μm, and 18 mirror holes (device P2F2).

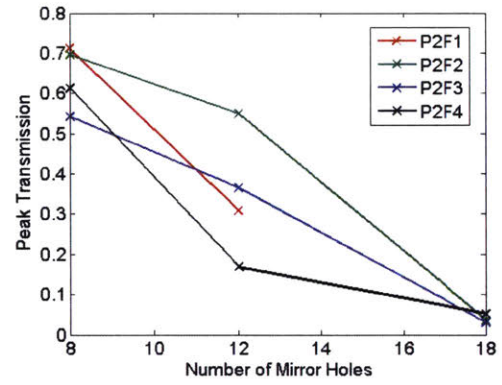

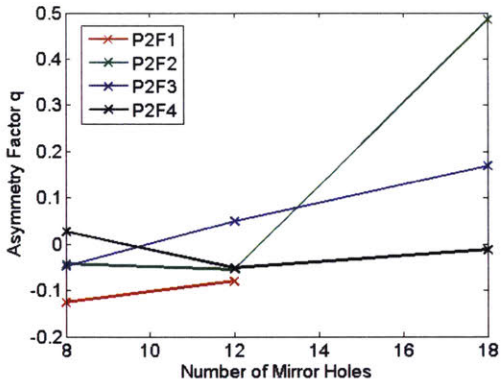

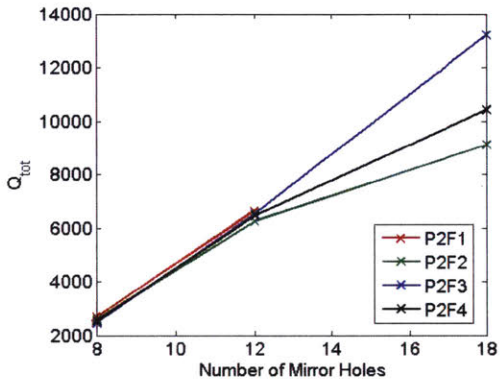

Device Name	Input Width	Output Width	Taper Length
P2F1	0.33 μm	0.48 μm	0.1 μm
P2F2	0.33 μm	0.48 μm	0.8 μm
P2F3	0.33 μm	0.66 μm	0.1 μm
P2F4	0.33 μm	0.66 μm	0.8 μm

Figure 4.15: Summary of Measurements on Fano Tapered Devices
The graphs show different fitting parameters (peak transmission, asymmetry, and Q_{tot}) for devices with various taper out widths and taper lengths, as summarized in the table in the figure. Recall that the Fano peak is most asymmetric when $|q| = 1$. Devices were on the CNSE chip.

4.14 and 4.15. It appears that the Fano effect is more prominent in devices with shorter taper lengths and narrower widths at the taper output. However, no trends can really be determined from these measurements, since the phase between the two modes is not considered. But, using the Equations 4.4, the expected phase between the two modes can be determined to provide insight on controlling the phase between the modes. If the taper can be better engineered in the next iteration of devices, better Fano modulators could be tested.

4.3.2 Exciting Both Transverse Electric and Transverse Magnetic Modes

It was also proposed that the Fano line-shape could be created by interfering the TE an TM modes. Since the photonic crystal design has no band gap for TM polarized light, the TM mode is able to propagate through the PhC freely. Since the TE fundamental mode is resonant at the defect cavity, while the TM mode is a propagating mode, the Fano resonance might be able to arise from interference between the TE and TM

modes. TE and TM modes are considered orthogonal because they utilize different vector components of the electric field. But in a high-index 3D system, the modes are not perfectly orthogonal and have non-zero power in other field components. Therefore, the two modes still might interfere with each other to some degree.

We designed grating couplers that had comparable far-field radiation patterns for both the TE and TM modes. Because of time reversal symmetry, the approximate effectiveness of the grating coupler can be determined by its farfield radiation pattern. The directivity of the far-field patterns determines the angle the fiber output should be for maximum coupling. For our purposes, we would need the TE and TM modes to have high directivity in the same direction, though it was accepted that coupling efficiency would likely decrease. The grating couplers were not carefully optimized, since this was just for proof of concept.

Grating couplers use 1D periodic elements to diffract the light from inside the chip out-of plane. According to the Bragg condition, the scattered waves exhibit constructive interference when $k_z = \beta_{wg} + nk_{gr}$, for $n = ..., -1, 0, 1, ...$ is satisfied. The propagation of the mode in the waveguide is β_{wg}, and the effective grating wavevector is approximated as $k_{gr} = \frac{2\pi}{n_{tooth}w_{tooth}+n_{gap}w_{gap}}$, where n is the effective index of the grating tooth or the SiO2 gap between the teeth, and w is the width of the tooth in the z direction.

Solving for the coupling angle ϕ from $k_z = k \sin\phi$, we get

$$\phi = \sin^{-1}(\frac{\beta - k_{gr}}{n_{cl}(2\pi/\lambda)}) \tag{4.5}$$

For the fundamental TE mode, the β_{wg} is roughly 10.627 μm^{-1}. The current grating design used for these devices have teeth that are 0.380 μm wide and spaced 0.25 μm apart. The coupling angle is about 8 degrees.

The idea was that to couple both TE and TM polarized light to the waveguide, a k_{gr} could be found such that the constraint

$$\beta_{wg,TE} + nk_{gr,TE} \approx \beta_{wg,TM} + mk_{gr,TM} \tag{4.6}$$

is met for some combination of integers n and m. However, k_{gr} for TE and TM modes is different given the same structure, since the effective indices of the teeth and spaces are different for the two polarizations. Furthermore, from our simulations it appears that the effective grating wavevector can be calculated only for a single tooth and gap, because at each interface from silicon to oxide a significant portion of the wave is scattered. An approximate solution could potentially be found by using methods like the Marcatili to

estimate the effective index of the grating components, but that was not attempted here [45].

Our approach was to alter the grating coupler design such that the grating was periodic with every two teeth. The spacing between the teeth were all of width d_{gap} and teeth had widths of $d_{tooth,1}$ and $d_{tooth,2}$, as is shown in Figure 4.16. During our simulations, we assumed that the thickness of the SiN cladding layer was 40 nm, though the cladding thickness on the physical chip was closer to 70 nm.

Ultimately we chose two designs. Design 1 had $d_{gap} = 0.396$ μm, $d_{tooth,1} = 0.324$ μm, and $d_{tooth,2} = 0.780$ μm. Design 2 had $d_{gap} = 0.340$ μm, $d_{tooth,1} = 0.340$ μm, and $d_{tooth,2} = 0.85$ μm.

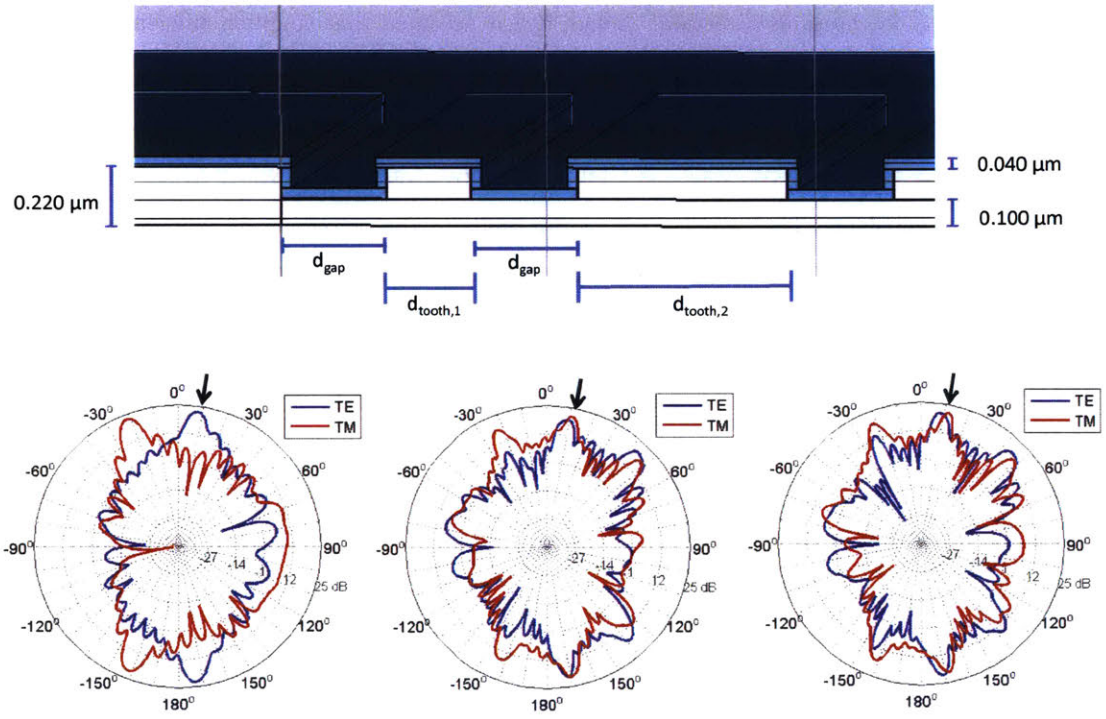

Figure 4.16: TE/TM Grating Coupler Design
The picture on top shows the nomenclature used to define the grating pattern. The plots on the bottom show the far-field directivity patterns for purely TE, Design 1, and Design 2 grating couplers. The arrows correspond to the approximate angles the fibers will be at with respect to the grating coupler.

Simulation results are shown in Figure 4.16. Though the directivity of the grating is somewhat compromised by roughly 2-3 dB because there is stronger radiation in other directions, the farfield radiation patterns for both TE and TM modes show peaks at around 10 degrees.

Experimental results are shown in Figure 4.17. As the graphs show, as the TM component of the incident light increases, more light passes through the waveguide, so the peak height decreases with respect to the

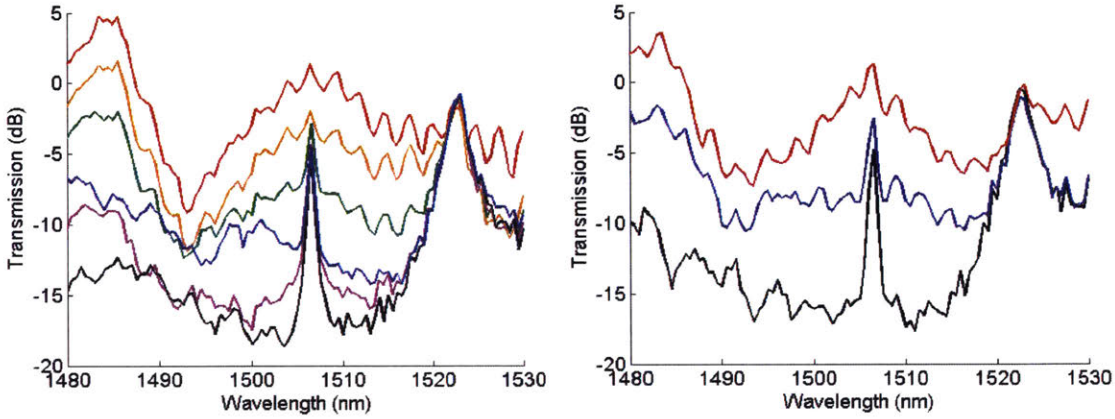

Figure 4.17: TE/TM Grating Coupler Device Measurements
Transmission spectra with different input polarizations for modulators with Design 1 and Design 2 grating couplers. Devices were on the CNSE chip.

background transmission. When the TM polarization dominates, the transmission spectrum of the photonic crystal cannot be detected. No interference is observed. Therefore, the TE and TM mode will not interfere with each other and generate a Fano line-shape transmission spectrum. Note that the normalization of power was done using an average transmission efficiency through the waveguide, so the regions of the transmission spectra that exceed zero are artifacts of the normalization, and do not represent gain of any sort.

4.4 Summary

We showed that Fano interference could be obtained by interfering the fundamental and first excited TE modes, but could not be obtained by interfering the fundamental TE and TM modes. In theory, the fundamental and first excited modes in an "infinite index rectangular waveguide" (the optical analogy to a particle in an infinite well system for quantum mechanics) should also be orthogonal. However, both modes have a dominant E_y component, so when the modes do overlap, the modes interfere. In contrast, the TM mode has a dominant E_x component, so the interference efficiency is limited by the mode overlap of either E_y or E_x, which will already is small.

Because of previous work [47], we expect that Fano interference will improve modulator extinction and efficiency. However, we have yet to test the active Fano devices to ensure that they work as expected.

In the future, more work needs to be to optimize the modulators. One task would be to characterize the phase between the fundamental and first excited TE modes. This could be done by systematically varying the lengths of the cavities. Another would be to design the supporting electronics to reduce its capacitance and reduce its effect on the quality factor and insertion loss of the resonant mode.

Chapter 5

Summary and Future Work

This thesis presented work on three different projects. Each project was an application of sub-wavelength photonic structures, but appear very different because of the system's different boundary conditions. We first used theory or numerical simulations to predict the behavior of each system, and then verified our simulation results with experiments. For all of the projects, a next iteration device needs to be designed in order to improve on what we presented here.

In summary, the first project was the large aperture, miniature spectrometer. By using a large area 1D diffraction grating, we built a spectrometer that used the Talbot effect to resolve different wavelengths. Conservatively, the resolution was 4 nm, though wavelengths of less than 1 nanometer were differentiable. We also found a spectrometer design that can potentially have a resolution of less than 0.5 nm resolution. The spectrometer, excluding the read-out electronics and the extra space, could fit within a 10 mm x 10 mm x 5 mm box. Including the extra components of the spectrometer, the spectrometer was still able to fit within a 25 mm x 25 mm x 20 mm box. The etendue of the spectrometer was approximately 0.033 mm^2. This was calculated assuming a 1 degree acceptance angle. Though this was not explicitly tested, our simulations suggested that a the wavelength can still be detected, albeit at a lower resolution. We also saw broadened peaks for clearly diverging light sources, so this estimate is reasonable. While we were able to successfully miniaturize the spectrometer, we still were unable to completely and accurately explain some parts of our experimental results. For example, the measured wavelength was always offset from the actual wavelength, and the offset varied with detector position. Our spectrum also sometimes showed two peaks, instead of a single peak, that corresponded to the incident wavelength. In the future, we could improve the spectrometer increasing its acceptance angle. This would improve the light-collecting power of the spectrometer, and

reduce the sensitivity of the spectrometer to the incident angle of the beam.

The second project was the photonic crystal barcodes. By engineering the defect cavity of the resonant cavity, the back-scattering efficiency can be increased. We presented an initial set of measurements on CMOS PhC barcodes to better understand the resonant modes and how the defect cavity modfications affected them. The defect cavity contained three resonant modes, two of which had strong vertical emission but low Q, while one mode had low vertical emission but high Q. The highest Q mode that we measured was roughly 800, which corresponds to a FWHM linewidth of roughly 1.75 nm. This fell short of our target linewidth of less than 0.5 nm, but is narrower than other proposed barcodes like quantum dots. If we obtain a better understanding of photonic crystals in confined materials in order to explain some of the phenomena we observed, like the shifting of the resonant frequency with device size and fine structure within in the resonant peaks, we might be able to use this knowledge to engineer barcodes with even narrower linewidths.

The third project was the Fano resonance modulators. We investigated generating Fano resonances by coupling to the fundamental and excited TE mode, and also by coupling to the fundamental TE and TM mode. Fano interference was observed only using the first method. We attempted to characterize the asymmetry of the Fano line-shape depending on the coupling efficiency to the two modes, but were unable to do so because we did not consider the phase between the two resonant modes. More work needs to be done in order to present modulators that will reliably exhibit Fano resonances, and the Fano modulator's extinction and efficiency still need to be characterized.

5.1 Next Steps and Future Work

Though the next steps for these projects were mentioned briefly in the previous chapters, we will summarize and elaborate on the work that needs to be done to finish or improve each project.

5.1.1 Talbot Spectrometer

As of now, we are able to resolve two different laser lines that are about 3 nm apart. The theoretical resolution of this spectrometer, assuming plane-wave incidence, was calculated to be about 1 nm. To improve the current spectrometer design, we should first understand why the experimental resolution is not as small as predicted– this might be a result of an imperfectly collimated beam at the input, or perhaps it is line-broadening due to the finite line-width of the laser itself.

We were able to resolve the wavelengths of two laser sources that were about about 6 nm apart from each

other. The next step would be to use the spectrometer to resolve the spectral composition of a incoherent light source, like a calibration lamp. As of now we were unable to resolve the spectral composition of a neon calibration source. The light from the calibration source was filtered using a 50 μm pin-hole or an iris, and the expanding beam was either directly incident on the detector or was passed through a lens or beam expander in attempt to collimate the beam. However, the light incident on the detector seemed to be very weak, since the picture appeared dark and required longer integration times than previously used. When the light source was close to the detector and directly incident on the detector without any spatial filter, the intensity seemed to be sufficient, but no spectrum from the mid-field pattern could be found. This most likely is because a wide range of angles are incident on the detector, so the Talbot effect is blurred out. Therefore, if we are able to increase in the incident power while the beam remains collimated, we may be able to measure the spectral composition of the calibration source.

In theory, there should be no reason why the Talbot spectrometer should be unable to spectrally resolve the signal. One concern is that since the pixel does not simply sample the light-field pattern, but integrates over a region of it, the detector image might be dominated by a DC background if the spectrum contains too many different wavelengths. This should not be a serious limitation because if multiple images corresponding to different laser wavelengths are added together manually, the FFT still reveals all of the wavelength components. However, we should still develop a model to predict how the Talbot effect behaves when the incident light contains a range of wavelengths.

To understand the origin of the measured wavelength offset and the two peaks in our spectrum, we should develop code to predict the detector response at any orientation in the mid-field. At best, this may fully explain the our experimental results. At worst, this can help us understand the tolerance of the spectrometer when the components are misaligned. Other people in the group are working on removing the glass slide and micro-lens array on top of the detector, as they might also contribute to the non-ideal features in the spectra.

Table 5.1 compares our work to the existing miniature spectrometer. Our miniature spectrometer has one of the higher etendues of the spectrometers presented so far, and potentially can have a comparable resolution. It is not the smallest spectrometer presented, but is good enough for our application.

Our experimental work was done with off-the-shelf components. A higher resolution spectrometer can be built according to the design curves. This would help us verify that the design curves are correct, and could potentially be used to measure actual Raman data, if the signal-to-noise ratio and dynamic range of the detector is sufficient.

Table 5.1: Miniature Spectrometers

This table lists recent miniature spectrometers that have appeared in the literature. The estimates of the spectrometer size included the space in between the grating and the detector. Etendue is calculated from $\pi(\mathrm{NA})^2 A_{slit}$.

Author	Spectrometer Type	Resolution	Etendue (mm^2)	Size (mm x mm x mm)
Kung 2001 [38]	Talbot	42 nm	0.003	40+ x 4.9 x 6.5
Xu 2003 [92]	Disordered 3D PhC	2-20 nm estimate	0.024	30+ x 5 x 5
Redding 2013 [67]	Disordered 2D PhC	0.75 nm	1e-7	0.100 x 0.050 on chip
Park 2008 [58]	Fresnel	10-23 nm	8.2e-4	1-7 x 0.750 x 0.750
Momeni 2009 [48]	Waveguide	0.010 nm	1e-7	0.080 x 0.200 on chip
Wang 2014 [87]	Broadband Diffractive Optic	1 nm	0.077	500 x 9 x 9
This work (exp.)	Talbot	4 nm	0.033	5 x 10 x 10
This work (theor.)	Talbot	0.5nm	0.033	3 x 10 x 10

The etendue of this device could be improved if the angle of acceptance is increased. This can potentially be done using computational methods, or maybe by designing a flat lens, as reported by Arbabi et al., [3] to collimate the incoming light. This step would help reduce the size of many spectrometers, since all systems right now require some optics to clean or focus the light onto the spectrometer itself.

5.1.2 Photonic Crystal Barcodes

The barcodes devices fabricated were on the order of 10μm by 10μm, and the narrowest linewidth measured was about 2 nm. Our high-end goal for this application was to design resonators that were as small as possible and exhibited Q's of about 100000. This would enable us to make 10000 barcodes with single resonant peaks within a 100 nm spectral range. However, as shown by our experiments, one resonant cavity can have multiple peaks. Having multiple peaks increases the number of barcode variants that can be made.

The spectral characteristics of the PhC barocdes as they are now are not terrible compared to the existing barcodes technologies. Considering the broadest linewidths, which are about 10 nm, we would have about 10 barcodes within a 100 nm span. Then if we were able to engineer the three resonant frequencies such that the relative position of the three resonant frequencies was altered, we could make another 10 barcodes for each new orientation.

The main concern is the barcode's size. The barcode is already relatively large for a cell, and would have a lower chance of being useful in a cellular environment if the barcode size is increased. Because the in-plane

Table 5.2: Comparison to Existing Biological Barcode Technologies

Barcode Description	Barcode Type	Size	Spectral Line Width	Number of Codes
Microscopic beads encoded with fluorophores beads [5]	Spectroscopic (Visible)	100μm diameter sphere	35 nm to 100 nm (asymmetric) [68]	2^N
Microscopic beads encoded with quantum dots [91]	Spectroscopic (Visible)	10μm diameter sphere	20 nm to 90 nm [7] [68]	m^N [a]
Nanoporous anodic alumina [69]	Spectroscopic (Visible)	2D thin-film	about 5 nm	$< 2^N$
Porous-silicon photonic crystals [11]	Spectroscopic (Vis-NIR)	94 mm x 94 mm x 5 mm	11 nm	2^N
Silicon colloid Microcavities [66]	Spectroscopic (NIR)	4.1 μm diameter sphere	1 nm	$< 2^N$
This work (goal)	Spectroscopic	10 μm x 10 μm x 220 nm	< 0.5 nm	2^N
This work (exp.)	Spectroscopic	9.1 μm x 7.35 μm x 220 nm	2 nm	2^N

Unless otherwise marked, N corresponds to the number of distinct units (e.g. fluorophores) possible.
[a] m = number of intensity levels.

and material absorption loss of these devices limits the maximum Q achievable for each resonant mode, it will be difficult to increase Q by two to three orders of magnitude while maintaining the barcode size, and potentially impossible if we had to reduce the barcode's size as well.

In order to increase the quality factor of the cavity, we first should understand why the resonant frequencies of the cavity change with cavity size, and the origin of the fine structure of the peaks.

The fabricated devices could be carefully characterized to better understand how small changes in the resonant cavity affect the radiative Q of the resonant modes of the cavity, but understanding how the photonic crystal resonant modes behave in a confined slab can lead to insight on how to use these features to our advantage. For example, the fine structure in the peaks could be in-plane or out-of-plane Fabry-Perot resonances that the PhC resonant mode couples particulary strongly to. To determine whether or not the fine-structure peaks are in-plane or out-of-plane, one could tilt the resonant cavities at various ϕs to see if the fine-structure is changes or not. Once this effect is understood, the device can be designed to avoid or utilize these features. If the fine structure is independent of device orientation, it could be used to encode even more

information in the barcode. The PhC barcode would then be similar to the colloidal silicon microcavities [11], but be able to store even more information because it would also have the resonances from the PhC.

Investigating the design of the resonant cavity more thoroughly might also be worthwhile. For example, it may be better to simulate other cavity designs, like a hexapole design as propose by Takagi et al. [77] and Kim et al [37]. Because of symmetry, these Q's for the resonant modes may be more similar, as opposed to the current cavity where the x-polarized modes are extremely low Q while the y-polarized mode is relatively high Q. If we do not limit ourselves to CMOS processing, we could also increase the radiative Q by increasing the thickness of the device.

Relying only on engineering the defect cavity to change the vertical emission and radiative Q of a single mode might not be enough to achieve resonant peaks with line widths of about 0.01 nm. In order to achieve the target Q_{rad} and Q_{loss} for the back-scattering devices, non-traditional PhC designs need to be investigated. For example, we should investigate using interference effects, like Fano interference [27] or cancellation [33] to decrease the linewidth of the resonant peak.

It would also be interesting to investigate how the boundaries of the PhC device can be engineered to reduce in-plane loss of the resonant mode. For example, it may be possible to engineer the PhC so that the edges totally internally reflect the resonant mode, preventing the fields from leaving the device. To do this, one could investigate the transmission and reflection properties of the photonic crystal by finding its isofrequency diagram through simulation.

On the measurement side, the current experimental set-up needs to be improved. For example, by replacing the camera with a large area photodetector and replacing the polarizing beam splitter with two polarizers with a higher rejection ratio, the sensitivity of the measurement will improve. By rebuilding the system so that it is not vertically oriented on a microscope that is sensitive to vibration, the noise in the measurement will be reduced.

5.1.3 Fano Resonance Modulator

To complete our analysis on the Fano modulators, we need to characterize the modulation extinction and efficiency of the modulators on the most recent tape-out. This was not done due to time constraints.

Before we can compare with state-of-the-art silicon photonic modulators, the next step for this project would be to better understand how to reliably engineer Fano resonances with strong asymmetries; the key concept that is still missing is being able to predict the phase between the fundamental and first excited TE modes. This might be as simple as using the propagation constant of each mode to figure out how the

ideal length of the modulator. If there is another chance to put a few Fano devices on a tape-out, it would be worth having Fano modulators of different lengths to check if our predictions are correct. In a previous iteration of devices, a resistor was used to thermally tune the index of the bus waveguide and control the phase between the resonant mode and the propagating mode. However, the previous devices showed high loss, so we did not use include a tuning resistor to minimize losses. Furthermore, if one could accurately predict the phase of the Fano modulator, the modulators would be easier to design and test in the future.

To prove that the photonic crystal modulators can have remarkably low energy costs per bit and better high frequency modulation response due to the small size of the resonant mode, we would need to optimize the doping distributions and the modulator pads. For example, we could optimize the doping distribution around the cavity and reduce the internal capacitance of the contact pads. Alternatively, since more researchers have worked on optimizing the structures of ring resonator modulators, one could attempt to design ring resonators that exhibit a Fano resonance to improve their modulation extinction and efficiency.

5.2 Conclusion

Though each application (the spectrometer, optical barcode, and electro-optic modulator) already has relatively well-defined solutions, the presented ideas can expand the limits of each technology. Specifically, by utilizing interference effects, such as the interference between the $m = -1, 0, +1$ diffraction orders for the Talbot spectrometer, or the interference between two resonant modes for the PhC barcodes, or the interference between one resonant mode and one continuous mode for the Fano modulators, the limits of existing technologies can be pushed further. We were able to create functional, first-iteration devices that all used periodic, subwavelength dielectric structures, though more work needs to be done to optimize the devices to prove their benefits over the current state-of-the-art technologies.

Of these three technologies, the theory explaining the spectrometer was the most complete, since the Talbot effect is relatively easy to understand. The theory behind the Fano modulator is also relatively well understood, though we still have not developed a model to estimate the phase between the two modes. For the barcode application, though the back-scattering theory is well understood, developing size-constrained, high quality factor PhCs is an interesting challenge that will require more insight. If successful, the applications might extend beyond what we proposed here.

Bibliography

[1] Y. Akahane, T. Asano, B.S. Song, and S. Noda. High-q photonic nanocavity in a two-dimensional photonic crystal. *Nature*, 425:944–947, October 2003.

[2] Jeffrey N Anker, W Paige Hall, Olga Lyandres, Nilam C Shah, Jing Zhao, and Richard P Van Duyne. Biosensing with plasmonic nanosensors. *Nature materials*, 7(6):442–453, 2008.

[3] Amir Arbabi, Yu Horie, Alexander J Ball, Mahmood Bagheri, and Andrei Faraon. Efficient high na flat micro-lenses realized using high contrast transmitarrays. In *SPIE OPTO*, pages 93720P–93720P. International Society for Optics and Photonics, 2015.

[4] W.L. Barnes and T.W. Ebbesen A. Dereux. Surface plasmon subwavelength optics. *Nature*, 424:824–830, August 2003.

[5] Bronwyn J Battersby, Darryn Bryant, Wim Meutermans, Daniel Matthews, Mark L Smythe, and Matt Trau. Toward larger chemical libraries: encoding with fluorescent colloids in combinatorial chemistry. *Journal of the American Chemical Society*, 122(9):2138–2139, 2000.

[6] H.A. Bethe. Theory of diffraction by small holes. *The Physical Review*, 66(7):163–182, October 1944.

[7] Marcel Bruchez, Mario Moronne, Peter Gin, Shimon Weiss, and A Paul Alivisatos. Semiconductor nanocrystals as fluorescent biological labels. *science*, 281(5385):2013–2016, 1998.

[8] G.H. Chan, J. Zhao, E.M. Hicks, G.C. Schatz, , and R.P. Van Duyne. Plasmonic properties of copper nanoparticles fabricated by nanoshpere lithography. *Nano Letters*, 7(7):1947–1952, May 2007.

[9] B.D. Chithrani, A.A. Ghazani, and W.C.W. Chan. Determining the size and shape dependence of gold nanoparticle uptake into mammalian cells. *ACS Nano Letters*, 6(4):662–668, February 2006.

[10] J. S. Chong. Hybrid laser with cmos photonics. Master's thesis, Department of EECS, Massachusetts Institute of Technology, Cambridge, MA, February 2014.

[11] Frederique Cunin, Thomas A Schmedake, Jamie R Link, Yang Yang Li, Jennifer Koh, Sangeeta N Bhatia, and Michael J Sailor. Biomolecular screening with encoded porous-silicon photonic crystals. *Nature materials*, 1(1):39–41, 2002.

[12] P.B. Deotare, M.W. McCutcheon, Frank I, W, M. Khan, and M. Lončar. High quality factor photonic crystal nanobeam cavities. *Applied Physics Letters*, 94(12):121106, February 2009.

[13] A.M.K. Enejder, T.G. Scecina, J. Oh, M. Hunter, W.-C. Shih, S. Sasic, G.L. Horowitz, and M.S. Feld. Raman spectroscopy for noninvasive glucose measurements. *Journal of Biomedical Optics*, 10(3):031114–0311149, 2005.

[14] D.J. Thomson et al. 50-gb/s silicon optical modulator. *IEEE Photonics Technology Letters*, 24(4):234–236, February 2012.

[15] K. Mehta et al. High-q cmos-integrated photonic crystal microcavity devices. *Nature Science Reports*, 4(4077), February 2014.

[16] M. Georgas et al. A monolithically-integrated optical transmitter and receiver in a zero-change 45nm soi process. *IEEE Journal of Solid State Physics*, 47(7), July 2012.

[17] M.R. Watts et al. Vertical junction silicon microdisk modulators and switches. *Optics Express*, 19(22):21989–22003, October 2011.

[18] P. Dong et al. High-speed and compact silicon modulator based on a racetrack resonator with a 1 v drive voltage. *Optics Express*, 35(19):3246–3248, October 2010.

[19] Q. Xu et al. 12.5 gbit/s carrier-injection-based silicon micro-ring silicon modulators. *Optics Express*, 15(2):430–436, January 2007.

[20] Hicham Fenniri, Lunhan Ding, Alexander E Ribbe, and Yegor Zyrianov. Barcoded resins: A new concept for polymer-supported combinatorial library self-deconvolution. *Journal of the American Chemical Society*, 123(33):8151–8152, 2001.

[21] Hicham Fenniri, Hartmut G Hedderich, Kenneth S Haber, Jihane Achkar, Brian Taylor, and Dor Ben-Amotz. Towards the dred of resin-supported combinatorial libraries: A non-invasive methodology based on bead self-encoding and multispectral imaging. *Angewandte Chemie*, 112(24):4657–4659, 2000.

[22] F.J. Garcia-Vidal, H.J. Lezec, T.W. Ebbesen, and L. Martin-Moreno. Multiple paths to enhance optical transmission through a single subwavelength slit. *Physical Review Letters*, 90(21), May 2003.

[23] A. Gerrits, B. Dykstra, O.J. Kalmykowa, K. Klauke, E. Verovskaya, M.J.C. Broekhuls, G. de Haan, and L. B. Bystrykh. Cellular barcoding tool for clonal analysis in the hematopoietic system. *Blood*, 115(13):2610–2618, April 2010.

[24] A.K. Ghosh, C. Fishman, and T. Feng. Theory of the electrical and photovoltaic properties of polycrystalline silicon. *Journal of Applied Physics*, 51(1):446–454, January 1980.

[25] W.M.J. Green, M.L. Rooks, L. Sekaric, and Y.A. Vlasov. Ultra-compact, low rf power, 10 gb/s silicon mach-zehnder modulator. *Optics Express*, 15(25):17106–17113, December 2007.

[26] N. Guerineau, E. Mambro, and J. Primot. Talbot experiment re-examined: study of the chromatic regime and application to spectrometry. *Optics Express*, 11(24):3310–3319, December 2003.

[27] S. Haddidi, L. Le-Gratiet, I. Sagnes, F. Raineri, A. Bazin, K. Bencheikh, J.A. Levenson, and A.M. Yacomotti. High quality beaming and efficient free-space coupling in l3 photonic crystal active nanocavities. *Optics Express*, 20(17):18876–18886, August 2013.

[28] E. Hecht. *Optics*. Addison Wesley Longman, Inc, third edition, 1998.

[29] J. Hendrickson, R. Soref, J. Sweet, and W. Buchwald. Ultrasensitive silicon photonic-crystal nanobeam electro-optical modulator: Design and simulation. *Optics Express*, 22(3):3271–3283, February 2014.

[30] K. Huang, L. Pu, Y. Shi, P. Han, R. Zhang, and Y.D. Zheng. Photoluminescence oscillations in porous alumina films. *Applied physics letters*, 89(20):201118, 2006.

[31] E. Hutter and J.H. Fendler. Exploitation of localized surface plasmon resonance. *Advanced Materials*, 16(19):1685–1706, October 2004.

[32] Illumina. 2010.

[33] J.D. Joannopolous, S.G. Johnson, J.N. Winn, and R.D. Meade. *Photonic Crystals: Molding the Flow of Light*. Princeton Universty Press, Princteon, NJ, second edition, 2008.

[34] Steven G. Johnson and J. D. Joannopoulos. Block-iterative frequency-domain methods for maxwell's equations in a planewave basis. *Opt. Express*, 8(3):173–190, 2001.

[35] Aristeidis Karalis, Steven G Johnson, and JD Joannopoulos. Discrete-mode cancellation mechanism for high-q integrated optical cavities with small modal volume. *Optics letters*, 29(19):2309–2311, 2004.

[36] Nikolai G Khlebtsov and Lev A Dykman. Optical properties and biomedical applications of plasmonic nanoparticles. *Journal of Quantitative Spectroscopy and Radiative Transfer*, 111(1):1–35, 2010.

[37] Se-Heon Kim, Sun-Kyung Kim, and Yong-Hee Lee. Vertical beaming of wavelength-scale photonic crystal resonators. *Physical Review B*, 73(23):235117, 2006.

[38] Helen L Kung, Aparna Bhatnagar, and David AB Miller. Transform spectrometer based on measuring the periodicity of talbot self-images. *Optics letters*, 26(21):1645–1647, 2001.

[39] Adolf W Lohmann, Hans Knuppertz, and Jürgen Jahns. Fractional montgomery effect: a self-imaging phenomenon. *JOSA A*, 22(8):1500–1508, 2005.

[40] G.R. Lokshin, A.V. Uchenov, M.A. Entin, V.E. Belonuchkin, and N.L. Eskin. On the spectra selectivity of talbot and lau effects. *Optics and Spectroscopy*, 89(2):312–317, January 2000.

[41] F.R.S Lord Rayleigh. On copying diffraction-gratings, and on some phenoena connected therewith. *Phil. Mag. S. 5*, 11(67):196–205, March 1880.

[42] G. Lucovsky, R.F. Schwarz, and R.B. Emmons. Transit time considerations in p-i-n diodes. *Journal of Applied Physics*, 35(622):622–628, March 1964.

[43] V.A. Mandelshtam and H.S. Taylor. Harmonic inversion of time signals. *Journal of Chemical Physics*, 107(17):6756–6769, 1997.

[44] V.A. Mandelshtam and H.S. Taylor. Harmonic inversion of time signals. *Journal of Chemical Physics*, 109(10):4128, 1998.

[45] Enrique AJ Marcatili. Dielectric rectangular waveguide and directional coupler for integrated optics. *Bell System Technical Journal*, 48(7):2071–2102, 1969.

[46] K. Mehta. Resonant photonic crystal photodetectors for the infrared in silicon. Master's thesis, Department of EECS Massachusetts Institute of Technology, Cambridge, MA, September 2012.

[47] K. Mehta, J.S. Orcutt, and R.J. Ram. Fano line shapes in transmission spectra of silicon photonic crystal resonators. *Applied Physics Letters*, 102, February 2013.

[48] Babak Momeni, Ehsan Shah Hosseini, Murtaza Askari, Mohammad Soltani, and Ali Adibi. Integrated photonic crystal spectrometers for sensing applications. *Optics communications*, 282(15):3168–3171, 2009.

[49] Edmund J Moran, Sepehr Sarshar, John F Cargill, Manouchehr M Shahbaz, Anna Lio, Adnan MM Mjalli, and Robert W Armstrong. Radio frequency tag encoded combinatorial library method for the discovery of tripeptide-substituted cinnamic acid inhibitors of the protein tyrosine phosphatase ptp1b. *Journal of the American Chemical Society*, 117(43):10787–10788, 1995.

[50] E. Moreno, F.J. Garcia-Vidal, and L. Martin-Moreno. Enhanced transmission and beaming of light via photonic crystal surface modes. *Physical Review B*, 69(12), March 2004.

[51] Sheila R. Nicewarner-Peña, R. Griffith Freeman, Brian D. Reiss, Lin He, David J. Peña, Ian D. Walton, Remy Cromer, Christine D. Keating, and Michael J. Natan. Submicrometer metallic barcodes. *Science*, 294(5540):137–141, 2001.

[52] KC Nicolaou, Xiao-Yi Xiao, Zahra Parandoosh, Andrew Senyei, and Michael P Nova. Radiofrequency encoded combinatorial chemistry. *Angewandte Chemie International Edition in English*, 34(20):2289–2291, 1995.

[53] J. S. Orcutt. *Monolithic Electronic-Photonic Integration in State-of-the-Art CMOS Processes*. PhD thesis, Department of EECS, Massachusetts Institute of Technology, Cambridge, MA, February 2012.

[54] Ardavan F. Oskooi, Chris Kottke, and Steven G. Johnson. Accurate finite-difference time-domain simulation of anisotropic media by subpixel smoothing. *Optics Letters*, 34:2778–2780, September 2009.

[55] Ardavan F. Oskooi, David Roundy, Mihai Ibanescu, Peter Bermel, J. D. Joannopoulos, and Steven G. Johnson. MEEP: A flexible free-software package for electromagnetic simulations by the FDTD method. *Computer Physics Communications*, 181:687–702, January 2010.

[56] O. Painter, R. K. Lee, A. Scherer, A. Yariv, J.D. O'Brien, P.D. Dapkus, and I. Kim. Two-dimensional photonic band-gap defect mode laser. *Science*, 284(5421):1819–1821, June 1999.

[57] Y. Park and S. Choi. Miniaturization of optical spectroscopes into fresnel microspectrometers. *Journal of Nanophotonics*, 7(1):077599, 2013.

[58] Yeonjoon Park, Laura Koch, Kyo D Song, SangJoon Park, Glen King, and Sang Choi. Miniaturization of a fresnel spectrometer. *Journal of Optics A: Pure and Applied Optics*, 10(9):095301, 2008.

[59] Ibsen Photonics. 2015.

[60] Ibsen Photonics. 2015.

[61] D.J. Pine, D.A. Weitz, J.X. Zhu, and E. Herbolzheimer. Diffusing-wave spectroscopy: dynamic light scattering in the multiple scattering limit. *Journal of Physics France*, 51:2101–2127, September 1990.

[62] C. Pitsillides, E.K. Joe, X. Wei, R.R. Anderson, and C.P. Lin. Selective cell targeting with light-absorbing microparticles and nanoparticles. *Biophysical Journal*, 84(6):4023–4032, June 2003.

[63] C.V. Poulton, X.G. Zeng, J.S. Orcutt, J.M. Shainline, M.T. Wade, and M. Popovic. Linear photonic crystal microcavities in zero-change soi cmos. In *Advanced Photonics 2013*, 2013.

[64] S. Preradovic and N.C. Karmaka. *Multiresonator-Based Chipless RFID: Barcode of the Future*. Springer Science and Business Media, January 2012.

[65] K. Preston, P. Dong, B. Schmidt, and M. Lipson. High-speed all-optical modulation using polycrystalline silicon microring resonators. *Applied Physics Letters*, 92(151104), 2008.

[66] F. Ramiro-Manzano, R. Fenollosa, E. XifrÃ©-PÃ©rez, M. GarÃn, and F. Meseguer. Porous silicon microcavities based photonic barcodes. *Advanced Materials*, 23(27):3022–3025, 2011.

[67] B. Redding, S.F. Liew, R. Sarma, and H. Cao. Compact spectrometer based on a disordered photonic chip. *Nature Photonics*, 7:746–751, September 2013.

[68] Ute Resch-Genger, Markus Grabolle, Sara Cavaliere-Jaricot, Roland Nitschke, and Thomas Nann. Quantum dots versus organic dyes as fluorescent labels. *Nature methods*, 5(9):763–775, 2008.

[69] A. Santos, V.S. Balderrama, M. Alba, P. FormentÃn, J. FerrÃ©-Borrull, J. PallarÃ¨s, and L.F. Marsal. Nanoporous anodic alumina barcodes: Toward smart optical biosensors. *Advanced Materials*, 24(8):1050–1054, 2012.

[70] Takashi Sato. Focus position and depth of two-dimensional patterning by talbot effect lithography. *Microelectronic Engineering*, 123:80–83, 2014.

[71] K. Schepers, E. Swart, J.W.J. van Heijst, C. Gerlach, M. Castrucci, D. Sie, M. Heimerikx, A. Velds, R.M. Kerkhoven, R. Arens, and T.N.M. Schumacher. Dissecting t cell lineage relationships by cellular barcoding. *The Journal of Experimental Medicine*, 205:2309–2318, September 2008.

[72] R. A. Soref and B. R. Bennett. Electrooptical effects in silicon. *IEEE Journal of Quantum Electronics*, 23(1):123–129, January 1987.

[73] Xing Su, Jingwu Zhang, Lei Sun, Tae-Woong Koo, Selena Chan, Narayan Sundararajan, Mineo Yamakawa, and Andrew A Berlin. Composite organic-inorganic nanoparticles (coins) with chemically encoded optical signatures. *Nano letters*, 5(1):49–54, 2005.

[74] Y. Sun and S. Forrest. Enhanced light out-coupling of organic light-emitting devices using embedded low-index grids. *Nature Photonics*, 2:483–487, August 2008.

[75] S. M. Sze. *Physics of Semiconductor Devices.* John Wiley and Sons, Inc, 1969.

[76] S. M. Sze. *Semiconductor Devices: Physics and Technology.* Wiley-India, 2009.

[77] H. Takagi, Y. Ota, N. Kumagai, S. Ishida, S. Iwamoto, and Y. Arakawa. High q h1 photonic crystal nanocavities with efficient vertical emission. *Optics Express*, 20(27), December 2012.

[78] HF Talbot. *Dublin Philos. Mag*, 9(1836):401, 1836.

[79] T. Tanabe, K. Nishiguchi, E. Kuramochi, and M. Notomi. Low power and fast electro-optic silicon modulator with later p-i-n embedded photonic crystal nanocavity. *Optics Express*, 17(25):22505–22513, December 2009.

[80] Erman Timurdogan, Cheryl M Sorace-Agaskar, Jie Sun, Ehsan Shah Hosseini, Aleksandr Biberman, and Michael R Watts. An ultralow power athermal silicon modulator. *Nature communications*, 5, 2014.

[81] N.-V.-Q. Tran, Sylvain Combrie, Pierre Coleman, Alfredo De Rossi, and Ting Mei. Vertical high emission in photonic crystal nanocavities by band-folding design. *Physics Review B*, 82(075120), August 2010.

[82] N.V.Q Tran, S. Combrie, and A. De Rossi. Directive emission from high-q photonic crystal cavities through band folding. *Physical Review B*, 79(4), January 2009.

[83] P.D. Vasko, J. Blackwell, and J.L. Koenig. Infrared and raman spectroscopy of carbohydrates.: Part ii: Normal coordinate analysis of α-d-glucose. *Carbohydrate Research*, 23(3):407–416, 1972.

[84] A. Vena, E. Perret, and S. Tedjini. Chipless rfid tag using hybrid coding technique. *IEEE Transactions on Microwave Theory and Techniques*, 59(12):3356–3364, December 2011.

[85] Jelena Vučković, Marko Lončar, Hideo Mabuchi, and Axel Scherer. Design of photonic crystal microcavities for cavity qed. *Physical Review E*, 65(1):016608, 2001.

[86] Jelena Vuckovic, Marko Loncar, Tomoyuki Yoshie, Axel Scherer, Michael Armen, Jon Williams, and Hideo Mabuchi. High-q optical nanocavities in planar photonic crystals. In *High-Power Lasers and Applications*, pages 190–199. International Society for Optics and Photonics, 2002.

[87] Peng Wang and Rajesh Menon. Computational spectrometer based on a broadband diffractive optic. *Optics express*, 22(12):14575–14587, 2014.

[88] G.R.T. White, G. Gardiner, G. Prabhakar, and A.A. Razak. A comparison of barcoding and rfid technologies in practice. *Journal of Information, Information Technology, and Organizations*, 2:119–132, 2007.

[89] R. Windisch, C. Rooman, S. Meinlschmidt, P. Kiesel, D. Zipperer, G.H. Dohler, B. Dutta, M. Kujik, G. Borghs, and P. Heremans. Impact of texture-enhanced transmission on high-efficiency surface-textured light-emitting diodes. *Applied Physics Letters*, 79(15), October 2001.

[90] Y.R. Wu, A.E. Hollowell, C. Zheng, and L.J. Guo. Angle-insensitive structural colours based on metallic nanocavities and coloured pixels beyond the diffraction limit. *Scientific Reports*, 3, February 2013.

[91] Hongxia Xu, Y Sha Michael, Edith Y Wong, Janet Uphoff, Yanzhang Xu, Joseph A Treadway, Anh Truong, Eamonn O'Brien, Steven Asquith, Michael Stubbins, et al. Multiplexed snp genotyping using the qbead^{TM} system: a quantum dot-encoded microsphere-based assay. *Nucleic Acids Research*, 31(8):e43–e43, 2003.

[92] Z. Xu, Z. Wang, M. E. Sullivan, D. J. Brady, S. H. Foulger, and A. Adibi. Multimodal multiplex spectroscopy using photonic crystals. *Optics Express*, 11(18), September 2003.

[93] Xiang-Wei Zhao, Zhao-Bin Liu, Han Yang, Keiji Nagai, Yu-Hua Zhao, and Zhong-Ze Gu. Uniformly colorized beads for multiplex immunoassay. *Chemistry of materials*, 18(9):2443–2449, 2006.

.1 Electrical Modulation

.1.1 Carrier Depletion Modulation

The first method is the depletion of carriers that were introduced to the resonator structure by material doping. Typically, p-n junctions are used for depletion mode modulation, since much of the resonant mode in the cavity would overlap with the depletion region and see the most change in carrier concentration. In a p-i-n diode, the depletion width approximately remains constant. Because the the carrier concentrations p and n are generally much greater than the doping of the intrinsic (i) region, the i region is usually completely depleted even at zero bias voltage. The width of the depletion region still does change with reverse bias, though the change is usually small compared to the width of the i-region.

Assuming the i-region is completely depleted at zero bias voltage, the total depletion width is

$$W_{dep} = W_i + \sqrt{\frac{2\varepsilon_{Si}}{q}\frac{N_A + N_D}{N_A N_D}(\frac{k_B T}{q}\ln\frac{N_D N_A}{n_i^2} - V_A)} \tag{1}$$

where W_i is the width of the intrinsic region, ε_{Si} is the dielectric constant of silicon, N_A and N_D are the doping concentrations of the p- and n-regions respectively, and V_A is the applied voltage.

The junction in AC can be modeled as a parallel plate capacitor (with a parasitic series resistance). When a higher reverse bias voltage is applied, carriers are removed from the edge of the depletion region and doping impurities are ionized. When the bias voltage is returned to a lower bias voltage, carriers return to the edges to the quasineutral region. Considering only the AC signal, it is as if the edges of the depletion region are the plates of parallel plate capacitor that are being charged and discharged. In the case of the p-i-n junction, the capacitance only decreases slightly with reverse bias voltage because the junction width only slightly increases, and is largely determined by the i-region width. For a junction of area A, the capacitance can be modeled as

$$C = \frac{\varepsilon_{Si} A}{W_{dep}} \approx \frac{\varepsilon_{Si} A}{W_i}. \tag{2}$$

The resistance of the p-i-n junction is largely determined by the resistance of the intrinsic region,

$$R = \frac{W_i}{\sigma A} \tag{3}$$

where $\sigma = q(\mu_p p + \mu_n n)$ is the conductivity and A is the area of the junction [75]. In reverse bias, the conductivity is largely defined by the photo-generated carriers due to the absorption of the light in the

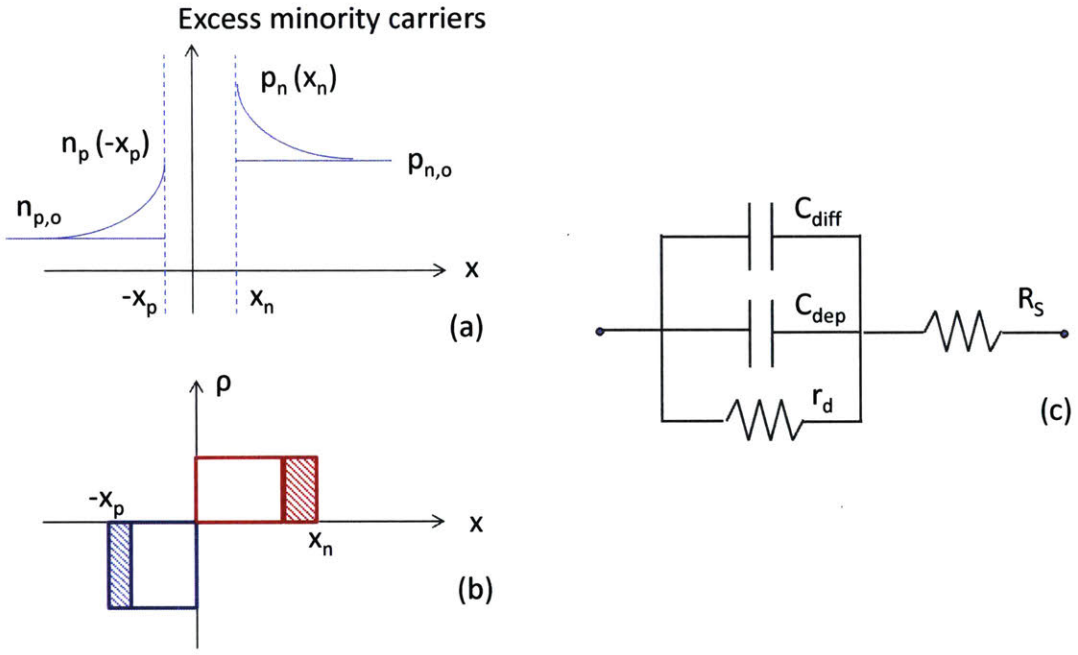

Figure 1: Diode Small-Signal Model
(a) This graph shows the minority carrier density when the device is in forward bias. (b) This graph shows the charge in the depletion region. The shaded regions show the "parallel plates" that are charged and discharged with modulation. (c) This circuit is the model of a diode, where C_{diff} is the diffusion capacitance (dominant in forward bias), C_{dep} is the depletion capacitance (dominant in reverse bias), r_d is the small-signal resistance of the diode, and R_S is the series resistance of the diode (which can be ignored in small-signal analysis). [76]

resonant cavity. An estimate of the maximum switching frequency can be found by modeling the junction as an RC circuit in parallel.

.1.2 Carrier Injection Modulation

The second way to achieve modulation is through the injection of carriers by applying a forward bias. The IV characteristics on p-i-n junctions are similar to p-n junctions, except that the current is a function of the intrinsic region width W_i as opposed to the minority carrier diffusion length. The IV relation can be expressed as [75]

$$I = \frac{AqW_i}{\tau_e}(p_{n,o} + n_{p,o})e^{\frac{qV}{k_B T}}. \tag{4}$$

In this equation we assume the lifetimes of the minority carriers (τ_e) to be the same.

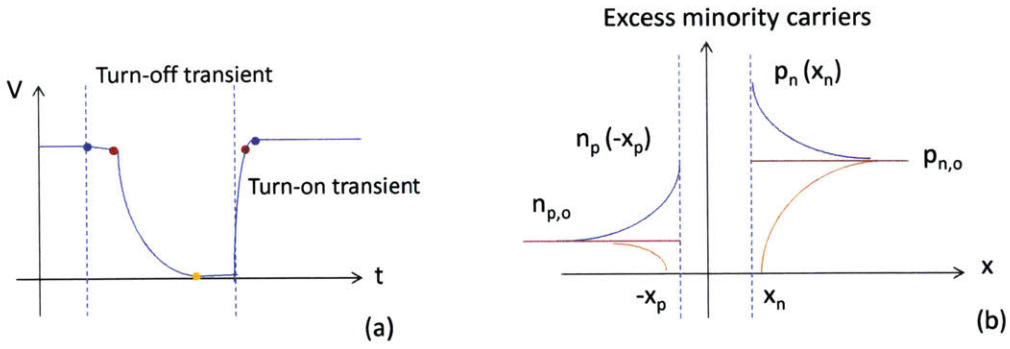

Figure 2: Theory of Turn-on and Turn-off Transients
(a) This figure shows what typical on and off transients look like in a p-n junction. When the diode is turned off, carriers must either recombine or be carried out of the depletion region by the internal electric field. When the diode is turned off, carriers are injected into the depletion from the quasineutral regions.
(b) This figure shows what the minority carriers look like in the on and off states. [76]

Because of the current going through the diode, the diffusion capacitance dominates. Defined generally as $C = \frac{dQ}{dV}$, where $Q = Q_p + Q_n = \tau_e(I_p + I_n)$, the diffusion capacitance can be expressed as

$$C_{diff} = \frac{Aq^2 W_i}{k_B T}(p_{n,o} + n_{p,o})e^{\frac{qV}{k_B T}}. \tag{5}$$

The resistance is still as previously defined in equation (3). However, the conductivity is largely determined by the injected carriers, and is proportional to the current through p-i-n junction in forward bias. The small signal resistance resistance, $r = \frac{dv}{di}|_{(V,I)}$ is then approximately the inverse of the forward current. Again, to find the maximum switching frequency, the diode can be modeled as a RC circuit with time constant $\tau = RC$.

However, since typically square waves of bits are used to characterize modulators, which have high and low frequency components as opposed to sinusoidal waves of a pure frequency, $\tau = RC$ is not the most accurate estimate of the roll-off frequency. A more useful way of approaching the problem is by looking at the transient behavior, which is determined by a combination of recombination/turn-on and injection/turn-off time constants. When the electrical signal goes from high to low, the optical signal turns off when the carriers in the intrinsic region have been removed. The removal of carriers in the intrinsic region is affected by the carrier drift from the electric field and the recombination of electrons and holes.

The minimum switching time is [75] [42] is about

$$\frac{1}{\tau_{off}} = \frac{1}{\tau_e} + \frac{(\mu_e + \mu_h)(V_{bi} + V_R)}{W_i^2} \leq \frac{1}{\tau_e} + \frac{v_{sat,n} + v_{sat,p}}{W_i} \tag{6}$$

where τ_e is the recombination lifetime, μ_n and μ_p are the mobilities of the electrons and holes respectively, $v_{sat,n}$ and $v_{sat,p}$ are the saturated velocities of the electrons and holes respectively, V_{bi} is the built-in voltage, V_R is the applied reverse bias voltage, and W_i is the width of the intrinsic region. The physical intuition behind this switching frequency is simply that there are two parallel mechanisms of carrier removal: recombination (characterized by the recombination lifetime), and electrical removal (characterized by the time it takes for the minority carriers to cross the intrinsic region width). Notice that the larger the intrinsic region width, the longer the turn-off time constant is.

When the electrical signal goes from low to high, the optical signal turns on once the carrier density in the intrinsic region reaches N_{ON}. The turn-on time constant can be approximated as [76]

$$\tau_{on} = \tau_e \ln(\frac{J_{inj}}{J_{inj} - J_{on}}) \tag{7}$$

where τ_e is the carrier lifetime, J_{inj} is the injected current density, and J_{on} is the current density that corresponds to the on-state carrier density. In single-crystalline silicon, the carrier lifetime is around 1 to 5 ns, it becomes difficult to obtain picosecond switching required for Gbit/s communication without large driving currents. Therefore, depletion modulators tend to be more energy efficient at rates faster than 1 Gbps.

However, in polysilicon, the carrier lifetime is significantly reduced. According to Ghosh et al, the effective lifetime of polysilicon can be expressed as [24]

$$\tau_{eff} = \frac{d}{6\sigma v N_{ss}} \tag{8}$$

where d is the dimension of the grain (which was modeled as cube), σ is the measured capture cross section for surface states, v is the thermal velocity of the carriers, and N_{ss} is the concentration of recombination centers per unit area at the grain boundaries. If we assume $\sigma = 2 \times 10^{-16}\text{cm}^2$, $v = 10^7$ cm/sec, and $N_{ss} = 1.6 \times 10^{13}\text{cm}^{-2}$, then

$$\tau_{eff} = 5 \times 10^{-6} d. \tag{9}$$

For the all-optical microring modulator devices fabricated by Preston et al, the polysilicon grain size

was anticpated to be approximately 300 nm, which corresponds to an effective lifetime of around 150 ps. Experimentally, they measure an effective lifetime of 135 ± 5 ps [65]. Therefore, reducing the carrier lifetime by about a factor of 3 is very possible, and would allow for modulation up to at least 3 GHz if the injection current was 0.

.2 Talbot Effect Depth of Field

In Lokshin and Guerineau, they claim that the depth of field of the Talbot effect is dependent on the number of lines in the grating [40] and the width of the grating slit [26]. Though neither of these papers showed derivations, it is likely that they superposed spherical waves propagating from the transmission grating.

Consider a 2D system, with an infinitely long transmission grating with infinitely small slits spaced a distance d apart. The slits are infinitely thin, so that transmission from each slit is a spherical wave. The intensity at any x and z, $I(x, z)$, can be expressed as

$$I(x,z) = \left| \sum_{N=-\infty}^{\infty} \frac{exp(-jkr_N)}{sqrt(r_N)} \right| \tag{10}$$

, where r_N is the distance from point (x, z) to the N^{th} slit.

If we look at the intensity as a function of z at $x = 0$, the equation is simplified to

$$I(x,z) = \left| \sum_{N=-\infty}^{\infty} \frac{exp(-jk(\sqrt{(z^2 + (Nd)^2)}))}{\sqrt{z^2 + (Nd)^2}} \right|. \tag{11}$$

Using a Taylor expansion to simplify the square root, we get

$$I(x,z) \approx \left| exp(-jkz) \sum_{N=-\infty}^{\infty} \frac{exp(-jk(N^2d^2/2z)}{z + N^2d^2/2z)} \right|. \tag{12}$$

We notice that only when $k\frac{N^2d^2}{2z} = m\pi$ is the intensity non-zero. Solving for z, we obtain the Talbot distance, as expected. However, this also means for an infinite grating, we obtain delta functions at the Talbot distances. With a grating of a finite size, we'd get a sinc function in z at the Talbot distance. We could also predict that by making the slits wider, the depth of field for the Talbot self-image would also increase.

The above equations are a restatement of Fresnel diffraction for a transmission grating. However, the conclusions we reached do not match the simulation results–this is because of the decreasing intensity of the

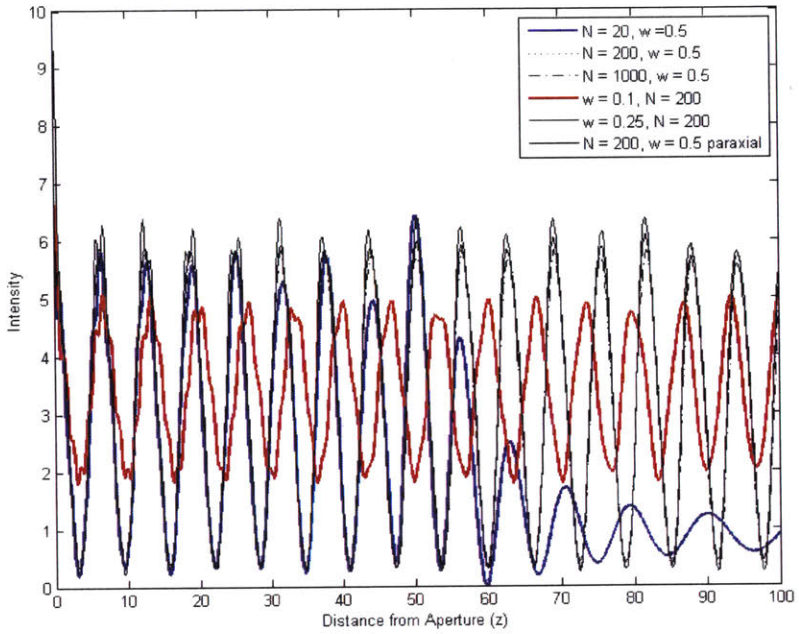

Figure 3: Variation of Talbot Effect Depth of Field
This graph shows simulations of the intensity as a function of z for a variety of grating sizes and slit widths. Here, N is the approximate number of slits an w is the width of the slit relative to the period. The wavelength-to-period ratio (λ/d) is 1.89.

spherical wave as it propagates farther away from the slit. The above conclusion assumes that the waves from all slits are equal, when in reality, the slits that are closest to it dominate the intensity pattern. As a result, the mid-field diffraction pattern looks more like cosines than delta functions.

Most of them closely match, with the exception of the $N = 20$ plot and the $w = 1$ plot. The $N = 20$ plot decays because the z on the graph goes past the region where the Talbot effect exists. The region where the Talbot effect exists is determined by the region where the $m = -1, 0$, and $+1$ diffraction coexist. The $w = 0.1$ plot is different because the smaller slit size transmits waves that are more spherical/non-paraxial.

.2.1 Farfield Radiation Pattern Calculation

The surface electric (J_s) and magnetic (M_s) currents are calculated using

$$\mathbf{J}_s = \hat{n} \times \mathbf{H} = -\hat{x}H_y + \hat{y}H_x \tag{13}$$

$$\mathbf{M}_s = -\hat{n} \times \mathbf{E} = \hat{x}E_y - \hat{y}E_x \tag{14}$$

The vector potentials for each are

$$\mathbf{A} = \mu_0 \int_s \frac{\mathbf{J}_s e^{-jkr}}{4\pi r} dS \tag{15}$$

$$\mathbf{F} = \varepsilon_0 \int_s \frac{\mathbf{M}_s e^{-jkr}}{4\pi r} dS \tag{16}$$

In the far-field, $r \approx R - \rho \cos \Psi$, where $\rho = \sqrt{x^2 + y^2}$. Note that $k\rho \cos \Psi = kx \sin\theta \cos\phi + ky \sin\theta \sin\phi = k_x x + k_y y$.

Under this approximation, we have

$$\mathbf{A} = \mu_0 \frac{e^{-jkr}}{4\pi r} \mathbf{N} \tag{17}$$

$$\mathbf{F} = \varepsilon_0 \frac{e^{-jkr}}{4\pi r} \mathbf{L} \tag{18}$$

, where

$$N_x(k_x, k_y) = -FT\{H_y(x,y)\} \tag{19}$$

$$N_y(k_x, k_y) = +FT\{H_x(x,y)\} \tag{20}$$

$$L_x(k_x, k_y) = +FT\{E_y(x,y)\} \tag{21}$$

$$L_y(k_x, k_y) = -FT\{E_x(x,y)\} \tag{22}$$

$$\tag{23}$$

The numerical aperture in this coordinate system is simply $k_x^2 + k_y^2 = k^2 \sin^2\theta$, where θ is the angle of acceptance of the objective.

Alternative explanation: Because typically a single polarization of the electric field is dominant, the

far-field radiation pattern can be determined by propagating the near-field pattern using spherical waves. Because we are interested in the far-field, the Fraunhofer approximation can be used. This also tells us that the far-field radiation pattern is the 2D Fourier transform of the near-field pattern.

.2.2 Barcode Device CNSE Chip Layout

Barcode devices on the CNSE chip are explained in the figures.

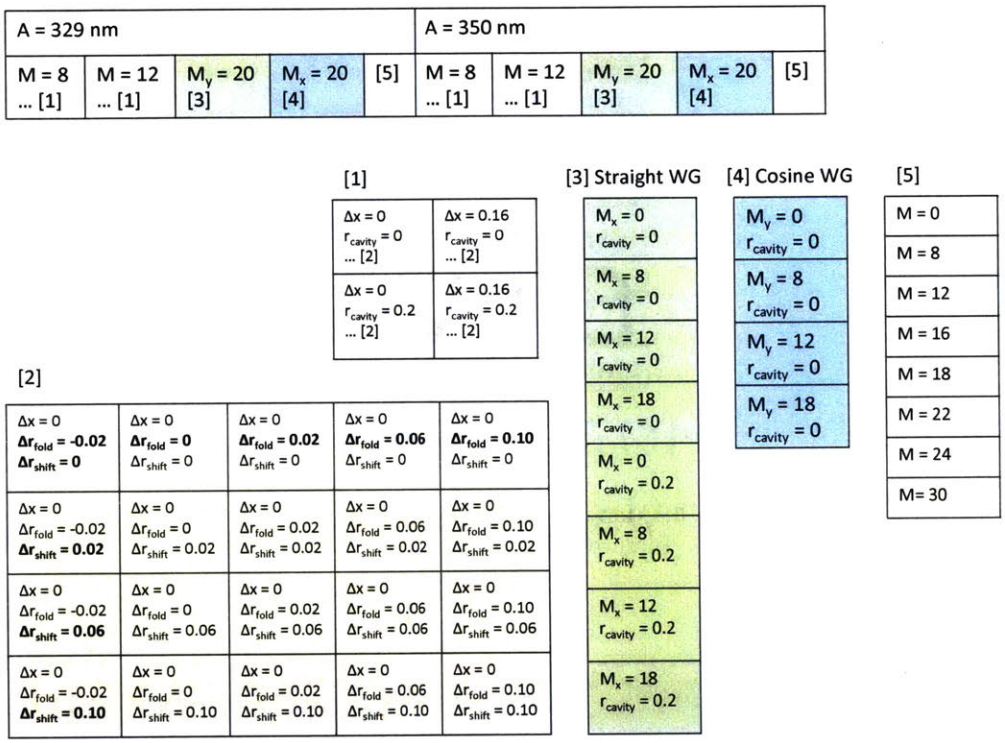

Figure 4: Map of Barcode Devices on Chip
Key explaining devices.

.2.3 Modulator Device CNSE Chip Layout

Active and passive devices contain the same modulator architectures–the basic Lorenztian modulator, four types of tapered Fano modulators, and two types of TE/TM grating coupler modulators. Each cavity has variants with at least 0, 8, and 12 mirror holes. The active devices have different p-i-n structures (small 'i', large 'i') around the cavity so that hopefully a few devices will work well. The pads are designed for a 100

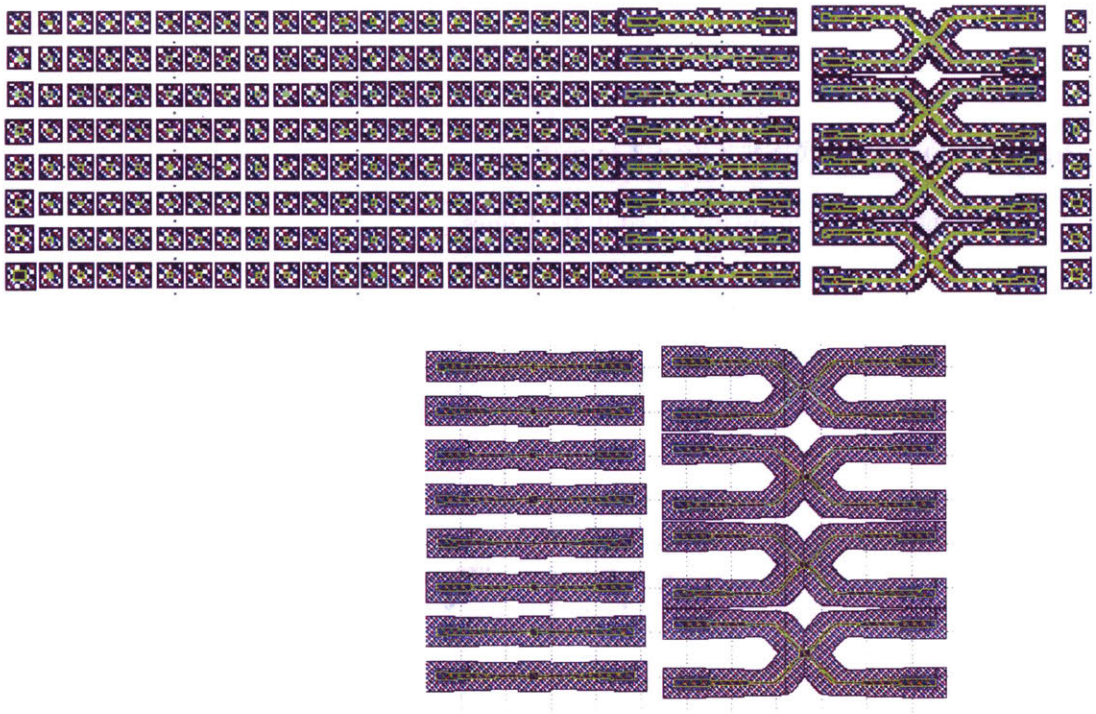

Figure 5: Map of Barcode Devices on Chip
Picture of device layout.

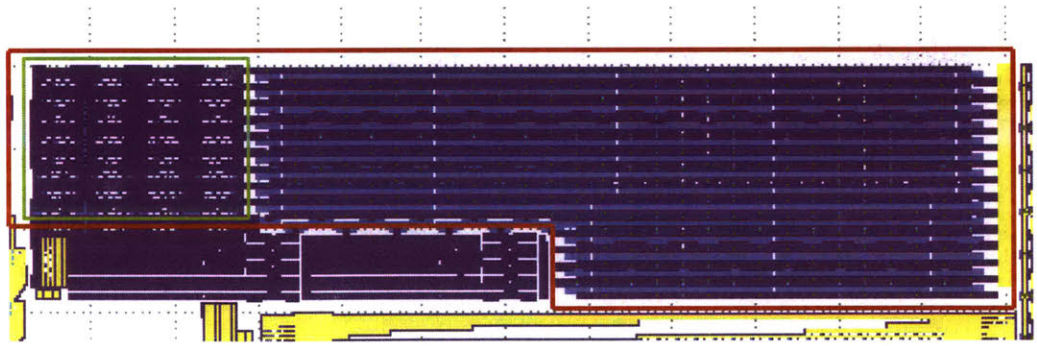

Figure 6: Map of Modulator Devices on Chip
Picture of all the devices. Region enclosed by red box are the waveguide designs. Region enclosed by green box are passive devices.

micron pitch and are 60 μm squares.